First-principles investigation of $BiFeO_3$ and related multiferroic materials

Thesis submitted in fulfillment of the requirements
for the degree of Doctor of Philosophy in Physics
Universitat Autonoma de Barcelona, 2012

Author: Otto E. González Vázquez
Supervisor: Dr. Jorge Iniguez
Tutor: Javier Rodríguez Viejo

Institut de Ciencia de Materials de Barcelona (ICMAB-CSIC)

Universitat Autonoma de Barcelona

A mis padres

Jorge Íñiguez González, Científico Titular del Consejo Superior de Investigaciones Cientificas (CSIC) en el Instituto de Ciencia de Materiales de Barcelona (ICMAB).

CERTIFICA:

Que el trabajo presentado en esta memoria, titulado **First-principles investigation of $BiFeO_3$ and related multiferroic materials** ha sido realizado bajo su dirección por **D. Otto Emiliano González Vázquez** en el Departamento de Teoría y simulación de Materiales del Instituto de Ciencia de Materiales de Barcelona y **EMITE su conformidad** para que dicha memoria sea presentada y tenga lugar, posteriormente, su correspondiente defensa para optar por el título de **Doctor** por la **Universidad Autónoma de Barcelona**. Para que así conste firma la presente:

Dr. Jorge Íniguez González
Director

De la misma manera, **Javier Rodríguez Viejo**, profesor titular de la **Universidad Autónoma de Barcelona**, como tutor de la presente tesis, firma el presente certificado:

Prof. Javier Rodríguez Viejo
Tutor

El interesado,

Barcelona, 16 de Mayo del 2012.

Abstract

This work is about magnetoeltric multiferroics, a relatively new class of materials discovered by the mid of the past century, which involve simultaneously ferroelectricity and magnetism. Perovskite oxide BiFeO3 (BFO) is one of the few multiferroic materials at room temperature. However, as its ferroelectric and anti-ferromagnetic transition temperatures are relatively high (about 1100 K and 640 K, respectively), BFO s electromechanical and magnetoelectric responses are small at ambient conditions.

In this thesis we used ab-initio methods, based on density functional theory, to study the basic properties of BFO and proposed possible strategies for enhancing its response. We used first-principles methods to perform a systematic search for potentially stable phases of BFO. We considered the distortions that are most common among perovskite oxides and found a large number of local minima of the energy. We discussed the variety of low-symmetry structures discovered, as well as the implications of these findings as regards current experimental work on this compound.

We also carried out a study of the $Bi_{1-x}La_xFeO_3$ (BLFO) solid solution formed by multiferroic BFO and the paraelectric antiferromagnet $LaFeO_3$ (LFO). We discussed the structural transformations that BLFO undergoes as a function of La content and the connection of our results with the existing crystallographic studies. We found that, in a wide range of intermediate compositions, BLFO presents competitive phases that are essentially degenerate in energy. Further, our results suggested that, within this unusual morphotropic region, an electric field might be used to induce various types of paraelectric-to-ferroelectric transitions in the compound. We also discussed BLFO s response properties and showed that they can be significantly enhanced by partial substitution of Bi/La atoms in the pure BFO and LFO materials. We analyzed the atomistic mechanisms responsible for such improved properties and showed that the effects can be captured by simple phenomenological models that treat explicitly the composition x in a Landau-like potential.

Furthermore, we performed a first-principles study of BFO at high pressures. Our work revealed the main structural change in Bi s coordination and suppression of the ferroelectric distortion, electronic spin crossover and metallization, and magnetic loss of order effects favored by compression and how they are connected. Our results are consistent with and explain the striking manifold transitions observed experimentally

We conclude our thesis presenting the preliminary results of an ongoing project in which we are modeling the energetics of the oxygen octahedra rotations in perovskite oxides. The model is fitted to the first-principles results and a careful check of its validity is carried out.

Resumen

Esta tesis trata sobre los magnetoeléctricos multiferroicos, una clase relativamente nueva de materiales descubiertos a mediados del siglo pasado, que presentan simultaneamente ferroelectricidad y magnetismo. El $BiFeO_3$ (BFO) es un óxido con estructura perovskita, el cual es uno de los pocos materiales multiferroicos a temperatura ambiente. Sin embargo, como sus temperaturas de ordenamiento ferroeléctrico y anti-ferromagnético son relativamente altas (alrededor de 1100 K y 640 K, respectivamente), las respuestas electromecánica y magnetoeléctrica del BFO son relativamente pequenas en condiciones ambientales.

En esta tesis se utilizamos métodos ab-initio, basados en la teoría del funcional de la densidad (DFT), para estudiar las propiedades del BFO, y proponemos una posible estrategia para la mejora de su respuesta. Hemos utilizado métodos de primeros principios para llevar a cabo una búsqueda sistemática de las fases potencialmente estables de este compuesto. En la que consideramos las distorsiones más comunes entre los óxidos de tipo perovskita y encontrando un gran número de mínimos locales de la energía. En este trabajo se discute la gran variedad de estructuras de baja simetría descubiertas, así como las implicaciones de estos hallazgos en cuanto a los trabajos experimentales mas recientes sobre este compuesto.

También se llevó acabo un estudio de la solución sólida $Bi_{1-x}La_x$ FeO_3 (BLFO) formada por la BFO y la $LaFeO_3$ (LFO)antiferromagnetica paraeléctrica. Se discuten las transformaciones estructurales que sufre BLFO en función del contenido de La, y la conexión de nuestros resultados con los estudios cristalográficos existentes. Hemos encontrado que, en una amplia gama de composiciones intermedias, la BLFO presenta fases que son esencialmente degeneradas en energía. Además, los resultados sugieren que para este compuesto, dentro de esta región morfotrópica inusual, se puede utilizar un campo eléctrico para inducir transiciones paraeléctrico a ferroeléctrico. También se discuten las propiedades de respuesta de la BLFO y se demuestra que se pueden mejorar significativamente en los materiales puros BFO y LFO, mediante la sustitución parcial de los átomos Bi y La . Se analizaron los mecanismos atómicos responsables de esta mejora en las propiedades y se muestra que los efectos pueden ser capturados por modelos fenomenológicos sencillos, que incluyen de manera explícita la composición x en un potencial de Landau.

Por otra parte, se presenta también un estudio de primeros principios de la BFO a altas presiones. En el cual explicamos la naturaleza de las transiciones de fase del BFO, que simultáneamente involucran un colapso del volumen, un cambio en el estado de spin de High spin a Low spin y una metalización producto del desorden magnético en la nueva fase. Nuestros resultados son consistentes con la transición múltiple observada experimentalmente.

Por último presentamos los resultados preliminares de un proyecto en marcha, en el cual estamos modelando la energética de las rotaciones de los octaedros de oxigeno en los óxidos de estructura perovskita. Para ello se ha expandido la energía en función de los parámetros de orden que caracterizan dichas rotaciones hasta cuarto orden. Hemos fiteado el modelo a los resultados de nuestros cálculos de primeros principios y realizado una comprobación cuidadosa de su valides, determinando que es necesario recurrir a ordenes mas altos en nuestra teoría.

Contents

List of Figures

List of Tables

Introduction

Nowadays we are surrounded by a variety of electronic devices that are integrated into our daily lives. Behind the functioning of these are phenomena such as ferroelectricity, the giant magnetoresistance and others. A new class of materials is currently under intense investigation, these materials called multiferroics can simultaneously exhibit electric and magnetic orders. Such coexistence of both orders and the possible occurrence of a coupling between them (i.e., in the case when magnetoelectric effect is present) opens new possibilities for technological applications.

Since its discovery at the mid of the past century, the phenomenon of multiferroicity has attracted great attention from the scientific community. However, due to the scarcity of such materials and the difficulties in their experimental growth led to a decrease in the activity around these compounds. It was not until the beginning of this century when the field has been refuel by the combination of some factors; the appearance of a seminal paper by Spaldin et al. in which they have discussed a hypothesis for the scarcity of magnetic ferroelectrics, the state of the art experimental technology for the synthesis and characterization of such materials was already mature, and the interest in novel materials with potential technological applications (target technologies range from transducers and magnetic field sensors, to the information storage industry).

Among the multiferroic materials, perovskite oxide bismuth ferrite ($BiFeO_3$ or BFO) is the best studied compound of this family. Despite its simple structure, it is one of the few simple crystals that presents magnetoelectric coupling and multiferroic order at room temperature. BFO was first studied by Smolensky s group in 1959, but their samples were too conductive to be of use. The interest in this compound was dramatically increased after the paper by Wang et al. [88] in which they have reported a unexpectedly large remnant polarization $\mathbf{P}$, fifteen times larger than the one previously observed in single crystals, together with very large ferromagnetism of 1.0 Bohr magneton per unit cell. While some of these results were later proved to be either wrong or misleading, nonetheless the paper has stimulated and inspired a great number of experimental and theoretical works on this compound.

Despite being one of the most studied multiferroics, BFO continues to appear as one of the most fascinating materials of the day. An example of this, is that BFO s phase diagram remains unresolved, with newly reported phases as function of temperature T and/or pressure p [38, 60]. Furthermore, recently it has been shown that it displays a variety of novel fundamental effects, like an increase in conductivity at specifics domain walls [81] or new structural phases in thin films with potentially useful response properties. [94]

Our work is framed in the theoretical and computational study of the properties of BFO and related materials. The objective of the present thesis was the study of the properties of $BiFeO_3$ and to explore possible ways to enhance its functional responses.

The present thesis is organized as follows. The first two chapters are devoted to introduce the theoretical background as well as the state of the art of theoretical works in the subjet covered by this thesis. In chapter 1 we will describe the basics theoretical details of the first-principles methods used in our calculations, along with the general methodology followed in our DFT simulations. Chapter 2 introduces the physical properties and phenomena of interest to our study, like ferroelectricity and magnetism in perovskite oxides, as well as the formalism to treat the magnetoelectric effect in such systems. We also comment on the state of the art for theoretical works in the field, and our contributions to it. The following chapters from 3 to 6 are devoted to the discussion of our results. We present the results of our first principles search for potentially stable phases of the multiferroic $BiFeO_3$ in chapter 3, where we obtained plenty of distinct low-energy phases of the compound and discussed the implications of our findings. In chapter 4 we used first-principles methods to study the $Bi_{1-x}La_xFeO_3$ (BLFO) solid solution formed by the multiferroic $BiFeO_3$ (BFO) and the paraelectric antiferromagnet $LaFeO_3$ (LFO). We discuss BLFO s phase transitions as a function of the La content x, and show that the chemical substitution of Bi/La atoms in the pure compounds leads to significantly improved response properties, which we were able to model with a simple Landau like potential. In chapter 5 we deal with the main electronic, and magnetic effects that occur in $BiFeO_3$ under compression and elucidate how they are connected. Our last results are discussed in chapter 6, where we show the first step in constructing a general theory to capture the energetics of the most common distortions present in perovskites. Finally the results of this work are summarized in the conclusions.

Chapter 1

Density Functional Theory and Methods

1.1 Density Functional Theory

Introduction

Accurate description of chemical and physical properties of materials requires the quantum mechanical treatment of the many-particle system of electrons and nuclei. Properties such as bulk modulus, conductivity or material s response to an applied field can be understood in terms of their microscopic origins. This usually would require solving the Schrodinger Eq. (1.1) for a wavefunction of $3 \times (Number\,of\,particles)$ spatial variables $\{\mathbf{R}, \mathbf{r}\}$,

$$H(\{\mathbf{R}\},\{\mathbf{r}\}) \mid \Psi(\{\mathbf{R}\},\{\mathbf{r}\})\rangle = E \mid \Psi(\{\mathbf{R}\},\{\mathbf{r}\})\rangle \tag{1.1}$$

where:

$$\begin{aligned} H(\{\mathbf{R}\},\{\mathbf{r}\}) = &-\sum_{I=1} \frac{\hbar^2}{2M_I}\nabla^2_{\mathbf{R_I}} - \sum_{i=1}\frac{\hbar^2}{2m}\nabla^2_{\mathbf{r_i}} \\ &+ \frac{1}{2}\sum_{I\neq J}\frac{Z_I Z_J e^2}{|\mathbf{R}_I - \mathbf{R}_J|} + \frac{1}{2}\sum_{i\neq j}\frac{e^2}{|\mathbf{r}_i - \mathbf{r}_j|} - \sum_{Ij}\frac{Z_I e^2}{|\mathbf{R}_I - \mathbf{r}_j|} \end{aligned} \tag{1.2}$$

is the hamiltonian of the many particle problem, M_I is the mass of the nucleus I at the position defined by vector $\mathbf{R}_I$, and m is the mass of the electron at the position $\mathbf{r}_i$. In Eq. (1.2) the first two terms are the kinetic energies of the nuclei and the electrons, respectively, and the remaining terms are the nuclei-nuclei, electron-electron and nuclei-electron Coulomb interactions (with Z_I the atomic number of the nucleus I). Solving these equations is a very complex problem, and some approximations are needed in order to simplify it.

A useful approximation in this context is the Born-Oppenheimer approximation [12]. Within this approximation the nuclei movement and the electronic problem can be treated independently of each other, which can be done as a consequence of the large mass difference between the nuclei and the electrons. The electrons move in a solid much faster than the nuclei, thus the electronic configuration can be considered as completely relaxed in its ground state at each position the ions assume during their motion. Retaining only the kinetic energy term

concerning the electrons we make use of the atomic positions just as parameters rather than variables in the Hamiltonian (1.4).

$$H(\{\mathbf{R}\},\{\mathbf{r}\}) = H_I(\{\mathbf{R}\}) + H_{el}(\{\mathbf{r}\},\{\mathbf{R}\}) \tag{1.3}$$

with:

$$H_{el}(\{\mathbf{r}\};\{\mathbf{R}\}) = -\sum_{i=1}\frac{\hbar^2}{2m_i}\nabla^2_{\mathbf{r_i}} + \frac{1}{2}\sum_{I\neq J}\frac{Z_I Z_J e^2}{|\mathbf{R}_I-\mathbf{R}_J|} + \frac{1}{2}\sum_{i\neq j}\frac{e^2}{|\mathbf{r}_i-\mathbf{r}_j|} - \sum_{Ij}\frac{Z_I e^2}{|\mathbf{R}_I-\mathbf{r}_j|} \tag{1.4}$$

Usually the number N of electrons involved in a condensed matter system is very large, solving the many-electron problem and finding their wave function is an impractical task.

In the last decades density functional theory (DFT) has emerged as a powerful alternative to solving N-body time independent Schrodinger equation. DFT formally reduces the problem of finding the multi-electron wave function to that of finding the electron density distribution $n(\mathbf{r})$ as the elementary quantity. This idea goes back to Thomas and Fermi, who already in 1927, shortly after the milestone publications of Schrodinger and Heisenberg, obtained a heuristic description of the many-electron system completely in terms of the electronic density. [27, 83] For this reason the Thomas-Fermi method is considered by many the conceptual root of the density-functional theory.

1.1.1 The Hohenberg-Kohn theorems

Almost 40 years after the works by Thomas and Fermi, density functional theory was born when Hohenberg and Kohn (HK) presented their famous theorem, [44] which states that the ground state properties of the many-particle system are uniquely determined by the ground state particle density $n(\mathbf{r})$.

Hohenberg and Khon formulated an exact theory to describe the many body problem with the density as the fundamental variable. Their theory contains two theorems on which density functional theory is based. This theory it is applicable to any system of interacting particles in presence of an external potential $V_{ext}(\mathbf{r})$.

The first theorem of the HK theory states:

- **Theorem I:** For any system of interacting particles in an external potential $V_{ext}(\mathbf{r})$, the potential $V_{ext}(\mathbf{r})$ is determined uniquely, except for a constant, by the ground state particle density $n_0(\mathbf{r})$.

The first theorem has a direct corollary: *Since the Hamiltonian is fully determined by the ground state density (except for a constant shift in the energy), all properties of the system are completely determined once we know the ground state density* $n_0(r)$.

Table 1.1: Scheme of the HK theorem, compared to the usual relation of the quantities in quantum mechanics (QM), where the external potential $V_{ext}(\mathbf{r})$ is used to determine the ground state of the system $\Psi_0(\mathbf{r})$ that is used to construct the electronic density $n_0(\mathbf{r})$. In the HK theorem there is a direct relation between the potential and the density

usual QM relation between quantities				
$V_{ext}(\mathbf{r})$	$\rightarrow$	$\Psi_0(\mathbf{r})$	$\rightarrow$	$n_0(\mathbf{r})$
		HK theorem		
$V_{ext}(\mathbf{r})$		$\longleftrightarrow$		$n_0(\mathbf{r})$

A simple proof of the HK first theorem for non-degenerate ground states proceeds by *reductio ad absurdum*. It is shown that a contradiction arises if one assumes that different ground states $\Psi_0 \neq \Psi_0{}'$ (resulting from two different external potentials $V \neq V' + const$) lead to the same ground state density $n_0(\mathbf{r})$.

The prof is based on the Rayleigh-Ritz principle [2] for the ground state energy, which is given by $E_0 = \langle \Psi_0 \mid H_V \mid \Psi_0 \rangle$ with H_V the Hamiltonian associated to the potential V, assuming normalized wave functions as everywhere in this chapter.

$$E_0 < \langle \Psi_0' \mid H_V \mid \Psi_0' \rangle = \langle \Psi_0{}' \mid H_{V'} + V - V' \mid \Psi_0' \rangle = E_0' + \int n_0(\mathbf{r})[V(\mathbf{r}) - V'(\mathbf{r})]dr \qquad (1.5)$$

where the strict inequality is a consequence of the restriction to non-degenerate ground state. Analogously one obtains

$$E_0' < E_0 + \int n_0(\mathbf{r})[V'(\mathbf{r}) - V(\mathbf{r})]d\mathbf{r} \qquad (1.6)$$

Summing the two inequalities leads to the cancellation of the integrals, which contain the same density $n_0(\mathbf{r})$, resulting in the contradiction $E_0{}' + E_0 < E_0 + E_0{}'$. In this way we see clearly that two different external potentials can not lead to the same ground state density, and thus the ground state density uniquely determines the external potential.

The second of the Hohenberg-Kohn theorems, which is the minimum principle for the ground state energy E_0, is of particular importance. In this theorem the ground state energy is defined as a functional of the ground state density $n(\mathbf{r})$.

The second of the HK theorems states:

- **Theorem II:** An universal functional for the energy $F[n(\mathbf{r})]$ in terms of the density $n(\mathbf{r})$ can be defined, valid for any external potential $V_{ext}(\mathbf{r})$. For any particular $V_{ext}(\mathbf{r})$, the

exact ground state energy of the system is the global minimum of the functional (1.7), and the density $n(\mathbf{r})$ that minimizes the functional is the ground state density $n_0(\mathbf{r})$.

$$E[n(\mathbf{r})] = min_{\Psi\to n}(\langle\Psi \mid T+U \mid \Psi\rangle + \langle\Psi \mid V_{ext} \mid \Psi\rangle) = F[n(\mathbf{r})] + \int n(\mathbf{r})V_{ext}(\mathbf{r})d\mathbf{r} \quad (1.7)$$

Where T stands for the kinetic energy operator, and U for the internal potential. Here $F[n(\mathbf{r})]$ is a universal functional of the charge density $n(\mathbf{r})$ and not of $V_{ext}(\mathbf{r})$. For the functional $E[n(\mathbf{r})]$ a variational principle holds: *the ground state energy is minimized by the ground state charge density*. In this way, DFT exactly reduces the problem of finding the N particle wavefunction to that of finding a 3 dimensional function $n(\mathbf{r})$ which minimizes the functional $E[n(\mathbf{r})]$. But in practice the problem remains unsolved, all our ignorance and difficulties to solve the many body Schrodinger Eq. (1.1) are now hidden in the unknown form of the universal functional $F[n(\mathbf{r})]$.

1.1.2 Kohn and Sham equations

The Hohenberg-Kohn theorems have transformed the many body problem of finding the N particle wavefunction to that of finding the 3 dimensional electronic density that minimizes $E[n(\mathbf{r})]$, but unfortunately we do not know the exact form of the functional $F[n(\mathbf{r})]$. This was overcome by Kohn and Sham (KS) one year later [55] when they proposed a way of solving this problem, using an auxiliary system of non interacting electrons with the same charge density $n(\mathbf{r})$ of the real problem. This system would be under the action of an effective potential V_{eff} that is constructed in such a way that the corresponding charge density equals the one of the system of the interacting electrons under study.

The scheme proposed by them has the form:

$$E[n(\mathbf{r})] = T'[n(\mathbf{r})] + \int n(\mathbf{r})V_{eff}(\mathbf{r})d\mathbf{r}. \quad (1.8)$$

where the $T'[n(\mathbf{r})]$ is the kinetic energy functional of the non-interacting electron. For a system of non-interacting electrons the charge density can be expressed as the sum over the occupied electron orbitals $\psi(\mathbf{r})$ which will be called from now on the KS orbitals:

$$n(\mathbf{r}) = \sum_i f_i \mid \psi_i(\mathbf{r}) \mid^2, \quad (1.9)$$

here ω_i is the occupation of the orbital i, for semiconductors and insulators it only can take values 1 or 0 (occupied or unoccupied), while for metals may take values between 0 and 1 (partial occupation). The KS orbitals are related to the V_{eff} as they are the solutions of the Schrodinger like equation (KS equation):

$$H_{KS}\psi_i(\mathbf{r}) = \varepsilon_i\psi_i(\mathbf{r}) \quad (1.10)$$

with the KS Hamiltonian,

$$\left(-\frac{\hbar^2}{2m}\nabla^2 + V_{\mathit{eff}}(\mathbf{r})\right)\psi_i(\mathbf{r}) = \varepsilon_i\psi_i(\mathbf{r}) \quad (1.11)$$

where the KS orbitals obey the orthonormality conditions

$$\int \psi_i^*(\mathbf{r})\psi_j(\mathbf{r})d\mathbf{r} = \delta_{ij}. \tag{1.12}$$

Now, if we know the form of the potential V_{eff}, the problem of finding the density is equivalent to solving the Eq. (1.11), and with this obtain the complete description of the system. But unfortunately it is not so easy, we don t know the actual form of the V_{eff}. Let s examine the variational property seen in the Hohenberg-Kohn theorem (1.7), and try to extract some information about the form of the V_{eff}. We can recast (1.7) as

$$\begin{aligned} E[n(\mathbf{r})] &= F[n(\mathbf{r})] + \int n(\mathbf{r})V_{ext}(\mathbf{r})d\mathbf{r} \\ &= T'[n(\mathbf{r})] + \frac{1}{4\pi\epsilon_0}\frac{e^2}{2}\int\int \frac{n(\mathbf{r})n(\mathbf{r}')}{\mid \mathbf{r}-\mathbf{r}' \mid}d\mathbf{r}d\mathbf{r}' + \int n(\mathbf{r})V_{ext}(\mathbf{r})d\mathbf{r} + E_{xc}[n(\mathbf{r})] \end{aligned}$$

Here the second term is the Hartree term and the last term is the so called *exchange and correlation energy functional*, all our *"ignorance"* is hidden here in this term. It is defined as the difference between the exact energy functional (1.7) and the single electron kinetic energy and the Hartree term proposed by Kohn and Sham,

$$\begin{aligned} E_{xc}[n(\mathbf{r})] &= F[n(\mathbf{r})] - (T'[n(\mathbf{r})] + \frac{1}{4\pi\epsilon_0}\frac{e^2}{2}\int\int \frac{n(\mathbf{r})n(\mathbf{r}')}{\mid \mathbf{r}-\mathbf{r}' \mid}d\mathbf{r}d\mathbf{r}') \\ &= T[n(\mathbf{r})] - T'[n(\mathbf{r})] + U[n(\mathbf{r})] - \frac{1}{4\pi\epsilon_0}\frac{e^2}{2}\int\int \frac{n(\mathbf{r})n(\mathbf{r}')}{\mid \mathbf{r}-\mathbf{r}' \mid}d\mathbf{r}d\mathbf{r}'. \end{aligned} \tag{1.13}$$

Now, to go ahead we just need the exact form for $E_{xc}[n(\mathbf{r})]$, where we collect the electron-electron interaction missed by the Hartree term and the difference between the kinetic energy terms. Since the ground state density $n_0(\mathbf{r})$ minimize the functional $E[n(\mathbf{r})]$, variying Eq. (1.13) in terms of the density we get,

$$\frac{\delta E[n(\mathbf{r})]}{\delta n_0(\mathbf{r})} = \frac{\delta T'[n(\mathbf{r})]}{\delta n_0(\mathbf{r})} + \frac{1}{4\pi\epsilon_0}\frac{e^2}{2}\int \frac{n(\mathbf{r}')}{\mid \mathbf{r}-\mathbf{r}' \mid}d\mathbf{r}' + V_{ext}(\mathbf{r}) + \frac{\delta E_{xc}[n(\mathbf{r})]}{\delta n_0(\mathbf{r})} = 0 \tag{1.14}$$

where we define the exchange-correlation potential as,

$$v_{xc}[n(\mathbf{r})] = \frac{\delta E_{xc}[n(\mathbf{r})]}{\delta n_0(\mathbf{r})} \tag{1.15}$$

We are ready to construct the KS potential V_{eff} as

$$V_{\mathit{eff}}(\mathbf{r}) = V_{ext}(\mathbf{r}) + \frac{1}{4\pi\epsilon_0}\frac{e^2}{2}\int \frac{n(\mathbf{r}')}{\mid \mathbf{r}-\mathbf{r}' \mid}d\mathbf{r}' + v_{xc}[n(\mathbf{r})] \tag{1.16}$$

Formally the KS equations look similar to the self-consistent Hartree-Fock equations, the only difference being the inclusion of the *exchange and correlation potential*. Neither the ψ_i and the ε_i have any physical meaning, except that the ψ_i yield the true ground state density and the energy of the highest occupied KS orbital for finite systems, which is minus the ionization energy [59].

This formalism is in principle exact, but so far we do not know how the exchange-correlation term depends on the density $n(\mathbf{r})$. This is will be covered by the next section.

1.1.3 Approximations to the Exchange Correlation potential, LDA and GGA

In order to solve the KS equations we need to know the form of the exchange-correlation potential.Then we will be able to construct the KS effective potential and solve self-consistently the system of equations. In the same work where they proposed their scheme, Khon and Sham already proposed a form for this functional, *the local density approximation* (LDA). They pointed out that many solids can be considered close to the limit of the homogeneous electron gas (this is for instance the case of metals), and they proposed to treat the exchange-correlation term in this limit (i.e. the effects of the exchange and correlations are local). The form they proposed for the exchange-correlation term was the integral over all the space of the exchange-correlation energy density assumed to be the same as in the homogeneous electron gas with the local charge density $n(\mathbf{r})$.

$$E_{xc}^{LDA}[n(\mathbf{r})] = \int n(\mathbf{r})\xi(n(\mathbf{r}))d\mathbf{r} \tag{1.17}$$

where $\xi(n(\mathbf{r}))$ is the exchange correlation energy density of the uniform electron gas with density $n(\mathbf{r})$, parametrized by quantum Monte Carlo calculations. Several parameterizations are available differing mainly in the treatment of the correlation part, with the Perdew and Zunger being one of the most widely used [66].

The LDA has turned out to be a better approximation than was expected, describing with enough accuracy a large number of systems (mostly solids). It provides atomic positions, lattice constant, and phonon frequencies within an small percent of error. [50]

Despite the success of the LDA, its deficiencies are also known, like the characteristic underestimation of lattice constant ($\sim 2\%$) and consequently the volume ($\sim 5\%$) underestimation. The more the system behave close to the homogeneous gas the better the description obtained within the LDA, but when dealing with molecules or systems that are highly inhomogeneous the results start getting coarse. It is known that the LDA badly overestimates ($\sim 20\%$ and more) cohesive energies and bond strengths in molecules. For such systems a correction to the LDA was also proposed in the original work by Khon-Sham, which includes the density gradient in the expression for the exchange correlation potential,

$$E_{xc}^{GGA}[n(\mathbf{r})] = \int n(\mathbf{r})\xi(n(\mathbf{r}), \mid \nabla n(\mathbf{r}) \mid, ...)d\mathbf{r}. \tag{1.18}$$

This correction provides a better description of the system as it takes into account not only the values of the density in a region of the space, but also the gradients of this density. The generalized gradient correction (GGA) can be seen as the simplest and natural enhancement of LDA to describe inhomogeneous systems. Within this level of approximation, better results are obtained for binding energies and bond lengths of molecules. Several flavors (PW91, PBE, and others) [68,70] of the gradient correction exist nowadays, each of them devised to describe accurately a desired property. A recent revised version of GGA was introduced for solids, the PBEsol parametrization which improves the description of equilibrium properties of densely packed solids [69].

With these results we already have the ingredients to solve the KS system of equations. Many systems can be described by the approximations mentioned above. However, some interesting cases are beyond their scope (for instance strongly correlated systems). How to extend the theories just mentioned to treat these cases, it is covered by the next section.

1.1.4 Treating strongly correlated electrons within DFT

The approximations discussed so far often fail in describing systems with the presence of strongly correlated electrons. In such systems, like for instance materials with transition metal atoms or rare earths, the electrons of the d and f orbitals have an strongly localized behavior deviating from the homogeneous electron gas model. These localized electrons feel a stronger Coulomb interaction that is not covered by the local density approximation LDA neither by the gradient correction GGA. In order to include this strong Coulomb interaction of the localized electrons a modification in the functional is necessary. A Hubbard-like term including effective on-site interactions was introduced and developed by Anisimov and coworkers to correct for the effect of strong correlations [1].

The local functional corrected to treat strongly correlated electrons is named LDA+U (or GGA+U in the case of the gradient corrected). The basic idea behind LDA+U is to include in the functional a term that account for the strong electron-electron interaction in the localized orbitals. The theory can be illustrated briefly by the formula:

$$E^{LDA+U}[n(\mathbf{r})] = E^{LDA}[n(\mathbf{r})] + E^{Hub}[n^{I\sigma}_{mm'}] - E^{dc}[n^{I\sigma}] \tag{1.19}$$

in this equation (1.19), $n^{I\sigma}_{mm'}$ is the atomic orbital occupation matrix for the Hubbard atoms (atoms with strong correlated electrons) at the site I with the spin σ,

$$n^{I\sigma}_{mm'} = \sum_{\mathbf{k},n} f_{\mathbf{k},n} \langle \psi^{\sigma}_{\mathbf{k},n} \mid \phi^{I}_{m} \rangle \langle \phi^{I}_{m'} \mid \psi^{\sigma}_{\mathbf{k},n} \rangle \tag{1.20}$$

here $f_{\mathbf{k},n}$ is the occupation of the electronic state with wave vector $\mathbf{k}$ and band index n. The ϕ^{I}_{m} is the m-th atomic orbital of the atom sitting at site I and the $\psi^{\sigma}_{\mathbf{k},n}$ is the electronic wavefunction corresponding to the state $(\mathbf{k}, n)$ with spin σ.

The first term in Eq. (1.19) is the LDA functional for the energy. The second, $E^{Hub}[n^{I\sigma}_{mm'}]$ is the Hubbard term that quantifies the correlation of the states populating the localized

orbitals. The third term $E^{dc}[n^{I\sigma}]$ is the correlation energy of these states as obtained from the Hubbard term treated at a mean-field level, which has to be subtracted from the total energy to avoid double counting. And the $n^{I\sigma} = \sum_m n^{I\sigma}_{mm}$ is the trace of the atomic orbital occupations matrix for the Hubbard atoms. We can rewrite Eq. (1.19) as,

$$E^{LDA+U}[n(\mathbf{r})] = E^{LDA}[n(\mathbf{r})] + \sum_I \left[\frac{U}{2} \sum_{m,\sigma \neq m',\sigma'} n^{I\sigma}_m n^{I\sigma'}_{m'} - \frac{U}{2} n^I (n^I - 1) \right] \tag{1.21}$$

with $n^{I\sigma}_m = n^{I\sigma}_{mm}$, and $n^I = \sum_{m,\sigma} n^{I\sigma}_m$. The U is the parameter (Hubbard U) that will account for the onsite correlations. It can be seen that if we take the derivative of this Eq. (1.21) with respect to the orbital occupancy, the respective orbital energy is obtained:

$$\epsilon^{I\sigma}_m = \frac{\partial E}{\partial n^{I\sigma}_m} = \epsilon^{I\sigma 0}_m + U(\frac{1}{2} - n^{I\sigma}_m) \tag{1.22}$$

where $\epsilon^{I\sigma 0}_m$ is the corresponding LDA orbital energy. If we compare the occupied ($n^{I\sigma}_m \sim 1$) and unoccupied ($n^{I\sigma}_m \sim 0$) cases, a gap of the order of U opens between these states.

Another way of handling these correlations is the hybrid functional approach. Within this approach the exchange-correlation is expressed as a parametrized combination of the Hartree-Fock exchange and the exchange-correlation dependence of the LDA/GGA approximations. There exist several flavors of hybrids functionals, differing in the parameterization employed.These functionals are the most accurate available so far to treat the insulating magnetic materials of interest in this work. However, calculations based on them are still very expensive from the computational point of view. [19]

1.2 Other Technicalities

1.2.1 Basis set, PAW, and Brillouin Zone sampling

Basis set

Density functional theory is a very powerful and general technique, which can be employed to study a wide variety of systems like: isolated molecules, surfaces, and extended systems such as crystals. For the purpose of this thesis we will be concerned with the last class of systems (*crystals*). A crystal can be described by the repetition of an elementary unit cell defined by the lattice vectors ($\mathbf{a}_1, \mathbf{a}_2, \mathbf{a}_3$) along the Bravais lattice ($\mathbf{R} = n_1\mathbf{a}_1 + n_2\mathbf{a}_2 + n_3\mathbf{a}_3$ where n_1, n_2, and n_3 are integers). This crystal periodicity is reflected in the translational symmetry of the one electron Hamiltonian of the system (e.g the KS Hamiltonian H_{KS}):

$$H_{KS}(\mathbf{r}) = T' + V_{eff}(\mathbf{r}) = T' + V_{eff}(\mathbf{r} + \mathbf{R}) = H_{KS}(\mathbf{r} + \mathbf{R}) \tag{1.23}$$

with T' the kinetic energy of the electron and $V_{eff}(\mathbf{r})$ the periodic effective potential of the crystal.

The eigenstates of such Hamiltonian must satisfy the periodic conditions, and, thus according to Bloch s theorem can be expressed as:

$$\psi_{n\mathbf{k}}(\mathbf{r}+\mathbf{R}) = e^{\imath\mathbf{k}\mathbf{R}} u_{n\mathbf{k}}(\mathbf{r}) \tag{1.24}$$

where $\psi_{n\mathbf{k}}(\mathbf{r})$ are the KS orbitals and $u_{n\mathbf{k}}(\mathbf{r})$ is a lattice periodic function. Therefore each wave function will have associated a wave-vector $\mathbf{k}$, and a band index n that runs over occupied and unoccupied states. Theses wave-vectors $\mathbf{k}$ are points in the reciprocal space defined within the first Brillouin zone (BZ, which is the set of points closer to the origin in reciprocal space than any other reciprocal lattice point),

$$\mathbf{k} = k_1\mathbf{G}_1 + k_2\mathbf{G}_2 + k_3\mathbf{G}_3$$

here k_i are integers and the $\mathbf{G}_i$ are,

$$\mathbf{G}_1 = 2\pi\frac{\mathbf{a}_2\times\mathbf{a}_3}{\mathbf{a}_1\cdot(\mathbf{a}_2\times\mathbf{a}_3)}, \quad \mathbf{G}_2 = 2\pi\frac{\mathbf{a}_3\times\mathbf{a}_1}{\mathbf{a}_1\cdot(\mathbf{a}_2\times\mathbf{a}_3)}, \quad \mathbf{G}_3 = 2\pi\frac{\mathbf{a}_1\times\mathbf{a}_2}{\mathbf{a}_1\cdot(\mathbf{a}_2\times\mathbf{a}_3)}$$

the reciprocal lattice vectors.

The KS orbitals used to compute the charge density in section 1.1.2 can be expanded in terms of a basis set. While the choice of the basis to expand the KS orbitals is in principle arbitrary, some bases are particularly convenient. The two most widely used bases are atomic like orbitals and plane waves ; each of them have certain advantages. In our study we will employ a code that is based on a plane wave basis set, which offers a number of benefits. They appear as the natural choice for extended systems like the case of crystals, taking advantage of the periodicity of the lattice.

Following from the Eq. (1.24) the function $u_{n\mathbf{k}}(\mathbf{r})$ can be expanded in a infinite set of plane waves with wave-vectors $\{\mathbf{G}\}$:

$$u_{n\mathbf{k}}(\mathbf{r}) = \sum_{\mathbf{G}} c_{n\mathbf{k}}(\mathbf{G}) e^{\imath\mathbf{G}\cdot\mathbf{r}} \tag{1.25}$$

The $c_{n\mathbf{k}}(\mathbf{G})$ are obtained from the Fourier transformation given by:

$$c_{n\mathbf{k}}(\mathbf{G}) = \frac{1}{\Omega}\int_{\Omega} u_{n\mathbf{k}}(\mathbf{r}) e^{\imath\mathbf{G}\cdot\mathbf{r}} d\mathbf{r} \tag{1.26}$$

where the integral is done over Ω (the primitive unit cell volume). We may see that the electronic wave functions can be expressed as the sum of plane waves:

$$\psi_{n\mathbf{k}}(\mathbf{r}) = \sum_{\mathbf{G}} c_{n\mathbf{k}}(\mathbf{G}) e^{\imath(\mathbf{k}+\mathbf{G})\cdot\mathbf{r}} \tag{1.27}$$

However, for practical reasons it is not possible to expand the wave functions in an infinite basis of plane waves. Fortunately, if a sufficiently high number of plane waves is considered,

the error from truncating the expansion can be as small as desired. The number of plane waves included in the expansion can be controlled by a parameter, the cutoff for their kinetic energy,

$$\frac{\hbar^2}{2m} \mid \mathbf{k} + \mathbf{G} \mid^2 \leq E_{cut} \tag{1.28}$$

with large enough E_{cut} the basis set is sufficiently complete to describe accurately the system.

Summarizing, the use of plane waves as basis set results in the following advantages:

- Due to Bloch s theorem, plane-waves are the natural choice for the representation of electron bands in a periodic system.
- The kinetic energy operator is diagonal in a plane wave representation. Similarly the potential operator is diagonal in real space. The use of fast Fourier transforms in changing between these representations provides a large saving in computational effort.
- The quality of the basis is easily set by adjusting a single parameter until the desired accuracy is reached.

The disadvantage of using plane-waves as basis set is the number of functions required to describe the rapid oscillations of the electronic wave function close to the nucleus, like in the case of the core electrons. There are several approaches to overcome this difficulty; one of them is the introduction of the Projector Augmented Waves (PAW), which is the one will be used in our calculations.

Projector Augmented Waves (PAW)

Core states are difficult to expand in PWs due to the high number of waves needed to describe their rapidly oscillating wave functions. However, they do not contribute in a significant manner to chemical bonding and solid-state properties. Only outer (valence) electrons do, while core electrons can be considered frozen in their atomic state. This suggests that one can safely ignore changes in core states (frozen core approximation) while solving explicitly for the valence electrons.

The idea of replacing the full atom with a much simpler pseudoatom (by means of a pseudopotential) with valence electrons only, was suggested for the first time in a 1934 paper by Fermi. Pseudopotentials (PPs) have been widely used in solid state physics starting from the 1960s. In earlier approaches PPs were designed to reproduce some known experimental solid-state or atomic properties such as energy gaps or ionization potentials. Other types of PPs were obtained from band structure calculations with the OPW (orthogonalized PW) basis set, by separating the smooth (PW) part from the strongly oscillating part in the wave functions. Nowadays, modern PPs are constructed to mimic the scattering properties of the true atom.

An alternative approach to PP s is the one introduced by Blochl in 1994 known as Projector Augmented Waves (PAW), which is in a sense more general. [11] The idea behind the PAW

method is to map the all-electron wave functions (ψ) into a set of auxiliary pseudo-wave functions (ψ) that are smoother (ψ can be easily expandable in PWs).[1] Such mapping between the complete wave function and the pseudo-wave functions is carried out by means of a linear operator $\mathcal{T}$. This transformation provides a simple and consistent way to reconstruct all-electron wave functions from the pseudo-wave functions that are used in the calculations. In the case of a single atom in the system the mapping is defined as:

$$\mid \psi\rangle = \mathcal{T} \mid \psi\rangle = (1 + T_R) \mid \psi\rangle \tag{1.29}$$

where the functions ψ are solutions of the all-electron atomic KS equation; the functions ψ are the corresponding pseudo-wave functions, which are much smoother in the region of the core electrons, and join smoothly to ψ at the border of R. Outside R, the pseudo-wave functions and the all-electron wave functions must coincide (i.e., $T_R = 0$ outside R).

If we know the transformation $\mathcal{T}$ from the pseudo wave functions to the all-electrons wave functions, we can obtain the physical quantities as the expectation value $\langle A\rangle$ of any operator A from the pseudo-wave functions ψ. This can be done either directly as $\langle\psi \mid A \mid \psi\rangle$ after transformation $\mid \psi\rangle = \mathcal{T} \mid \psi\rangle$ or as the expectation value $\langle\psi \mid A \mid \psi\rangle = \langle\psi \mid A \mid \psi\rangle$ of a pseudo operator $A = \mathcal{T}^\dagger A \mathcal{T}$. Similarly, we can evaluate the total energy directly as a functional of the pseudo-wave functions, with the ground state pseudo-wave function obtained from

$$\frac{\delta E[\mathcal{T} \mid \psi\rangle]}{\delta\langle\psi \mid} = \epsilon \mathcal{T}^\dagger \mathcal{T} \mid \psi\rangle \tag{1.30}$$

It is important to mention that usually, while the valence electrons are considered explicitly on the calculation, the core states are imported from an isolated atom configuration (frozen core approximation).

Brillouin zone Sampling

In order to compute the electronic density in a periodic system one has to integrate over the Brillouin Zone (BZ):

$$n(r) = \frac{\Omega}{(2\pi)^3} \sum_n \int f_{\mathbf{k}n} \mid \psi_{\mathbf{k},n}(r) \mid^2 d\mathbf{k} \tag{1.31}$$

where the index n runs over the bands. This integral can be approximated as a sum over $\mathbf{k}$, and we need to select a finite number of k-points to evaluate the wave functions and extract the electronic structure in the most accurate way possible.

$$n(r) = \frac{\Omega}{(2\pi)^3} \sum_n \int f_{\mathbf{k}n} \mid \psi_{\mathbf{k},n}(r) \mid^2 d\mathbf{k} \;\simeq\; \frac{\Omega}{(2\pi)^3} \sum_n \sum_{\mathbf{k}} f_{\mathbf{k}n} \mid \psi_{\mathbf{k},n}(r) \mid^2 \tag{1.32}$$

[1] Note that the definition all-electron, here and in the following, refers to a KS calculation that includes core electrons, not to a many-electron wave function.

Fortunately, the values of the electronic wavefunctions at k-points that are very close to each other it is almost the same. This property allows for a reduction of the k-points to be sampled, and if we take into account the symmetry of the BZ the number of k-points needed is even lower [5, 16, 61].

For the purpose of this thesis we used the Monkhorst-Pack method to sample the Brillouin zone. This method consist of generating a uniform set of points defined by,

$$\mathbf{k}_{n_1,n_2,n_3} \equiv \sum_{i}^{3} \frac{2n_i - 1}{2N_i}\mathbf{G}_i \tag{1.33}$$

here N_i the number of division along the lattice vector $\mathbf{G}_i$, whith n_i run over all the values $n_i = 0, 1, 2, ..., N_i - 1$. The quality of this sampling can be determined by a convergence tests. For insulators and semiconductors the number of k-points to be accounted in the calculations is lower than for the case of metals. In the case of metals it is important to sample carefully the regions where the band cross the Fermi level as in this regions the bands are partially occupied and the changes in the electronic structures are more drastic than in the case of filled bands.

1.2.2 Convergence tests and Example calculations for $BiFeO_3$

In order to set the calculations conditions we have performed a convergence study. As explained before, the parameters energy cutoff and density of the k-point grid determine the quality of the calculations. In order to describe appropriately the system we need to adjust this two parameters to obtain an adequate description at a lower computational cost. For materials where strong correlations play a fundamental role, the value of the Hubbard U entering the LDA+U/GGA+U also need to be set. We want to illustrate how these calculation conditions were determined for the case of $BiFeO_3$ (BFO), a material that is relevant for the purpose of our work.

$BiFeO_3$ is a ferroelectric material, with a G-anitferromagnetic order (G-AFM, an antiferromagnetic coupling between all first nearest neighboring magnetic ions) in its ground state (see Fig. 1.1). It has a rhombohedral symmetry with $R3c$ space group and a polarization along the [111] direction, expressed in the Cartesian setting defined in Fig. 1.1. We want to have a proper description of the system; thus, to ensure we have reached the desired accuracy, we checked how well described were: the equilibrium structure, the phonon spectra, and energy difference between the most relevant magnetic orders [G-AFM and the ferromagnetic (FM) orders] with respect to the parameters mentioned before.

For the convergence study we performed a relaxation of the structure starting from the atomic positions reported by the previous work [63]. For these calculations the structure was spanned to a pseudo-cubic 40 atom cell that will be the cell used in our calculations (see Fig. 1.1). This cell is obtained by doubling the 5-atom cell of the ideal perovskite structure along the three cartesian directions. As we are interested in the study of possible phase transitions in BFO, the use of this 40 atom cell allows more degrees of freedom in the atomic relaxations

and the possibility to explore more symmetries that are compatible with it.

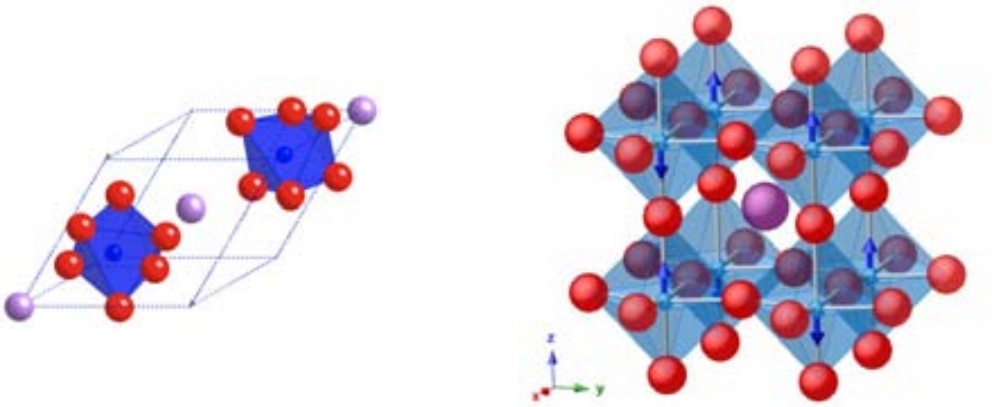

Figure 1.1: The rhombohedral 10 atom unit cell of $BiFeO_3$; G type Antiferromagnetism in a 40 atom pseudo-cubic unit cell

The correct description of the magnetic order is crucial in order to attain the correct ground-state of the system. As explained before, the electrons responsible for the magnetic properties are the strongly localized $3d$ electrons from the Fe atoms. In order to have an adequate description of these electrons, a correct value for the parameter U has to be chosen. For that purpose we computed the energy differences between the ferromagnetic and the antiferromagnetic orders for different values of U. These calculations were done at constant cell and atomic positions (taken from a previous relaxation of the reported structure in [63]).We compare our results with those obtained from calculations with B1-WC hybrid functional, (see Fig. 1.2) which will be our reference for accuracy with respect to the relative stability of the magnetic phases. [19] We obtained that U =4 eV reproduce accurately the results from hybrid calculations and thus is the one chosen by us to describe the d electrons interaction in Fe.

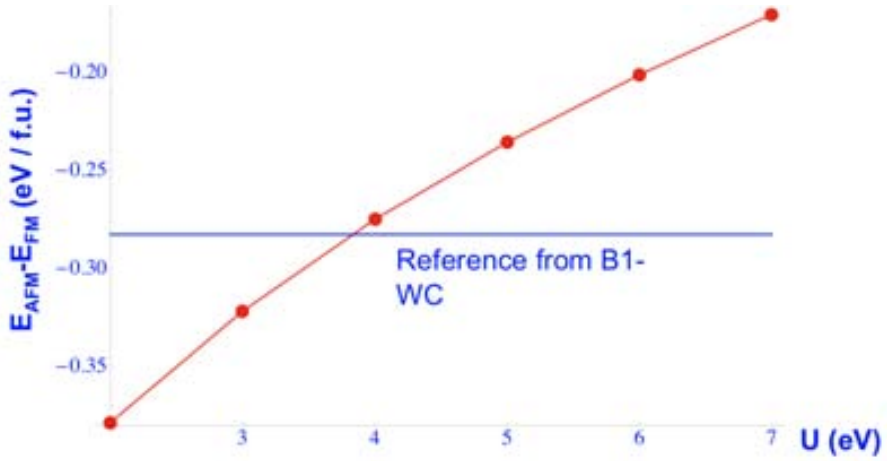

Figure 1.2: The value of the U that best fit the hybrid (B1-WC) results is the $U = 4$ eV, the same conclusion was obtained for both GGA+U (shown here), and LDA+U

When dealing with ferroelectric materials it is crucial to have an accurate description of the structure. Ferroelectricity is strongly related to the structural distortions, specially those breaking the inversion symmetry. For this purpose we did full relaxations (unit cell and atomic positions) with several values for the energy cutoff and different grids of k-points (Gamma-centered), and compared the results. The relaxations were carried employing the quasi-Newton algorithm to relax the ions into their ground state.

E_{cut}[eV]	300	400	**500**	600
a [Å]	5.668	5.688	**5.696**	5.704
$\alpha[^o]$	59.30	59.20	**59.17**	59.10
V_{rh}[Å^3]	126.76	127.74	**128.21**	128.45
Bi_x	0.000	0.000	**0.000**	0.000
Fe_x	0.277	0.278	**0.279**	0.279
O_x	0.561	0.562	**0.563**	0.563
O_y	0.961	0.962	**0.964**	0.964
O_z	0.109	0.110	**0.111**	0.111

$k-point$	$3\times3\times3$	$4\times4\times4$	$5\times5\times5$
a [Å]	**5.696**	5.696	5.696
$\alpha[^o]$	**59.17**	59.17	59.17
V_{rh}[Å^3]	**128.21**	128.21	128.21
Bi_x	**0.000**	0.000	0.000
Fe_x	**0.279**	0.279	0.279
O_x	**0.563**	0.563	0.563
O_y	**0.964**	0.964	0.964
O_z	**0.111**	0.111	0.111

Table 1.2: Calculated lattice constant a, rhombohedral angle α, volume V_{rh} of the rhombohedral cell, and Wyckoff positions ($2a(x,x,x)$ for the cations and $6b(x,y,z)$ for the anions) of $BiFeO_3$. Left: for different Energy cutoffs and $3\times3\times3$ grid of k-points. Right: for different grid of k-points and Energy cutoff $E_{cut} = 500$ eV.

The stopping criteria for the relaxations was to achieve residual forces and stresses below 0.01 eV/Å and 1 kB, respectively. Relaxations were re-run until obtaining the relaxation within one step to ensure that big changes in volume will not introduce error due to changes in the number of plane waves included in the calculations. The structural details obtained for the different settings can be compared in table (1.2), where we can appreciate that the result obtained for $E_{cut} = 500$ eV and a $k-point$ grid of $3\times3\times3$ are sufficiently converged. The results for the equilibrium volume are shown graphically in Fig. (1.3).

Lattice dynamical properties are of special importance when describing the ferroelectric and response properties of BFO. We also have computed the phonon frequencies for different settings and compared our results to determine which calculation conditions are sufficiently converged with this respect. It can be see from table 1.4 that the 500 eV energy cutoff and the grid $3\times3\times3$ are already well converged with respect to the phonon frequencies calculations.

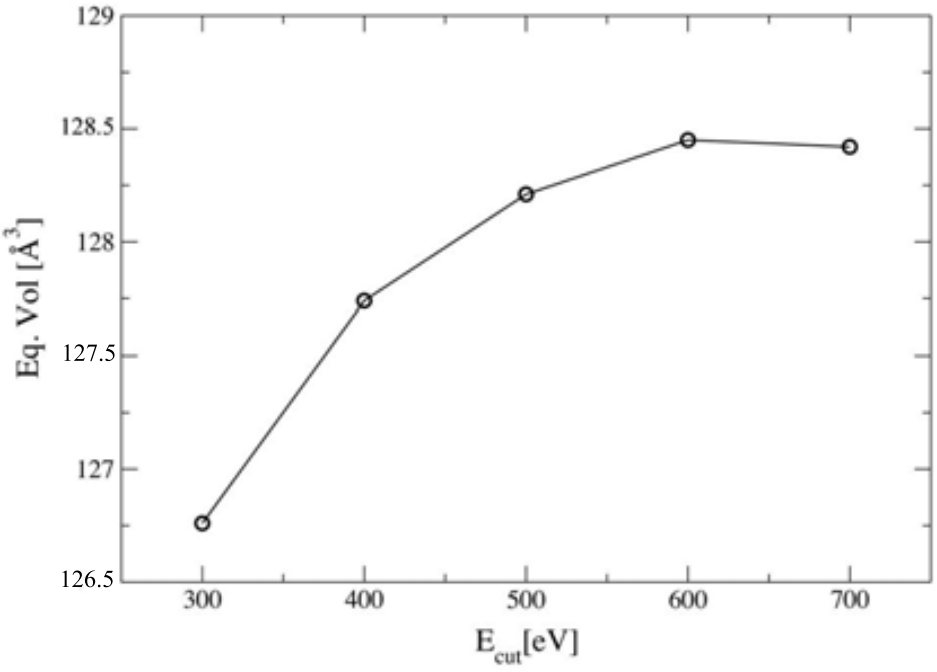

Figure 1.3: Convergence of the equilibrium Volume with respect to the Energy cutoff for a $3 \times 3 \times 3$ grid of k-points for the $BiFeO_3$ ground state

$3 \times 3 \times 3$			500 eV		
300 eV	400 eV	500 eV	$3 \times 3 \times 3$	$4 \times 4 \times 4$	$5 \times 5 \times 5$
56.8	56.6	**57.0**	**57.0**	56.8	56.8
61.0	61.0	**61.2**	**61.2**	61.1	61.1
72.1	72.1	**72.2**	**72.2**	72.2	72.2
72.3	72.4	**72.5**	**72.5**	72.5	72.5
85.8	85.6	**85.6**	**85.6**	85.7	85.7
90.3	90.1	**90.2**	**90.2**	90.2	90.2

Figure 1.4: Calculated zone centered (Γ-point) phonon frequencies in cm^{-1} for $BiFeO_3$ in the ground sate (R3c with G-AFM)

We also compared the energy difference between the ferromagnetic and antiferromagnetic orders. The energy corresponding to different magnetic orders can be expected to depend strongly on the sampling of the Brillouin zone, a consequence of each magnetic order presenting differences in the electronic structure. In table 1.3, we may appreciate that the energy differences differ by no more than 0.1 meV/f.u. for the different grids tried. In this respect, it is shown in table 1.3 that the 500 eV energy cutoff and the grid $3 \times 3 \times 3$ of k-points renders a converged result for the magnetic interactions.

$(E_{AFM} - E_{FM})$ meV/ f.u			
E_{cut}	k-point grid		
	$3 \times 3 \times 3$	$4 \times 4 \times 4$	$5 \times 5 \times 5$
400 eV	-284.4	-284.4	-284.4
500 eV	$\mathbf{-284.5}$	-284.5	-284.4
600 eV	-284.3	-284.3	-284.5

Table 1.3: Energies differences between the the G-Antiferromagnetic and Ferromagnetic orders. We ratify then the $3 \times 3 \times 3$ grid of k-points and the 500 eV energy cutoff are accurate enough to describe the system.

As we have shown a careful study involving the fundamentals quantities of interest need to be done to ensure that the calculation conditions are optimal. In this work we will be dealing with phase transitions, metastable phases with different structural and/or magnetic orders, etc. which requires an accurate description of the system. Here we have determined the converged conditions for $BiFeO_3$ calculations that will be used in this work (except where indicated).

Chapter 2

Magnetoelectric Multiferroics

This work is about magnetoeltric multiferroics, a relatively new class of materials discovered by the mid of the past century, which involve simultaneously ferroelectricity and magnetism. Ferroelectric materials exhibit spontaneous polarization that can be reverted (switched) by an applied electric field, as happens to ferromagnets with magnetization and magnetic fields. The simultaneous presence of these two properties in a single material is something difficult to meet in nature. If we add the existence of a coupling between the order parameters, the phenomena becomes even more exotic and fascinating.

The term multiferroic was defined by Schmid for the first time as: *Single-phase multiferroic materials are those that posses two or all three of the ferroic properties (ferroelectricity, ferromagnetism, and ferroelasticity)* [79]. However this definition has been broadened to include materials that present any type of long range magnetic order (ferromagnetism, ferrimagnetism, or anti-ferromagnetism), spontaneous electric polarization and/or ferroelasticity [24]. Such materials are of great interest for their potential technological applications and the basic science behind these phenomena.

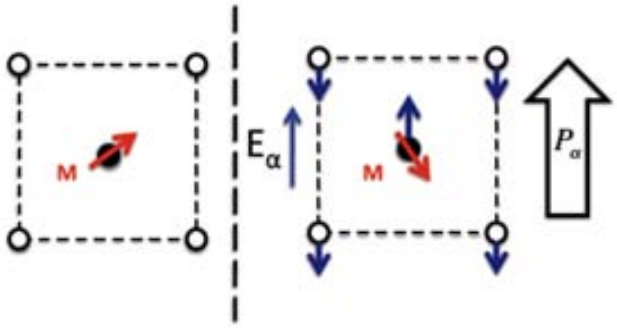

Figure 2.1: Simplified model of ME effect, coupled magnetization M and polarization P, turning on a strongly enough electric field E induce a polarization and a change in the magnetization

Another concept that will be important for our objective is the magnetoelectric effect. The property of a material to react to magnetic (electric) field undergoing a change in the polarization (magnetization) it is known as magnetoelectricity, (see Fig. 2.1). The idea of a system

with such a behavior at room conditions opens the path for a wide range of technological applications. The basic science behind their complex behavior and their possible implications for technological applications have merged together the interest in this materials, making this a very active field of research nowadays. It is in this scenario where our project takes place, with the study and search for strategies that enhance the response of one of the most promising magnetoelectric multiferroic materials, $BiFeO_3$.

2.1 Fundamentals

2.1.1 Ferroelectricity

Ferroelectric materials as already mentioned, are those that exhibit a spontaneous polarization that can be switched under an applied electric field. Certain conditions need to be present in a material to present such properties. One of the conditions to exhibit spontaneous polarization is that the crystal symmetry must be polar (non-centrosymmetric), polarization thus is associated with the loss of the inversion symmetry in the crystal. As for the polarization to be switchable, there has to be a path linking two different minima with the same polar symmetry and energy but with the polarization pointing along different directions, (see Fig. 2.2). This switching of the polarization is confirmed in the system by the presence of a polarization vs electric field (P vs. $\mathcal{E}$) hysteresis loop.

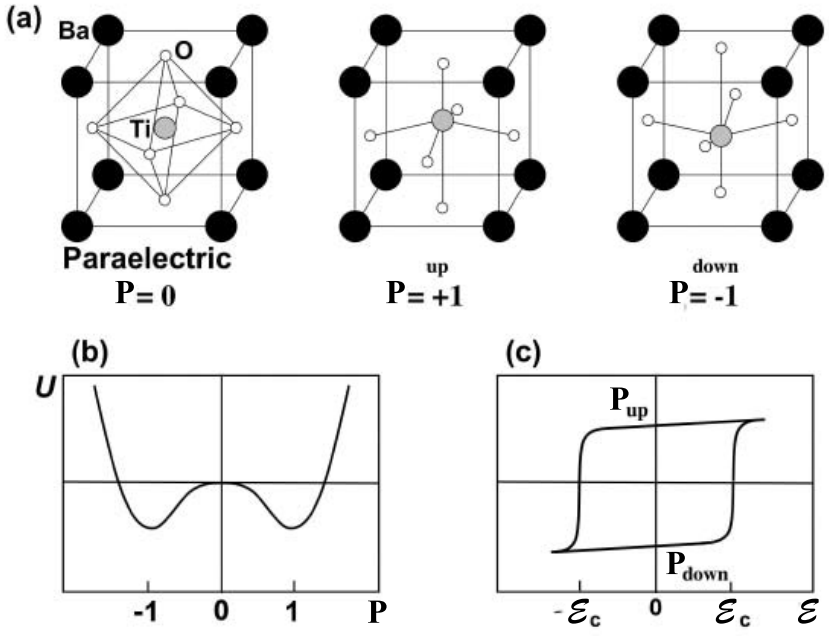

Figure 2.2: (a) $BaTiO_3$ in its high temperature paraelectric (PE) cubic perovskite structure and in its room temperature tetragonal structure (for **up** and **down** polarization states). (b) Typical double-well shape for the internal energy of $BaTiO_3$ in terms of the order parameter P. (c) Hysteresis loop of the polarization-electric field curve

The symmetry breaking from the non-polar paraelectric (PE) structure and the ferroelectric structure can be described in a Landau theory with the polarization as the order parameter.

In the vicinity of the phase transition, the Landau potential (F) can be expanded in powers of the the polarization P, with coefficient that can be fitted to reproduce experimental results or obtained from calculations. We chose the origin of energy for the paraelectric high symmetry phase to be zero:

$$\mathcal{F}(P;\mathcal{E}) = \frac{1}{2}AP^2 + \frac{1}{4}BP^4 + \frac{1}{6}CP^6 - \mathcal{E}P \tag{2.1}$$

where the expansion is truncated at sixth order. In this equation, $\mathcal{F}$ is the free energy density and is related to F by $\mathcal{F} = \frac{F}{\Omega}$ with Ω the unit cell volume; $\mathcal{E}$ is the electric field and the coefficients A, B and C define the energy profile.

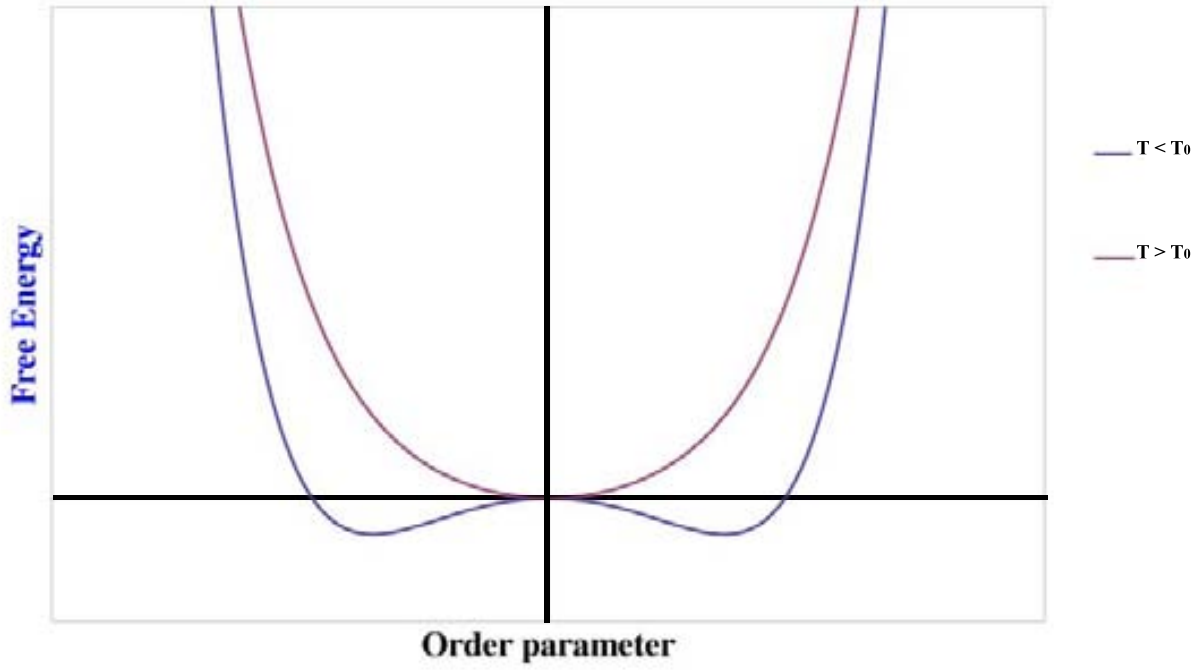

Figure 2.3: Second order phase transition, energy profile for $B > 0$

At the equilibrium structure the condition:

$$\frac{\partial \mathcal{F}}{\partial P} = 0 \qquad \& \qquad \frac{\partial^2 \mathcal{F}}{\partial P^2} > 0 \tag{2.2}$$

must be satisfied. Usually the temperature dependence of the Landau potential is restricted to the coefficient $A = A_0(T - T_0)$, with T_0 the temperature at which the coefficient A changes sign (i.e., the paraelectric phase is no longer a local minima). T_0 may coincide with the Curie temperature, but this is not always the case. We can generally assume that coefficients A_0 and C are positive. The profile of the energy will change significantly with the sign of B, which determines whether the transition between the ferroelectric and paraelectric phases will be of first or second order.

For $B > 0$, the phase transition at $T = T_0$ is of second order, the energy profile will evolve from that of a single well to a double potential well as the temperature is decreased (see Fig. 2.3). As the temperature is lowered, a polar phonon becomes softer until it gets to zero frequency and freezes below T_C (with $T_C = T_0$). As the atomic displacement corresponding to the polar phonon is frozen, the energy profile develops a double potential well. There is a close relation between the response of the system and the softening of the polar mode; this will be discussed in more detail later in this chapter, (see section 2.2).

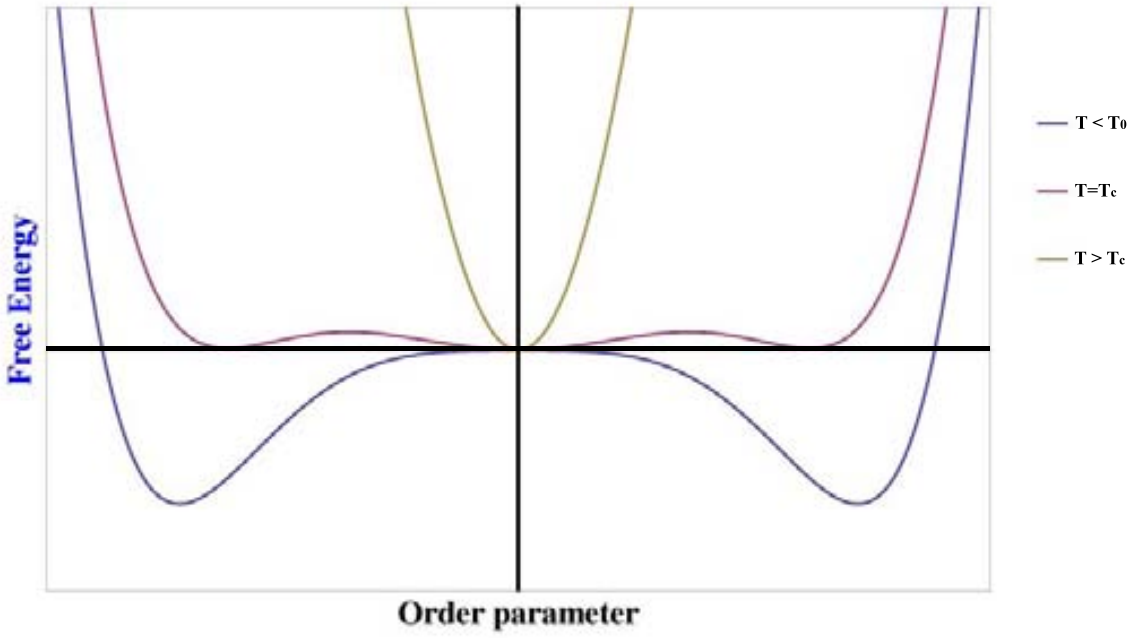

Figure 2.4: First order phase transition, energy profile for $B < 0$

The case where $B < 0$ shows a different behavior. For such systems the energy profile changes from a three minima situation to the double potential well. Note that, even at $T < T_C$ the system has a minima at the non-polar phase. In this case, the Curie temperature T_C and T_0 do not coincide; instead we have $T_C = T_0 + B^2/4A_0C$ (see Fig. 2.4). At temperatures above T_C there is a single minimum, the paraelectric state. For $T_0 < T < T_C$ the paraelectric phase and the ferroelectric phase coexist as minima; in this region the phase transition between the paraelectric and ferroelectric structures is of first order (there is a discontinuous change in the properties related to the first derivative of the free energy of the system at the transition, e.g. Polarization). For temperature below T_0 the system only exhibit the polar minima.

2.1.2 Magnetism

Magnetism is an old concept. However, the microscopic origin of this ancient phenomena was not clearly understood until the discovery of the electron and the development of the Quantum theory. The atomic structure, the electronic orbital momentum and spin, revealed the origin of this phenomenon. Magnetism appears in systems in which some of the electrons

are ordered according to their orbital component of the angular momentum and/or spin. For examples when the number of up and down spin electrons is not equal, the system is said to be magnetic (or have a net magnetic moment). For the purpose of this thesis, we will be only concerned with spin magnetism.

Ions, for instance transition metals (TM), with partially filled $3d$-shells ($l = 2$) have 5-fold degenerated orbitals ($2l + 1$ degenerate levels), that can be double occupied (by *up* and *down* spin oriented electrons). When filling this orbitals the electrons intend to align their spins and avoid the double occupancy of the same atomic orbital. The reason for such arrangement is that when two electrons populate the same atomic orbital (with spin *up* and *down*), their wavefunction will spatially overlap, resulting in an increase of the Coulomb repulsion. If instead they align occupying different orbitals the energy cost is reduced with the decrease of the Coulomb repulsion, (Hund s first rule).

In condense matter, systems that are composed of magnetic ions may display a certain order in the arrangement of the magnetic moments. The magnetic moments tend to align or anti-align depending on the interaction between the magnetic species. Depending on this ordering the system may exhibit a net magnetization (the sum of all magnetic moments is non zero) in the *ferromagnetic and ferrimagnetic order*, or not, like in the case of the *antiferromagnetic order*.

The materials that have all magnetic moments aligned and pointing in the same direction are known as *ferromagnetic*. Ferromagnets display an spontaneous magnetization that can be reversed under the influence of a magnetic field. They exhibit a hysteresis loop for the dependence of the magnetization in the magnetic field. While in the *antiferromagnetic* materials there is no net magnetization, as all the spins are anti-aligned to cancel out the magnetization. *Ferrimagnetic* materials are those in which the local magnetic moments of the atoms on different sublattices are opposed to each other, just as happens with antiferromagnetism. However, the magnetic moments of the opposed sublattices are unequal (they may consist of different chemical species like in the case of Bi_2FeCrO_6, or ions as in the case of Fe^{2+} and Fe^{3+}) and, thus, the cancelation is not complete, which leads to a remaining magnetization despite the anti-alignment of the spins.

Transition metal oxides (TMO) are a special case of magnetic materials. These materials exhibit a wide variety of magnetic properties: ferromagnetism, antiferromagnetism, colossal magnetoresistance, superconductivity, half metallicity, among others. When the transition metal ions are placed in a crystal, like in the case of the transition metal oxides, the spherical symmetry of the isolated atom is lost and the orbital degeneracy is lifted. Depending on the symmetry of the crystal, the splitting will favor certain electronic configuration. In the case of a transition metal surrounded by an ideal oxygen octahedra, like in perovskite oxides (see Fig. 1.1), the 5-fold orbital degeneracy of the $3d$ levels will be lifted favoring the t_{2g} over the e_g[1]. If the splitting Δ is too large the energy cost to populate the e_g may be larger than that of the double occupancy of the t_{2g} (see Fig. 2.5 for more details), which may result in the so-called low-spin configuration.

Another role of the oxygens in the TMO is to participate in the magnetic interaction between

[1] $3d$ orbitals may be classified by symmetry as $e_g(d_{x^2-y^2}, d_{z^2})$ and $t_{2g}(d_{xy}, d_{xz}, d_{yz})$

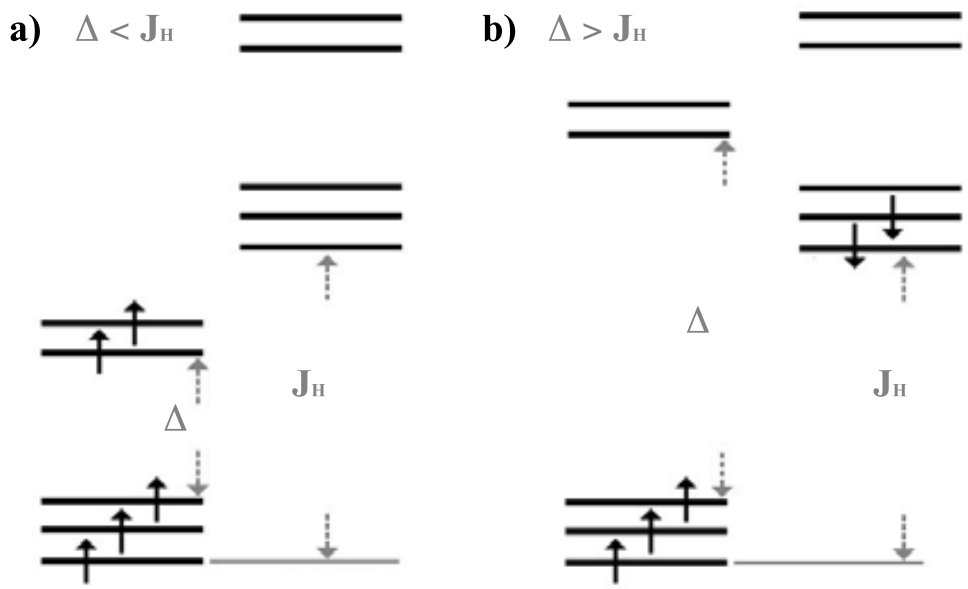

Figure 2.5: Example of orbital degeneracy lifted for the $3d$ levels in Fe^{3+} (5-$3d$ electrons), If the splitting Δ of the levels is smaller than the energy cost of the double occupancy, the system will populate all the orbitals (known as *High Spin* configuration); Otherwise if Δ is too large, the system will accommodate the electrons in the low lying orbitals t_{2g} (known as the *Low Spin* configuration

the TM atoms. These magnetic interaction can be explained making use of the Hubbard model for the d electrons:

$$H_{hub} = -\sum t_{ij} c^{+}_{i\sigma} c_{j\sigma} + U \sum n_{i\uparrow} n_{i\downarrow} \tag{2.3}$$

The first term describes the kinetics of the system, with the t_{ij} the matrix describing the probability of an electron hopping from site i to site j. The $c^{+}_{i\sigma}$ and $c_{j\sigma}$ are creation and annihilation operators of electrons at sites i and j respectively, and with spin σ. The second term is the Coulomb potential, where U is the magnitude of the on-site Coulomb repulsion, with $n_{i\uparrow}$ and $n_{i\downarrow}$ the spin-up and spin-down electron occupation of the site i.

We are interested in the case of Mott-Hubbard insulators ($U >> t$), where these systems can be described in perturbation theory.[2]. Consider a system with $U >> t$ and $n_e = 1$ (i.e. the system is insulator and have one localized d-electron per site, see Fig. 2.6). If we find the energy correction ΔE for second order perturbation theory in $t/U << 1$, we obtain for the case (a) $\Delta E = 0$ as the hopping from site i to site j is forbidden by Pauli exclusion principle. In contrast, for case (b) the hopping is allowed and we obtain $\Delta E = -\frac{2t^2}{U}$. As a result, the configuration with the antiferromagnetic order is favored. A similar result can be obtained for the case of TMO where the TM atoms are linked by an oxygen, where the localized $3d$ electrons of the TM atoms overlap with the same p orbital of the intermediate oxygen. These interactions that are mediated by virtual electron transfers between the TM atoms and/or between a shared anion and the two TM atoms are known as superexchange mechanism.

[2]a pedagogical explanation can be found in [**?**]

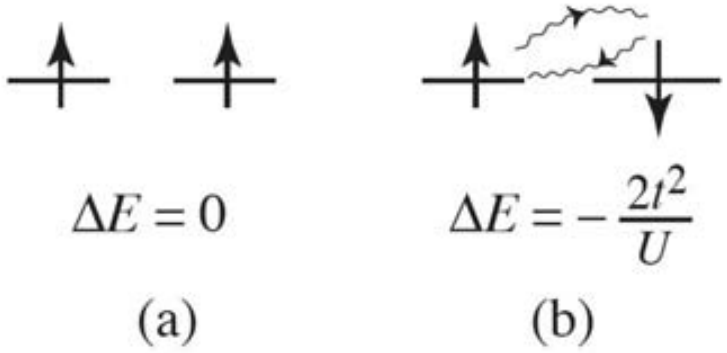

Figure 2.6: Simple model to explain the magnetic interaction between the atoms. Consisting of a system with $U >> t$ (insulator) and one localized d-electron per site).There are two relevant scenarios: (a) spins are aligned with ferromagnetic interaction between the two sites and, (b) spins are antiparallel and the interaction is antiferromagnetic.

Different orbital orientations and geometry of the bonding will result in a different overlaps between the orbitals, thus changing the exchange interaction. There is a set of rules known as the *Goodenough-Kanamori-Anderson rules* (GKA) that were formulated to predict how this exchange interaction should be according to the geometry of the bonding between TM atoms and the oxygen. [37, 51]

2.1.3 Magnetoelectric coupling

The magnetoelectric effect is a phenomenon in which the magnetization(polarization) is coupled to the electric (magnetic) field. It can be defined if we expand the free energy in terms of the electric $\mathcal{E}$ and magnetic $\mathcal{H}$ fields:

$$\mathcal{F}(\mathcal{E},H) = -\sum_i P_i^S \mathcal{E}_i - \sum_j M_j^S \mathcal{H}_j + \frac{1}{2}\sum_{ii'} \chi^d_{ii'} \mathcal{E}_i \mathcal{E}_{i'} + \frac{1}{2}\sum_{jj'} \chi^m_{jj'} \mathcal{H}_j \mathcal{H}_{j'} + \sum_{ij} \alpha_{ij} \mathcal{E}_i \mathcal{H}_j + \sum_{ijj'} \frac{\beta_{ijj'}}{2} \mathcal{E}_i \mathcal{H}_j \mathcal{H}_{j'} + \sum_{ii'j} \frac{\gamma_{ii'j}}{2} \mathcal{E}_i \mathcal{E}_{i'} \mathcal{H}_j + ... \quad (2.4)$$

where P_i^S and M_j^S are the spontaneous polarization and the magnetization in the direction i or j respectively. The $\chi^d_{ii'}$ and $\chi^m_{jj'}$ tensors are the dielectric and magnetic susceptibilities of the medium. The rest of the terms are those involved in the magnetoelectric effect: α is the linear magnetoelectric coupling, with β and γ being higher-order (quadratic) terms of the magnetoelectric coupling. By dropping the higher-order coupings, β and γ, we can write:[3]

$$\mathcal{F}(\mathcal{E},\mathcal{H}) = -\sum_i P_i^S \mathcal{E}_i - \sum_j M_j^S \mathcal{H}_j + \frac{1}{2}\sum_{ii'} \chi^d_{ii'} \mathcal{E}_i \mathcal{E}_{i'} + \frac{1}{2}\sum_{jj'} \chi^m_{jj'} \mathcal{H}_j \mathcal{H}_{j'} + \sum_{ij} \alpha_{ij} \mathcal{E}_i \mathcal{H}_j \quad (2.5)$$

[3]There are some works dedicated to the study of higher order effects [77, 78], but most of the literature about ME refers to the linear effect.

From Eq. (2.5) we can derive the dependence of the polarization P of the magnetic field H,

$$P_i(\mathcal{E},\mathcal{H}) = -\frac{\partial \mathcal{F}}{\partial \mathcal{E}_i} = P_i^S + \frac{1}{2}\sum_{i'} \chi^d_{ii'}\mathcal{E}_{i'} + \sum_j \alpha_{ij}\mathcal{H}_j \tag{2.6}$$

similarly for the dependence of M on the electric field $\mathcal{E}$,

$$M_j(\mathcal{E},\mathcal{H}) = \frac{\partial \mathcal{F}}{\partial \mathcal{H}_j} = M_j^S + \frac{1}{2}\sum_{j'} \chi^m_{jj'}\mathcal{H}_{j'} + \sum_i \alpha_{ij}\mathcal{E}_i. \tag{2.7}$$

As can be noticed, in the absence of a electric (magnetic) field the polarization (magnetization) react to the magnetic (electric) field proportional to the order of α. The linear magnetoelectric coupling is bounded from above by the dielectric and magnetic susceptibilities, as:

$$\alpha_{ij}^2 < \chi^d_{ii}\chi^m_{jj} \tag{2.8}$$

which can be proven by calculating the change in the free energy that occurs when electric and magnetic fields are simultaneously applied to a magnetoelectric medium. [13] Thus, ferroelectrics and ferromagnetic materials are expected to exhibit large magnetoelectric response, as their often have a large dielectric and magnetic susceptibility respectively. It is important to stress higher-order magnetoelectric effects are not limited by this upper bound. [24]

Note also that a linear magnetoelectric is not necessarily a multiferroic material. The magnetic point group (symmetry) of the material might allow spontaneous polarization in addition to the linear magnetoelectric effect, however this is not always the case (e.g. Cr_2O_3). The converse is also true: the linear ME effect is not allowed for all multiferroics (e.g. in bulk $BiFeO_3$ where the existence of an incommensurable spin cycloid forbids the linear effect).

This is a very active field of research, with new strategies to enhance this effect being explored. Part of our work is motivated in this direction. At the end of the present chapter we devote a section to mention the state of the art of this field of research.

2.2 Microscopic theory of functional properties of ME multiferroics

Magnetoelectric multiferroics exhibit various functional properties, besides the switchable spontaneous polarization, they may also display large magnetoelectric and the dielectric responses, which may make them suitable for technological applications.

We want to derive these response properties as the appropriate second derivatives of the energy E per unit volume with respect to the perturbations. In the absence of strain, let us consider the energy $E(\{u_n\})$ per undeformed unit cell volume (Ω) as a function of the infrared (IR) modes of the material, which can be obtained from diagonalization of the force-constant matrix at the Γ point of the Brillouin zone (BZ). Let us denote by u_n the amplitude of the n-th IR mode, with n running from 1 to N_{IR}. In the presence of applied electric ($\mathcal{E}$) and magnetic ($\mathcal{H}$) fields, it is convenient to Legendre transform $E(\{u_n\})$ into the *electric-magnetic enthalpy*

$F(\{u_n\};\mathcal{E},\mathcal{H})$. This enthalpy is expanded to second order around the zero-field equilibrium structure, [46] as:

$$\begin{aligned} F(\{u_n\},\mathcal{E},\mathcal{H}) =& F_0 - \sum_i P_i^S \mathcal{E}_i - \sum_j M_j^S \mathcal{H}_j + \frac{1}{2}\sum_{ii'} \chi^d_{ii'} \mathcal{E}_i \mathcal{E}_{i'} + \frac{1}{2}\sum_{jj'} \chi^m_{jj'} \mathcal{H}_j \mathcal{H}_{j'} + \sum_{ij} \alpha_{ij} \mathcal{E}_i \mathcal{H}_j \\ & - \sum_i P_i^{latt}(\{u_n\})\mathcal{E}_i - \sum_j M_j^{latt}(\{u_n\})\mathcal{H}_j + \frac{1}{2}\sum_n \kappa_n u_n^2. \end{aligned} \tag{2.9}$$

Here F_0 is the reference structure energy; $\mathcal{E}_i$ and $\mathcal{H}_j$ are the electric and magnetic fields along the direction i (j); P_i^S and M_j^S are the the spontaneous polarization and magnetization, respectively; $\chi^d_{ii'}$, $\chi^m_{jj'}$ and α_{ij} are the frozen-ion contributions to the dielectric susceptibility, magnetic susceptibility and magnetoelectric response, respectively. Finally, P_i^{latt} and M_i^{latt} are the contributions to polarization and magnetization arising from distortions of the equilibrium structure associated to IR modes, as given by,

$$P_i^{latt}(\{u_n\}) = \frac{1}{\Omega}\sum_n p^d_{ni} u_n, \qquad and \qquad M_j^{latt}(\{u_n\}) = \frac{1}{\Omega}\sum_n p^m_{nj} u_n, \tag{2.10}$$

Here, p^d_{ni} is the *mode polarity* that measures the polarization induced by the n-th mode eigendisplacement,$\xi^n_{\tau i}$, with

$$p^d_{ni} = \sum_{\tau i'} Z_{\tau,ii'} \xi^n_{\tau,i'}, \tag{2.11}$$

where $\xi^n_{\tau i}$ is the component along the direction i' of the atom τ, and $Z_{\tau,ij}$ are the *Born effective charges*,

$$Z_{\tau,ii'} = -\Omega \frac{\partial P_i}{\partial r_{\tau,i'}} \tag{2.12}$$

$Z_{\tau,ij}$ is a fundamental quantity in the study of dynamical properties of polar crystals, and is defined as the change in the polarization P_i with respect to the displacement of the atom τ along the direction i'. We can define a magnetic equivalent for the mode polarity and Born charges just mentioned, which would have the forms

$$p^m_{nj} = \sum_{\tau j'} \zeta_{\tau,jj'} \xi^n_{\tau j'} \quad \text{and} \quad \zeta_{\tau,jj'} = -\Omega \frac{\partial M_j}{\partial r_{\tau,j'}} \tag{2.13}$$

The last term in Eq. (2.15) quantifies the energy cost associated to the IR modes, with κ_n being the stiffness of the n-th IR mode (i.e., the eigenvalue of the force constant matrix).

Dielectric response in ferroelectrics is mainly driven by the lattice mediated contributions, with the purely electronic contribution being a small part of the total response. In order to account for such contributions we need to introduce the functional $F(\mathcal{E},\mathcal{H}) = \min_u F(\{u_n\},\mathcal{E},\mathcal{H})$. Which can be obtained from the condition $\partial F/\partial u_n = 0$, which leads to the the relation:

$$u_n = -\sum_i \frac{p^d_{ni}\mathcal{E}_i + p^m_{ni}\mathcal{H}_i}{\kappa_n}. \tag{2.14}$$

By replacing in Eq. (2.15) the result for the u_n we obtain,

$$\begin{aligned} F(\mathcal{E},\mathcal{H}) =& F_0 - \sum_i P_i^S \mathcal{E}_i - \sum_j M_j^S \mathcal{H}_j + \sum_{ii'} (\frac{1}{2}\chi^d_{ii'} + \frac{1}{\Omega}\sum_n \frac{p^d_{ni}p^d_{ni'}}{\kappa_n})\mathcal{E}_i\mathcal{E}_{i'} \\ &+ \sum_{jj'} (\frac{1}{2}\chi^m_{jj'} + \frac{1}{\Omega}\sum_n \frac{p^m_{nj}p^m_{nj'}}{\kappa_n})\mathcal{H}_j\mathcal{H}_{j'} + \sum_{ij}(\alpha_{ij} + \frac{1}{\Omega}\sum_n \frac{p^d_{ni}p^m_{nj}}{\kappa_n})\mathcal{E}_i\mathcal{H}_j \end{aligned} \tag{2.15}$$

a new set of response functions now including the ions relaxations (i.e. the lattice contribution to the response). For instance now the dielectric susceptibility will have the form:

$$\chi^d_{ij} = \frac{\partial^2 F}{\partial\mathcal{E}_i\partial\mathcal{E}_{i'}} = \chi^d_{ii'} + \frac{1}{\Omega}\sum_n \frac{p^d_{ni}p^d_{ni'}}{\kappa_n} \tag{2.16}$$

Analogously we find,

$$\alpha_{ij} = \frac{\partial^2 F}{\partial\mathcal{E}_i\partial\mathcal{H}_j} = \alpha_{ij} + \frac{1}{\Omega}\sum_n \frac{p^d_{ni}p^m_{nj}}{\kappa_n} \tag{2.17}$$

From these equations we can see that the response will be ver large for the cases where $\kappa_n \to 0$ (i.e., if we reduce the energy cost for the distortions).

So far we have shown how the magnetoelectric coupling and the dielectric response can be expressed in terms of the mode polarities (electric and magnetic) and the force-constant matrix eigenvalues. This is a desirable picture that lead to a better understanding of how the dynamics of the lattice may affect the responses of the system. In this way the response can be related to the phase transitions and the softening of the polar modes that accompany the transition.

2.3 Difficulties to obtain ME multiferroics at room temperature and contributions from first principles theory

2.3.1 Scarcity of materials and small responses

According to Eq. (2.8), we can see that achieving a very large ME response requires finding materials with a large dielectric and/or magnetic susceptibility. The largest dielectric responses are found in ferroelectrics, while in ferromagnetic materials we observe the largest magnetic susceptibilities. From this we may think about ferromagnetic ferroelectrics as the best candidates for displaying giant ME effects. Besides ferromagnetic ferroelectrics many other multiferroics (with antiferromagnetic or ferrimagnetic orders) are also promising systems for large ME response.

According to Fiebig, we may classify the multiferroics in four major groups [28]:

- *Compounds with perovskite structure:* The first known multiferroic $PbFe_{1/2}Nb_{1/2}O_3$ and $PbFe_{1/2}Ta_{1/2}O_3$ [**?**] and some of the best studied multiferroics have the perovskite structure. Most of the compounds have either ABO_3 or $A_2BB\,O_6$ as the general chemical formula, and the variety of existing compounds is greatly enriched by chemical substitution (mostly $AB_{1-x}B_xO_3$).These materials usually exhibit a distorted unit cell of the ideal cubic perovskite. The compound that has been most extensively studied is $BiFeO_3$ [15], which is ferroelectric, ferroelastic and antiferromagnetic, and it is rhombohedrally distorted with $R3c$ space group. Interestingly, this compound displays a very high electric and magnetic ordering temperatures of $T_C \sim 1100$ K and $T_N \sim 650$ K respectively, which has stimulated the study and growth of a large variety of solid solutions based on $BiFeO_3$ [15].

- *Compounds with hexagonal structure:* In the case of sufficiently small cationic radii compounds with the general formula ABO_3 or $A_2BB\,O_6$ may crystallize in a hexagonal structure instead of the typical perovskite. The largest and best known group of hexagonal multiferroics is the one composed by the ferroelectric antiferromagnetic manganites $RMnO_3$ with R = Sc, Y, In, Ho, Er, Tm, Yb, Lu. [17] Their crystallographic point symmetry is $6mm$. Here we can find up to four long-range ordered subsystems: the ferroelectric lattice with a Curie temperature of $570 - 990$ K, the antiferromagnetic Mn^{3+} lattice with a Neel temperature of $70 - 130$ K [8] and two rare-earth sublattices with a magnetic ordering temperature of ~ 5 K [82].

- *Boracites:* Boracite compounds with the general formula $M_3B_7O_{13}X$ are ferroelectric ferroelastic antiferromagnets, in some cases exhibitng a weak ferromagnetic moment. With M = Cr, Mn, Fe, Co, Cu, or Ni as the bivalent ion and X = Cl, Br, or I, a large variety of compounds exists, many of which possess a ferroelectric Curie temperature above room temperature, whereas the magnetic ordering temperature never exceeds 100 K [87].

- *Fluorites:* Multiferroics of composition $BaMF_4$ with M = Mg, Mn, Fe, Co, Ni, and Zn, were introduced and discussed in detail by Guggenheim and Scott [25, 80]. The compounds are orthorhombic with $2mm$ point symmetry at high temperatures with an extrapolated Curie temperature above the melting point. With a magnetic ordering temperature around $25 - 70$ K the ferroelectric structures display purely antiferromagnetic or weak ferromagnetic ordering.

The classification given above was done in the 2005, but can be considered essentially valid nowadays. Besides the examples listed here, there is a general difficulty in having electric and magnetic long-range ordering in one compound. The number of multiferroic compounds that are known is relatively small. Most of them are antiferromagnetic ferroelectrics, and the preferred combination of ferromagnetism and ferroelectricity is only achieved in the form of weak ferromagnetism or weak ferroelectricity accompanying the otherwise antiferroic order.

2.3.2 Computational studies on how to achieve ME multiferroism

Magnetoelectric multiferroics are a rather difficult to find class of materials. If we then add the condition of having such a behavior at room temperature, the materials are very few, and

mostly limited to compounds of the $BiFeO_3$ family ($BiFeO_3$ and solid solutions of $BiFeO_3$ with other A and B cations $Bi_{1-x}A_xFe_{1-x}B_xO_3$).

There are several points of view to address the problem of these complex materials where ferroelectricity and magnetism take place simultaneously, and furthermore they are coupled. In this section we will give a briefing on what we consider a representative sample of the works in the field of first principles studies of magnetoelectric multiferroic materials.

The works by Nicola Spaldin were very influential in the field of magnetoelectric-multiferroics. Spaldin discussed why there are so few materials that are magnetic and ferroelectric [43]; limiting her analysis to transition-metal oxides (TMO), especially perovskites. She observed that the ferroelectrics (e.g., titanates) have B-site ions with $3d^0$ electronic configuration of the transition metal (TM) atom, whereas the magnetic materials require $3d^n$ unpaired electrons. This is the case of $BiFeO_3$, where the polarization is mostly due to the lone pair (s^2 orbital) of Bi^{+3}, so that the polarization comes mostly from the A-site while the magnetization comes from the B-site (Fe^{+3}). With this in mind, Spaldin and co-workers proposed the perovskite Bi_2FeCrO_6 with A-site ferroelectricity (Bi) and mixing magnetic cations (Fe/Cr) at the B-site, [4] resulting in a ferrimagnetic order from the partial cancelation of the anti-aligned lattices of Fe and Cr. among others, Spaldin s works refueled the activity in the field and many groups started working in this family of materials.

Contrary to the hypothesis followed by *Spaldin et al.* that ferroelectricity requires d^0-ness while magnetism requires partial d-state occupancy, a recent work by *Ghosez et al.* proved that this affirmation is not necessarily true. They showed that the cubic perovskite structure of $CaMnO_3$ also exhibits a weak ferroelectric instability due to the Mn^{4+} ions. [9] This ferroelectric instability remains suppressed by a much stronger antiferrodistortive (AFD) instability which is the responsible for the paraelectric (PE) ground state. Nevertheless, ferroelectricity can be favored by epitaxial strain or chemical substitution, as in a hypothetical $BaMnO_3$ with perovskite structure. These works have opened a new paths that were assumed to be a dead end for the design of new multiferroics.

Another path explored to find candidates that exhibit the linear magnetoelectric effect was the work by *Rondinelli et al.*. In this work, they have proposed an strategy to enable the linear ME coupling by appropriately breaking the symmetry at the interface of two oxides. [74] They have found a carrier mediated response at the interface between a ferromagnetic metal and a non-polar dielectric oxide. Although the observed effect was small it opened a new guideline for the design of potential candidates for magnetoelectric devices.

Finally, it is worth to mention the works by Fennie; much has been done by his group in strain engineering (i.e., tuning the materials properties by applying strain), and in the search of new candidates that exhibit multiferroicity. For example the works in the polarization-strain coupling of the multiferroic $EuTiO_3$. In this material they showed how the predicted competition between an antiferromagnetic- paraelectric (AFM-PE) phase and a ferromagnetic-ferroelectric phase allows magnetic phase control with an applied electric field, and electric phase control with an applied magnetic field, with modest critical fields. More recently, they have proposed a mechanism named by them as *hybrid improper ferroelectricity* to explain the ferroelectricity induced by the rotation patterns of the oxygen octahedra for layered perovskites of the type

$A_{n+1}B_nO_{3n+1}$. They discussed how these octahedra rotations simultaneously induce ferroelectricity, magnetoelectricity and weak ferromagnetism for the $Ca_3Mn_2O_7$, and proposed the strain as a via to control the magnetism in the system.

2.3.3 Improving the ME response at room temperature

In this thesis we want to discuss some of the possible strategies to enhance the response in ME multiferroics (more specifically in $BiFeO_3$, our candidate of choice). Thus, we will discuss different strategies that may lead to an enhancement of the response in this material, the different mechanisms involved in such enhancements, and how are related to the work we are presenting here. We begin by describing the different strategies to enhance what we call the *normal response*, i.e. the usual linear magnetoelectric coupling defined above.

Normal response

As we have mentioned before, the linear magnetoelectric coupling can be expressed in terms of a lattice mediated part and a purely electronic contribution see Eq. (2.17). Now lets analyze the terms contributing to α_{ij} and see how we can tune the material to maximize their contributions.

For the purely electronic part, one should try to have an electronically soft system, like for instance the electronic ferroelectric $LuFe_2O_4$ [49]. The problem with these systems is that the relevant energy scale is typically of the order of the band gap. In order to enhance this electronic response is desirable for the material to have a small band gap, which makes it less suitable for applications.

Another way is to bring the magnetic ordering temperature T_N close to room temperature (T_r). For instance, having $T_N \gtrsim T_r$ results in a strongly fluctuating spin system at T_r, which should lead to an enhancement of the ME response via the mechanism discussed by Mostovoy et al. [62].

The remaining possibilities are in the lattice mediated part, which depends on several material properties. It is proportional to the Z^* Born effective charges, or its magnetic equivalent ζ. There is no much room for improvement for the Z^*, as this electro-structural coupling depend on the ionization charges and they are already anomalously large in most ferroelectric perovskites [29, 95]. In the case of the ζ, one possibility is to use heavy magnetic species that present stronger spin-orbit effects. But then transition metals with extended $4d$ and $5d$ orbitals tend to result in a metallic behavior. On the other hand, if rare earths are employed, the magnetic ordering temperatures tend to be very low.

We are left then with the lowering of κ_n (force constant matrix eigenvalues) in Eq. (2.17) as a route to enhance the response. This lowering of κ_n it is directly related to the softening of the lattice. A polar mode with an small value of κ_n has a low energy cost for the distortion associated with it. The response of the system is enhanced as this mode will react strongly to external applied fields. This can be achieved by bringing the ferroelectric (FE)

ordering temperature T_C close to T_r. For $T_C \gtrsim T_r$ the system would experience large structural deformations in response to an applied $\mathcal{E}$-field; such a structural softness would result in an enhancement of the lattice-mediated dielectric and magnetoelectric responses. [46, 89]. In fact, one expects to obtain a divergence of the lattice-mediated part of α in the vicinity to a second-order FE transition. [71, 90]

In this work we will be seeking to soften the lattice by chemical doping $BiFeO_3$ with $LaFeO_3$ as a possible solution to enhance the magentoelectric properties of $BiFeO_3$. The details can be found in chapter 4.

Phase change response

The recent experimental discovery of electric field ($\mathcal{E}$) induced transitions in epitaxially compressed BFO by *Zeches et al.* [94], has attracted attention as possibility to induce large responses in the system. This $\mathcal{E}$-switching between two very different phases (with change in cell shape, polarization direction and magnetic order) implies a possible enhanced ME response. This is the context of the works by *Dieguez et al.* [21] who proposed the solid solution $BiFe_{1-x}Co_xO_3$ (BFCO) as an alternative to the compressive strain. In their paper they discuss how the BFCO solid solution is likely to display a rhombohedral to tetragonal (R-T) morphotropic transition analogous to the one induced by epitaxial compression in BFO.

The phase-change response has a different origin from that of the softening of the lattice. Here, a large effect can be achieved from the change in the properties of the system as the external field induces a first order phase transition. This phase transition will occur between phases with different polarization directions and magnetic orders. The result is a magnetoelectric effect as the system is driven from one phase to the other.

This mechanism is relevant for the systems we will be discussing along this thesis. As we have mentioned, we are interested in the enhancement of the response properties of BFO. For that purpose we have done a thorough study of the low-energy phases in this material. We have obtained a wide variety of phases with differents space groups, polarization directions and magnetic orders. We will show how for compressive strain tetragonal phases may be stabilized, and discuss in chapter 3 the implications of our results with respect to the observed experiments by *Zeches et al.* [94]. Possible $\mathcal{E}$-field induced transitions in $BiFeO_3$-$LaFeO_3$ solid solution will also be discussed in the chapter 4.

Chapter 3

$BiFeO_3$ phases

In this chapter we will describe the structural richness of $BiFeO_3$. This compound, despite being one of the most studied multiferroics, continues to appear as one of the most fascinating materials of the day. Recently it has been shown that it displays a variety of novel fundamental effects, like an increase in conductivity at specifics domain walls [81] or new structural phases in thin films with potentially useful response properties. [94]

Furthermore, BFO s phase diagram remains unresolved, with newly reported phases as function of temperature T and/or pressure p. In the review by Catalan et al. [15], a possible p-T phase diagram was proposed. Since then, the understanding of the different phase transitions has increased and Guennou et al. [38] have recently proposed a different one (see Fig. 3.1). At ambient conditions, BFO has a rhombohedral symmetry with the $R3c$ space group, with a unit cell defined by a lattice parameter of $a_{rh} = 3.965$ Å and a small rhombohedral angle $\alpha \approx 89.3 - 89.4^o$. It is also ferroelectric with a very large polarization of $\mathbf{P} \sim 0.9$ C/cm^2 along the [111] direction of the perovskite structure (see Fig. 1.1). Around $T \approx 1098$ K, it has been observed a sudden volume contraction corresponding to a first order phase transition. At the transition it is observed a peak in the dielectric constant that has been associated to a FE to PE transition. Although this can be arguable, as the dielectric response may exhibit peaks at FE to FE transition also, as happens in the case of $BaTiO_3$ for the tetragonal to orthorhombic and orthorhombic to rhombohedral transitions. At higher temperatures $T \approx 1204$ K a second order phase transition was observed by Catalan et al. to a metallic phase that was determined from x-ray diffraction data to be cubic. However recent studies by Arnold et al. show that the cubic phase can only be expected at temperatures higher than the decomposition point of the material [3] (see Fig. 3.1(b)).

Regarding the pressure induced structural transitions, experiments from Haumont et al. have described two transitions at pressures of 3.5 and 10 GPa respectively. The first from rhombohedral to monoclinic ($C2/m$) and the second one from monoclinic to orthorhombic ($Pnma$). Theoretical calculations by Ravindran et al. [**?**] have observed a phase transition from rhombohedral to orthorhombic phase at pressures of $p = 14$ GPa, but without indications of the intermediate monoclinic phase. Experiments by Gavriliuk et al. at hydrostatic pressures up to 65 GPa report an interesting transition that simultaneously involves loss of magnetic order, high to low spin configuration transition (spincrossover) and metallization. Their results suggest a rhombohedral high pressure phase, as they did not found any significant evidence of a change in the symmetry, although they did observe a contraction of the unit cell volume. [32]

In the recent work, by Guennou et al. have shown up to four transitions at low pressures (up to 11 GPa). In this range, they observations suggest phases displaying large unit cells and complex domain structures. Between 11 and 38 GPa the non-polar Pnma phase was observed to remain stable, with two high-pressure phase transitions at 38 and 48 GPa which were marked by the occurrence of larger unit cells and an increase of the distortion away from the cubic parent perovskite cell [38].

As we have seen, the structural phases of bulk BFO corresponding to high pressure and/or high temperature regimes are not well determined and there is debate even about the nature of the phases involved in the intermediate regions.

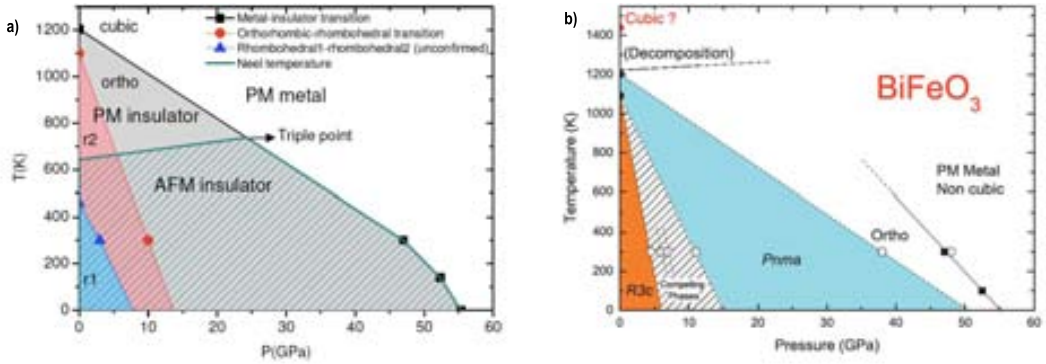

Figure 3.1: Figures taken from references [15] and [38], of the proposed phase diagrams for BFO. a) Phase diagram proposed by Catalan and Scott [15] with the high temperature and high pressure phases, having the same cubic symmetry. b) Phase diagram proposed by Guennou et al. [38] experimental observations of phase transitions at high pressure have no indications of a cubic phase, instead an orthorhombic phase was proposed.

The BFO thin films also exhibit a complex behavior. Recently Bea et al. [7] have shown that a tetragonal phase with a very large c/a can be stabilized under epitaxial strain. Then, Zeches et al. have reported the coexistence of the tetragonal and a rhombohedral phases (the latter related to the BFO ground state) on a length scale of tens of nanometers in films grown with intermediate strain displaying huge piezoelectric responses [94]. Other interesting results are those obtained by Catalan et al., who have observed the presence of a surface layer (skin layer) with a well differentiated structure from the inner crystal in BFO [**?**]. The presence of such skin layer makes more complicated the structural characterization of BFO thin films, as the surface has its own symmetry and undergoes its own phase transitions which interfere with measurements of bulk $BiFeO_3$. Thus it is important to unravel the structures that can be involved in the skin layer to better understand the properties of the material and its behavior at interfaces.

Another active direction of research pertains to BFO solid solutions with different rare earth elements or transition metals. That is the case, for instance of the $Bi_{1-x}La_xFeO_3$ solid solution investigated in this thesis work, where structural phases corresponding to the intermediate compositions are not well understood. [30, 75, 85, 93]

in our ICMAB group, while searching for the possible structural phases that may arise in the solid solutions $Bi_{1-x}La_xFeO_3$ and $BiFe_{1-x}Co_xO_3$, we performed a unbiased search for potentially stable phases of the parent compound BFO, going beyond the ones reported already in the literature. For that purpose we explored the most common distortions that take place in perovskite materials. We found a rich scenario with many structural phases that are local minima of the energy. Thus in this chapter we will present the lower energy phases obtained and describe the implications of such a structural richness.

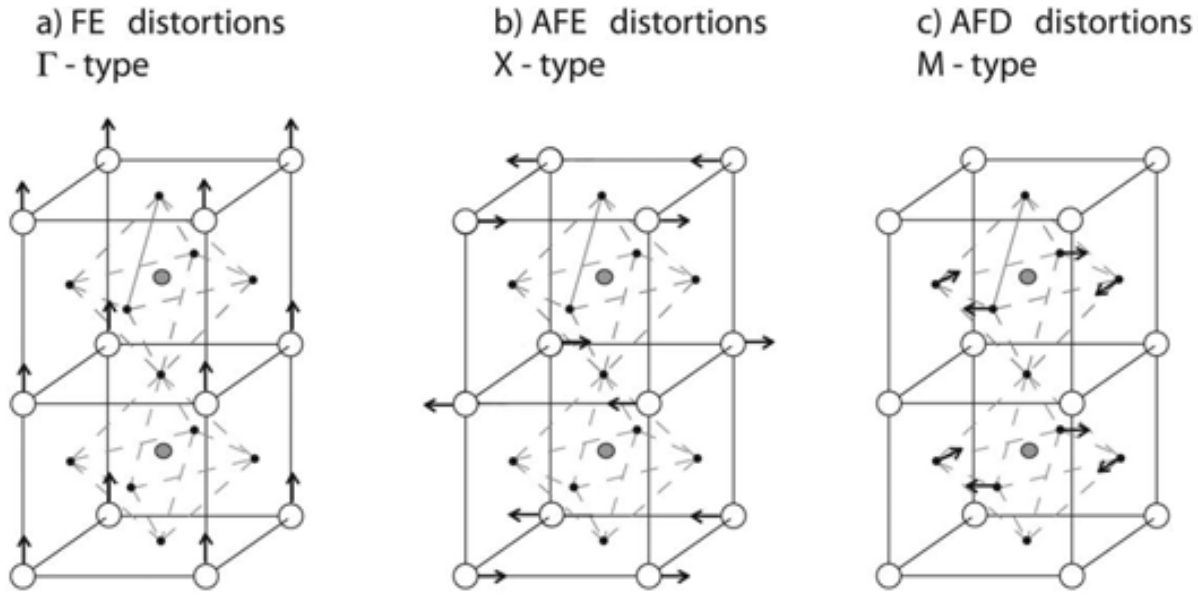

Figure 3.2: In this figure are sketched: a) ferroelectric (FE) patterns associated with irreducible representation Γ_4^- (symmetry labels correspond to the BZ of the five-atom cubic cell), b) tantiferroelectric (AFE) modes associated with zone-boundary q points (X-like, M-like, and R), and c) antiferrodistortive (AFD) patterns corresponding to any combination of in-phase (M_3^+) and antiphase (R_4^+) rotations of the O_6 octahedra around the Cartesian axes.

3.1 Comments on the computational approach

For the simulations we used the 40 atoms pseudocubic cell described in (1.2.2). This cell can be constructed by doubling the 5-atoms unit cell of the ideal perovskite structure along the cartesian directions x, y and z. Within this cell we were able to study the most common distortions from the cubic symmetry among the perovskite oxides. Among the different distortions that are common to perovskites, three major groups may be identified (see Fig. 3.2):

- Ferroelectric (FE) patterns, consisting of the coordinated displacement of the atoms sub-lattices along the same direction, FE distortions are associated to irreducible representation Γ_4^- which correspond to the Γ q-point $[q = \frac{2\pi}{a}(0,0,0)]$ of the BZ.
- Antiferroelectric (AFE) distortions, in which the atoms are displaced in an antiphase

manner canceling out the global polarization. AFE patterns can be associated to several q-points in the BZ: X $[q = \frac{\pi}{a}(1,0,0)]$, M $[q = \frac{\pi}{a}(1,1,0)]$, or R $[q = \frac{\pi}{a}(1,1,1)]$.

- Antiferrodistortive (AFD) patterns, corresponding to any combination of in-phase (M_3^+) and anti-phase (R_4^+) rotations of the O_6 octahedra around the Cartesian axes.

As has been explained before this cell is also compatible with the G- and C-antiferromagnetic orders, the former corresponding to the ground state of BFO, and the latter occurring in supertetragonal BFO s phase (see Fig. 3.3).

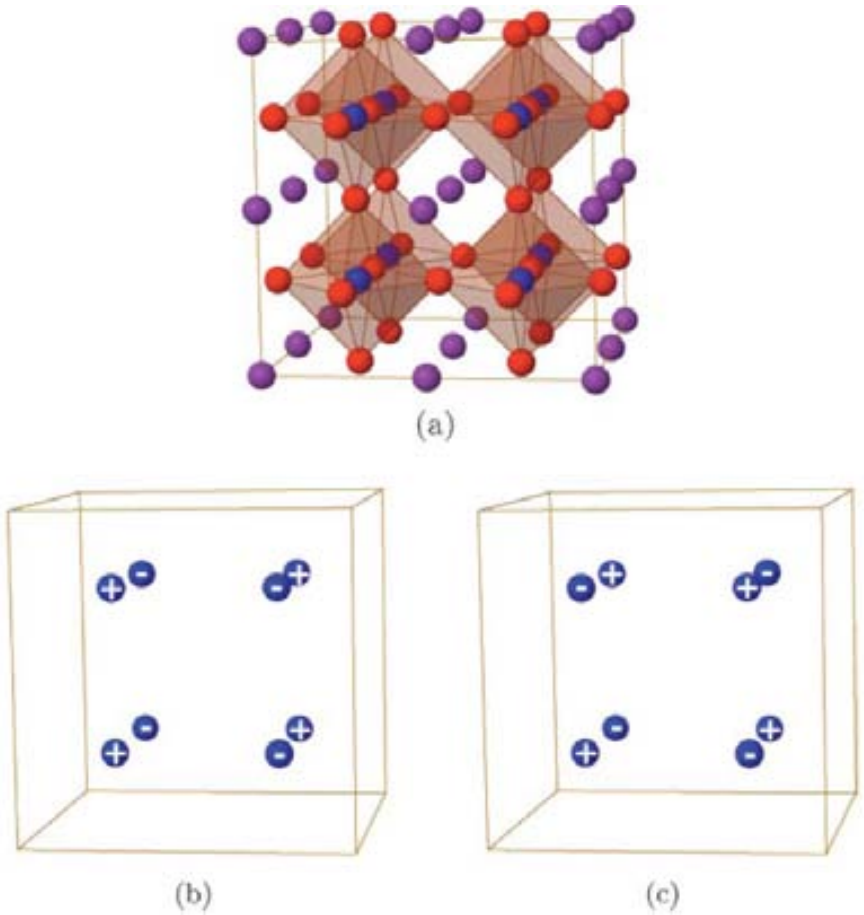

Figure 3.3: In this figure are sketched: a) the 40- atom pseudocubic cell, b) the C-antiferromagnetic order, and c) the G-antiferromagnetic order

Scheme for structural phase exploration

In order to explore all the just mentioned distortions, we needed to consider a large number of starting configurations. We have considered all the simple combinations of AFD patterns described in table 3.1 and Fig. 3.4:[1] Note that these AFD patterns include all the simple-tilt systems discussed in the crystallographic literature for simple (ABO_3) perovskites (see Fig. 3.5)

Table 3.1: All simple tilt systems used as starting point for the relaxations. Here we have employed the Glazer notation, with $a^{\circlearrowleft}b^{\circlearrowleft}c^{\circlearrowleft}$, letters refer to tilts around axes [100], [010], [001] respectively; $\circlearrowleft$ superscript refer to whether the tilting is in-phase (+) or anti-phase (-) along certain axis, or absent (0); $a^+a^+b^-$ means two equal-amplitude in-phase tilts around [100] and [010], and an anti-phase tilt with a different amplitude around [001]

$a^-b^0c^0$			
$a^-b^+c^0$	$a^-b^-c^0$		
$a^-b^-c^-$	$a^-b^-c^+$	$a^-b^+c^-$	$a^-b^+c^+$
$a^+b^0c^0$			
$a^+b^+c^0$	$a^+b^-c^0$		
$a^+b^+c^+$	$a^+b^-c^+$	$a^+b^+c^-$	$a^+b^-c^-$

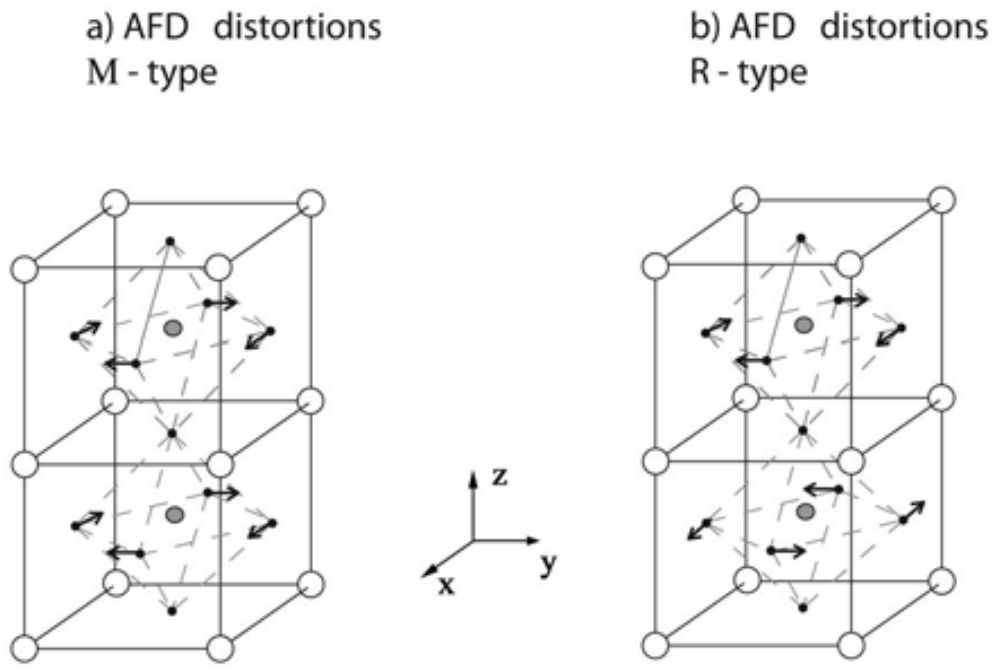

Figure 3.4: In this figure are sketched: a) in-phase rotation of O_6 octahedra ($a^0b^0c^+$); b) anti-phase rotation of the O_6 octahedra ($a^0b^0c^-$); along the [001] direction.

[1] Glazer have done a systematic study on octahedra tilting on perovskites, that later on was revised and enriched by Howard et al. for more details refer to [36, 45]

The relaxations were done for all the configurations in table (3.1) on which we superimpose combinations of FE and AFE distortions obtained by off-centering of Bi cations.

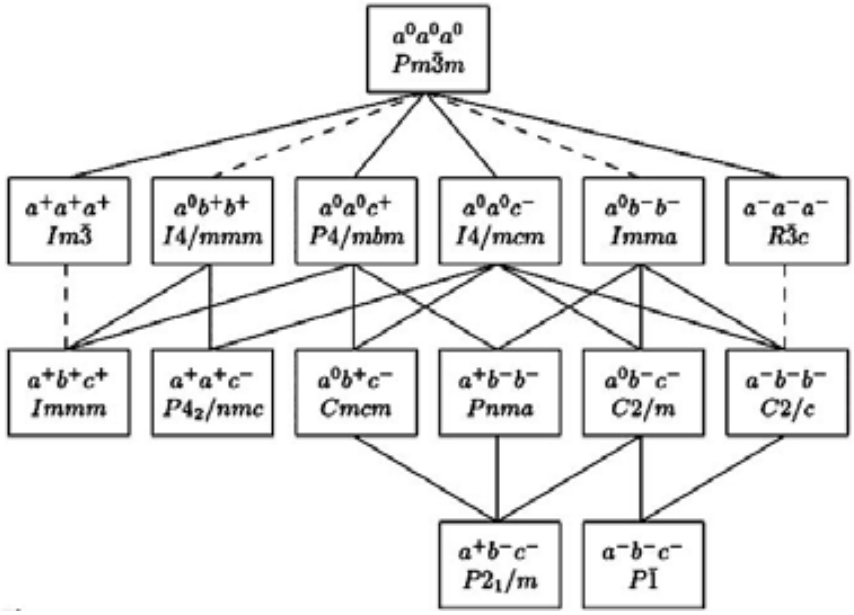

Figure 3.5: A schematic diagram recording the structures for perovskites found by Howard et al. (1998). The diagram shows the space-group symmetry, along with the Glazer (1972) symbol for the tilts. The lines indicate group-subgroup relationships, and a dashed line joining a group with its subgroup means that the corresponding phase transition is in Landau theory required to be first order. The figure has been reproduced from Howard et al. [Acta Cryst. (2002), B58, 565].

Furthermore we have studied different cells with cubic, tetragonal and orthorhombic shapes and different magnetic orders like the G- and C-antiferromagnetic spin arrangements. In total we have considered more than 300 starting configurations. For all these cases, we performed a short molecular dynamics simulation with random initial velocities (in order to break all the symmetries) and then a full structural relaxation. The lowest energy phases were confirmed as local minima by checking their stability against atomic and cell distortions.

For the structural search calculations, we employed the PBE+U functional, using essentially the calculations conditions discussed in section (1.2.2). As we will discuss later there are certain subtleties regarding the DFT functional chosen for the study. Here we will report the results obtained for three possible choices (LDA, PBE and PBEsol) and discuss which one seems to be more suitable.

3.2 Results and Dicussion

3.2.1 Lowest-energy phases found

As mentioned before more than 300 starting configurations were considered. From these, we obtained many local minima with energies within a range of 200 meV/f.u. above BFO s ground state. We list the most relevant phases found by our study in table (3.2), where we show the energies obtained by relaxing the relevant structures for different functionals (PBE+U, the one used for the explorations, as well as PBEsol+U and LDA+U).

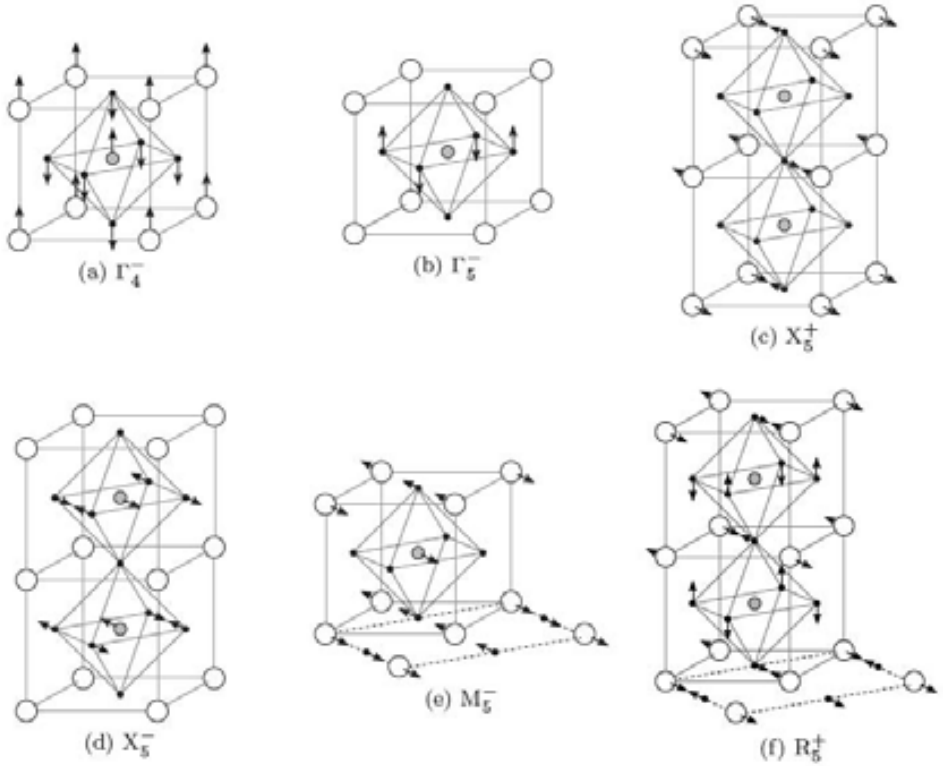

Figure 3.6: Illustration of atomic displacements for different symmetry modes that are relevant in our study of BFO: (a) soft FE mode; (b) (f) secondary modes mentioned in Table 3.2. Only displacement directions, not magnitudes, are indicated, white, gray, and black circles represent Bi, Fe, and O atoms, respectively.

We may appreciate from our results that the energy differences between phases depend strongly on the functional used for the calculations. For the different functionals, we observed changes in the relative stability of the local minima and even some did not capture some of the phases (this is the case of $Pna2_1$ which was found only with the PBE+U functional). These differences will be addressed in more detail later in this chapter.

Table 3.2: Energies and distortions of the most stable energy minima found (seven top phases), as well as a few saddle points (six bottom phases) included as reference. Columns 2 4 are the energies obtained with different DFT functionals. Note that the $Pna2_1 - G$ phase goes to $Pnma - G$ when relaxed with PBEsol+U and LDA+U. Columns 5 8 are the distortions from the ideal cubic perovskite structure ($Pm\bar{3}m$) that characterize the phases. In all cases the FE and AFD modes fully determine the symmetry breaking. A generic $[x, y, z]$ FE (AFD) distortion involves displacements (O_6 rotations) along (around) the x, y, and z Cartesian axes. We indicate the dominant FE and AFD distortions in bold. Column 8 includes other modes with a significant contribution (at least 10% of the largest one). The mode analysis was done with the ISODISPLACE software [14]; note that q-points indicated in symmetry labels constitute default choices and do not always correspond to the actual distortion modulation (e.g., the X_5^+ and X_5^- AFE modes in the table are actually modulated along the z direction).

	$\Delta E = E - E(R3c - G)$			Structural distortions			
Phases	PBE+U	PBEsol+U	LDA+U	Γ_4^-(FE)	R_4^+(AFD)	M_3^+ (AFD)	Aditional distortions
Pc-C	19	106	134	$[x, x, \mathbf{z}]$		$[0, 0, z]$	AFE(M_5^-), O_6-dist. (Γ_5^-), $c/a = 1.27$
Cm-C	12	103	132	$[0, y, \mathbf{z}]$		$[0, y, 0]$	O_6-dist. (Γ_5^-), $c/a = 1.27$
$Pna2_1$-C	14	99	127	$[0, 0, \mathbf{z}]$	$[x, x, 0]$	$[0, 0, z \sim 0]$	AFE (X_5^+, X_5^-, R_5^+,), $c/a = 1.26$
Cc-C	10	96	125	$[x, x, \mathbf{z}]$	$[x, x, z \sim 0]$		AFE(R_5^+), O_6-dist. (Γ_5^-), $c/a = 1.25$
Pnma-G	60	27	14		$[\mathbf{x}, \mathbf{x}, 0]$	$[0, 0, \mathbf{z}]$	AFE (X_5^+, R_5^+)
$Pna2_1$-G	47			$[0, 0, z]$	$[\mathbf{x}, \mathbf{x}, 0]$	$[0, 0, \mathbf{z}]$	AFE (X_5^+, X_5^-)
R3c-G	0	0	0	$[\mathbf{x}, \mathbf{x}, \mathbf{x}]$	$[\mathbf{x}, \mathbf{x}, \mathbf{x}]$		
P4mm-C	82	140	152	$[0, 0, \mathbf{z}]$			$c/a = 1.28$
R3m-G	136	169	191	$[\mathbf{x}, \mathbf{x}, \mathbf{x}]$			
*Amm*2-G	175	203	213	$[\mathbf{x}, \mathbf{x}, 0]$			
$R\bar{3}c$-G	272	230	209		$[\mathbf{x}, \mathbf{x}, \mathbf{x}]$		
*I*4/*mcm*-G	430	372	344		$[0, 0, \mathbf{z}]$		
$Pm\bar{3}m$-G	981	906	870				

Table 3.2 also includes a brief description of the distortions from the cubic structure (relevant distortion modes depicted in Fig. 3.6) that characterize each phase. The phases are labeled by their space group and a letter indicating the C- or G-AFM order . The computed polarizations are listed in table 3.3 as well as the lattice parameters corresponding to the 40-atom cell. The detailed structure of the local minima are presented in table 3.4 with the structures sketched in Fig. 3.7.

Our calculation revealed three phases that can be obtained with relatively small changes of the pseudo-cubic perovskite cell and which favor the G-AFM order, $R3c$-G, $Pnma$-G and $Pna2_1$-G.

- All the functionals correctly predicted the ferroelectric $R3c$ phase with G-AFM order as the ground state, with a polarization along the [111] cartesian direction and anti-phase O_6 rotations around the same axis ($a^-a^-a^-$).

- With regards to the $Pnma$ structure, it is paraelectric (PE) and characterized by a different O_6 rotation pattern ($a^-a^-c^+$), which involves anti-phase rotations around [110] and in-phase around [001]. This is a very common phase among perovskites (like for instance $LaFeO_3$, $LaCrO_3$,$GdScO_3$ or $DyMnO_3$). In the case of BFO s $Pnma$-G phase, it can be described as AFE, due to the Bi cations showing large anti-polar displacements in the (001) plane (characterized by the X_5^+ mode) with an amplitude of about 0.3 Å (such AFE distortion is also present in $LaFeO_3$, which we will discuss in chapter 4 where the La off-centering is about 0.2 Å).

- The $Pna2_1$-G phase is also orthorhombic with a very similar structure to $Pnma$-G, but including a FE distortion along the axis of the in-phase rotations. In comparison with the $Pnma$-G within the 40-atom cell, the $Pna2_1$-G exhibit an elongation along the polarization direction, typical of the coupling between strain and FE distortions in perovskite oxides.

These phases are strongly AFM; a strong AFM exchange between neighboring Fe ions is evidenced by the large energy difference between the ferromagnetic (FM) and the G-AFM configurations, of more than 200 meV/f.u., in agreement with the high Neel temperature observed in bulk BFO.

Besides the just mentioned phases, other phases involving a large tetragonal distortion of the cell (stretched along the z direction) were also obtained. These phases exhibiting a large c/a ratios ($c/a \geq 1.25$) will be refered in following as supertetragonal or T phases. Within these phases, the most favored magnetic order was the C-AFM (see Fig. 3.3) with a FM exchange interaction along the stretched direction. Along this direction the magnetic interactions are weaker, with an energy splitting about 5 meV/f.u. between the G- and C-AFM orders; a relatively lower ordering temperature is thus expected.

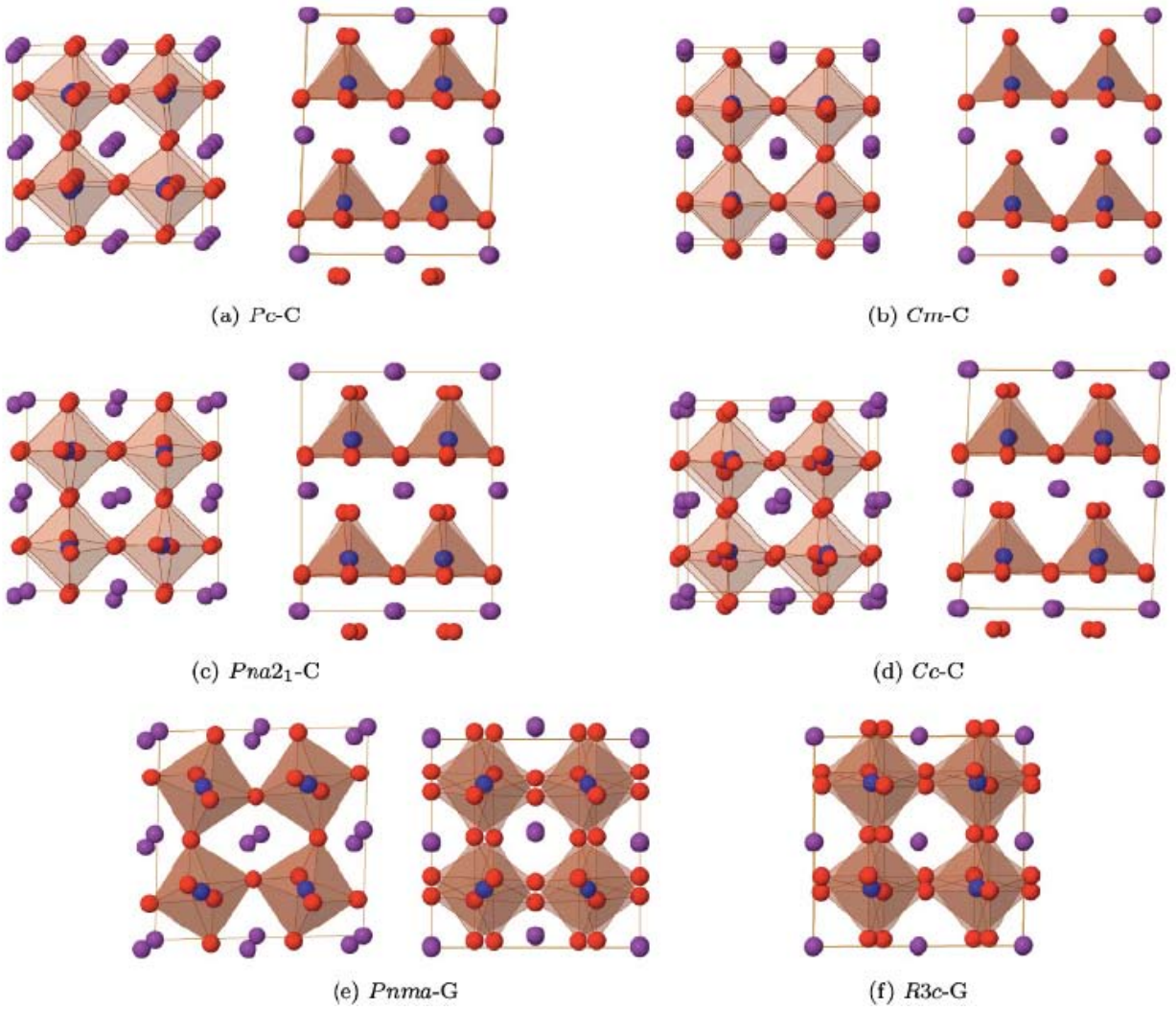

Figure 3.7: Sketch of phases obteined as energy minima: In the (a)(d) we show C-AFM supertetragonal phases; in the left (right) image the c axis is perpendicular (parallel) to the page. The (e) and (f) correspond to the G-AFM phases; two pseudocubic axes are equivalent in (e), with the left (right) figure having the nonequivalent axis perpendicular (parallel) to the page; the three pseudocubic axis are equivalent in (f). The atomic species can be identified as in Fig. 3.3

Table 3.3: Computed PBEsol+U lattice parameters (corresponding to the 40-atom cell of Fig. 3.3) and polarization values for the six stable phases of BFO listed in Table 3.2. The polarization direction is given in a Cartesian reference that corresponds almost exactly with the 40-atom cell vectors. For comparison, we also include the result for the $P4mm - C$ structure.

	Lattice parameters						Polarizations	
Phases	$a\,(\mathring{A})$	$b\,(\mathring{A})$	$c\,(\mathring{A})$	$\alpha\,(deg)$	$\beta\,(deg)$	$\gamma\,(deg)$	Magnitude C/m^2	Direction
Pc-C	7.500	7.500	9.489	88.1	88.1	89.7	1.20	$(0.29, 0.29, 0.92)$
Cm-C	7.380	7.608	9.533	86.6	90.0	90.0	1.50	$(0.00, 0.30, 0.95)$
$Pna2_1$-C	7.515	7.515	9.452	90.0	90.0	90.0	1.39	$(0.00, 0.00, 1.00)$
Cc-C	7.527	7.527	9.444	88.0	88.0	90.0	1.45	$(0.23, 0.23, 0.94)$
$Pnma$-G	7.830	7.830	7.770	90.0	90.0	87.6	0	
$R3c$-G	7.893	7.893	7.893	89.5	89.5	89.5	0.91	$(0.58, 0.58, 0.58)$
$P4mm$-C	7.414	7.414	9.526	90.0	90.0	90.0	1.52	$(0.00, 0.00, 1.00)$

Three of the T phases are monoclinic (Cc-C, Cm-C, and Pc-C) and one is orthorhombic ($Pna2_1$-C); all of them are ferroelectric with a very large polarization component along [001] direction (see the computed polarizations in table 3.3):

- In the case of the Cc-C phase, it presents a polarization in the $(1\bar{1}0)$ plane, as well as relatively small AFD distortions. This type of monoclinic phase is usually termed M_A; [86] a similar phase has been studied theoretically in connection with the supertetragonal structures observed experimentally in BFO films. [7, 39, 90, 94]
- The Pc-C phase is very similar to the Cc-C with respect to polar distortions (it M_A as well), but it has a different pattern of O_6 rotations.
- The Cm-C phase has a polarization in the (100) plane and a very distorted cell in the xy plane (monoclinic M_C in the notation of [86]).
- The $Pna2_1$-C phase is very similar to the $Pna2_1$-G structure discussed above, the stretching of the cell and development of polarization coinciding with the axis of the in-phase rotations.

Our results reveal a complex energy landscape, specially around the supertetragonal structures. For instance, in the case of the Cm-C phase it can be obtained as a Pm-C structure distorted by the $M_3^+\,[0, y, 0]$ mode listed in table 3.2. When going from Pm-C saddle point to the Cm-C minimum, the system lower its energy by about 1 meV/f.u. of energy. Similarly, the reported Pc-C phase is connected with a higher-symmetry Cm-C structure via a $M_3^+\,[0, 0, z]$ distortion. With such a complex energy landscape, we propose the structures in table 3.2 as a probably incomplete list of the rich phase diagram that this compound can present.

It is important to mention that we have explicitly checked that the above phases are local minima of the energy. We find this result very interesting, as some of them (e.g., the pairs formed by $Pnma$-G and $Pna2_1$-G, or Cc-C and Pc-C) are very similar structurally. Furthermore we want to stress the presence of monoclinic phases with such small primitive cells being energy minima in the absence of any stabilizing, electric field or stress. This is interesting because as long as we know, monoclinic phases in bulk perovskite oxides tend to be associated with complex solid solutions or large unit cells.

Table 3.4: Energy minima structures of table 3.2 as obtained from PBEsol+U calculations. In the case of the $Pna2_1 - G$ phase, the PBE+U result is given (see text).

Pc-C		$a = 7.291$ Å	$b = 5,291$ Å	$c = 5.315$ Å
(unique axis b)			$\alpha = \gamma = 90^o$	$\beta = 139.46^o$
Atom	$Wyck.$	x	y	z
Bi	2a	0.8692	0.2649	0.4158
Fe	2a	0.4372	0.2467	0.4361
O	2a	0.0471	0.7150	0.5161
O	2a	0.5781	0.5084	0.3342
O	2a	0.5609	0.0152	0.2979
Cm-C		$a = 9.534$ Å	$b = 7.380$ Å	$c = 3.804$ Å
(unique axis b)			$\alpha = \gamma = 90^o$	$\beta = 86.60^o$
Atom	$Wyck.$	x	y	z
Bi	2a	0.4948	0	0.9617
Bi	2a	0.9959	0	0.9418
Fe	2a	0.2810	0.2482	0.5184
O	2a	0.3590	0	0.5151
O	2a	0.8446	0	0.5261
O	4b	0.0864	0.2388	0.5689
O	4b	0.3449	0.2443	0.0153
$Pna2_1$-C		$a = 5.314$ Å	$b = 5.314$ Å	$c = 9.452$ Å
			$\alpha = \beta = \gamma = 90^o$	
Atom	$Wyck.$	x	y	z
Bi	4a	0.5451	0.4799	0.4590
Fe	4a	0.0195	0.5127	0.2448
O	4a	0.0357	0.5476	0.0493
O	4a	0.2669	0.7524	0.3170
O	4a	0.2633	0.2491	0.3058

Continued on next page

Table 3.4 – continued from previous page

Cc-C (unique axis b)		$a = 10.604$ Å	$b = 5.322$ Å, $\alpha = \gamma = 90^o$	$c = 5.323$ Å, $\beta = 62.80^o$
Atom	$Wyck.$	x	y	z
Bi	4a	0.4829	0.7707	0.1102
Fe	4a	0.2689	0.2630	0.2799
O	4a	0.0727	0.2986	0.4448
O	4a	0.3290	0.9986	0.4671
O	4a	0.3405	0.5032	0.4593
$Pnma$-G		$a = 5.650$ Å	$b = 7.770$ Å, $\alpha = \beta = \gamma = 90^o$	$c = 5.421$ Å
Atom	$Wyck.$	x	y	z
Bi	4c	0.0523	1/4	0.0100
Fe	4b	0	0	1/2
O	4a	0.9722	1/4	0.5946
O	8d	0.2998	0.0461	0.3037
$R3c$-G		$\alpha = \beta = 90^o$	$a = b = 5.559$ Å, $\gamma = 120^o$	$c = 13.782$ Å
Atom	$Wyck.$	x	y	z
Bi	6a	0	0	0
Fe	6a	0	0	0.7236
O	18b	0.3156	0.2294	0.1238
$Pna2_1$-G PBE+U		$a = 5.702$ Å	$b = 5.507$ Å, $\alpha = \beta = \gamma = 90^o$	$c = 8.036$ Å
Atom	$Wyck.$	x	y	z
Bi	4a	0.4435	0.0016	0.2194
Fe	4a	0.5015	0.5007	0.4943
O	4a	0.2137	0.7074	0.0519
O	4a	0.1848	0.6876	0.4796
O	4a	0.5302	0.4171	0.2532

3.2.2 Energy differences between phases

The results obtained for the energy differences between phases have a disturbingly dependence on the DFT functional. We can appreciate from table 3.2 that the relative stability of phases changes dramatically from one functional to another. For example we can see that $Pnma$-G is more stable than the T phases according to PBEsol+U and LDA+U, but less stable according to PBE+U. The differences can be so strong that we can appreciate even the loss of stability of one phase: $Pna2_1$-G is stable for PBE+U, but the relaxation of this structure with PBEsol+U and LDA+U leads to the $Pnma$-G structure. With such strong variations

in the results depending on the choice of functionals, we questioned ourseves which of the above mentioned functionals gives the right relative stability. We acknowledge the accuracy of PBEsol regarding the structural description of individual phases [69] but, does that apply also to relative stability among different phases?

Ideally one would resort to a higher level first-principles theory (i.e. Quantum Monte Carlo) to solve this question; however, such calculations are well beyond the scope of this work. Resorting to simpler schemes like the so-called hybrid functionals, which are generally considered to be more accurate than the functionals here employed, is not justified as they are not well tested for quantifying relative stabilities in cases like this one[2]. Moreover, structural predictions with hybrids have been shown to depend strongly on the underlying generalized gradient approximation, [10] which invalidates them for the present purposes.

Nevertheless we were able to make a significant comparison with experiment for the transition between the $R3c$-G and $Pnma$-G phases by studying the transition driven by hydrostatic pressure. It is known [40] that at room temperature under hydrostatic pressure the $R3c - G$ phase at 3.5 GPa transforms into a monoclinic $C2/m$ structure with a large cell (made of 12 formula units), and that a second transition at 10 GPa leads to the $Pnma$-G phase as shown by Haumont et al. [40]. These results suggest that the crossover in retalive stability between the $R3c$-G and the $Pnma$ occurs in the range of pressure 3.5 10 GPa. If this region is extrapolated to $T = 0$ K (temperature at which our simulations takes place), we find the $R3c$-G and $Pnma$-G phases invert their relative stability at a pressure between 5 and 14 GPa. We studied this transition between the $R3c$-G and $Pnma$-G phases under hydrostatic pressure[3]. We obtained (see Fig. 3.8) transition pressures of about 2 GPa for LDA+U, 3 GPa for PBEsol+U, and 5 GPa for PBE+U. From these results, the PBE+U seems the most accurate describing the relative stabilities of the phases, and the LDA+U should be avoided for this purposes.

Similarly, we can compare with experiment our predictions for the $R3c$-G to supertetragonal transition induced by epitaxial strain. We computed the relative stabilities of these phases as function of the epitaxial strain corresponding to a square substrate in the (001) plane, to determine the lattice mismatch needed to stabilize the large-(c/a) structures. We constrained the 40 atoms cell to remain square in the plane (001) and performed structural relaxations of the remaining degrees of freedom for the range of strains shown in Fig. 3.9. We can appreciate from Fig. 3.9, where the obtained strain values for the transitions were of -2.3%, -4.0%, and -4.5% for PBE+U, PBEsol+U, and LDA+U, respectively. Experiments have shown that a BFO-(001) thin film grown on SrTiO3 (about -1.5% misfit strain) exhibit a monoclinic structure that is an epitaxially distorted version of the $R3c$ phase, which we will call from now on R phase (this phase is believed to be monoclinic M_A with the Cc space group [18]). However, when grown on $LaAlO_3$ substrates (about -4.8% misfit strain), a supertetragonal T phase whose symmetry remains unclear, [7] or a coexistence of the R and T phases, [94] has been observed. These experiments, thus, suggest a phase change around epitaxial strains of -4.8%. Comparing with our results and assuming the supertetragonal phases obtained by us are good

[2]Such comparison was employed in section 1.2.2 for the determination of the most appropriate U value for describing the d-electrons. Where we compared two different magnetic orders within the same structure.

[3]Details on how the simulation of phase transitions under hydrostatic pressure are done, will be given in chapter 5

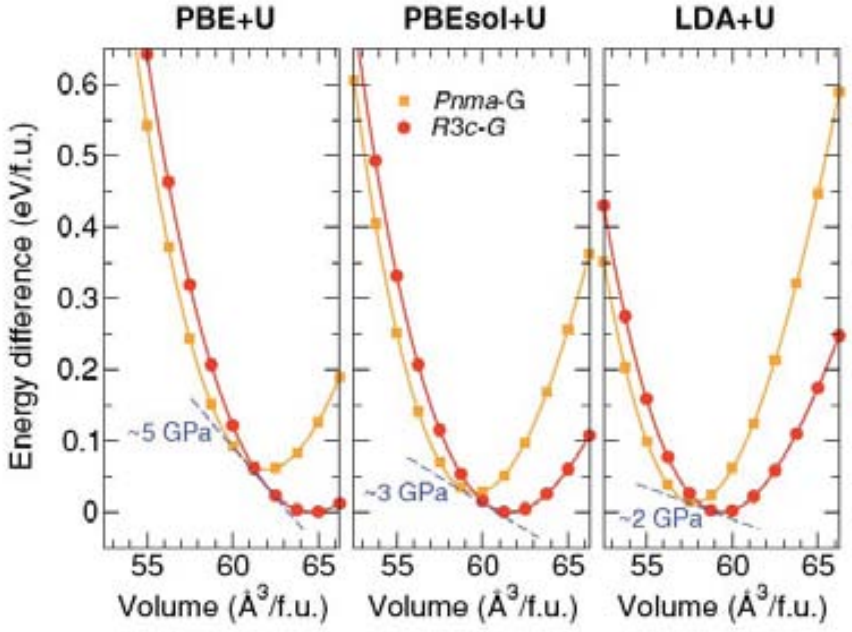

Figure 3.8: Energy versus volume curves for the most stable phases of BFO. The labels at the top indicate the DFT functional used. The transition pressures mentioned in the text were obtained by computing the slope of the common tangent of the $R3c$-G and $Pnma$-G curves which is obtained from the condition $E_{R3c} - P_c V_{R3c} = E_{Pnma} - P_c V_{Pnma}$.

candidates to represent the experimentally realized T phase, it seems that the PBE+U curve is the least reliable, with the LDA +U giving the more accurate description of the transition. This result that is not surprising, if we recall the known failure of the PBE approximations, which tend to render too large tetragonal distortions in ferroelectric perovskites. [10, 92]

Thus, the PBE+U and LDA+U approximations seem to work for one case but fail for the other. However, PBEsol+U appears as a reasonable compromise, describing with an acceptable degree of accuracy both situations. We thus, chose PBEsol+U as the most accurate DFT theory available to us. At any rate, noting that PBE+U performance is very good as regards the relative stability of the $R3c$-G and $Pnma$-G phases, we believe that the PBE+U prediction of the new ferroelectric phase $Pna2_1$-G deserves to be taken into account.

3.3 Discussion of results

The results here presented have direct implications for the theoretical models describing BFO s structural phase transitions as well as for current experimental works, specially regarding the epitaxially compressed films in which supertetragonal phases were discovered. In the following we will discuss the conclusions that can be drawn from these results.

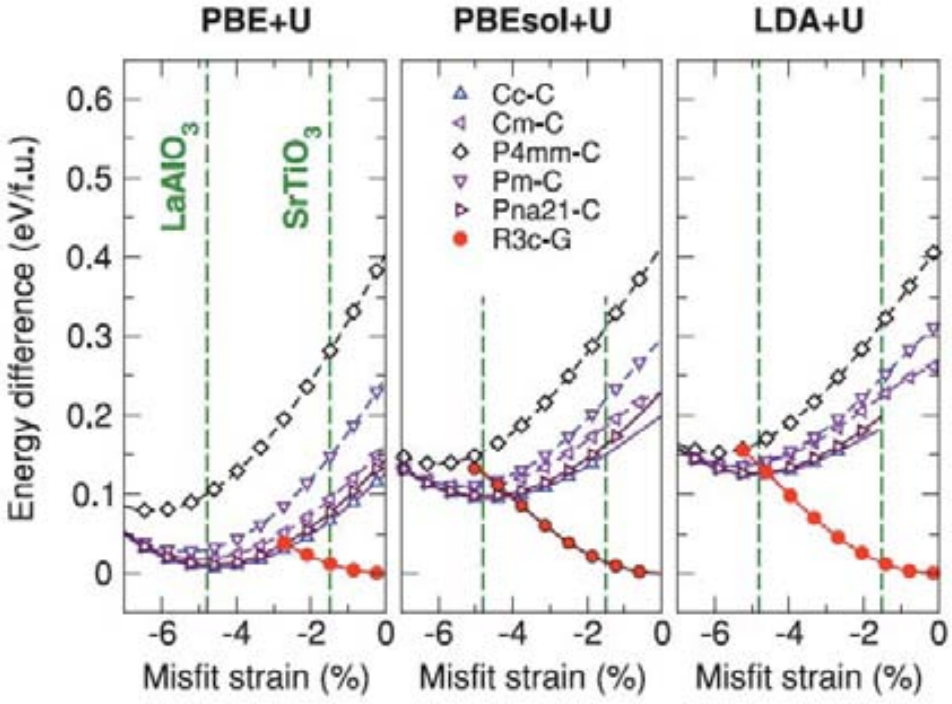

Figure 3.9: Energy of various BFO phases as a function of the misfit (epitaxial) strain corresponding to a square (001)-oriented substrate. The labels at the top indicate the DFT functional used. Note that the $R3c$-G phase reduces its symmetry to Cc-G in these epitaxial conditions.

3.3.1 Implications for experimental work

Novel phases obtained in thin films

Recent experimental works in BFO thin films by Béa et al. [7] and Zeches et al. [94] have shown that a novel phase of BFO is obtained when thin films are grown on strongly compressive substrates like $LaAlO_3$. This phase is characterized by a large $c/a \sim 1.23$ ratio and an out of plane polarization of $P_z \sim 0.8$ C/m^2. A number of first principles studies [39, 90, 94] have identified this phase with a monoclinic Cc structure from LDA+U calculations. The predicted phase has the same c/a ratio but exhibits a polarization of $P_z = 1.5$ C/m^2, resulting in a large quantitative disagreement with the experimental result.

In comparison, we have obtained several phases displaying large c/a ratios (see table 3.2) that are minima for the epitaxial strain corresponding to $LaAlO_3$ substrate. These phases are very close in energies, with differences below the 10 meV/f.u. (see Fig. 3.9). Therefore not only the $Cc-C$ phase, but also the Pc-C, Cm-C, and $Pna2_1$-C phases are energetically accessible for the mentioned experimental conditions.

Because our T phases are an almost perfect epitaxial match with the $LaAlO_3$ substrate, the structural and polarization data in tables 3.3 and 3.4 can be directly compared with the experimental results. Let us note that the T phases obtained from our calculations present a significant difference in values of polarizations. While the Pc-C phase (with a $c/a = 1.27$) presents $P_z \sim 1.1$ C/m^2, the $Cm-C$ and $Pna2_1$-C phases (with c/a of 1.26 and 1.25, respec-

tively) present $P_z \sim 1.4$ C/m^2. A result that suggests the $Pc-C$ phase as the best candidate to represent the T phase observed experimentally (disagreements between the experiment and theory would be below the 40% instead of the 90% of the previously proposed phase).

However, we want to stress that, because our T phases are so close in energy, predicting which one is realized experimentally is not a simple task, and may depend on subtle details not considered in our simulations. For instance, two of these phases (Pc-C and Cm-C) present no tilts (i.e., no rotations around the [100] and [010] axes) of the O_6 octahedra, which may make them preferable if the BFO films are grown on (001) substrates that clamp such distortions strongly. If a rectangular substrate is used, the Cm-C might be favored, with a distorted cell in the xy plane, etc.

Transitions in bulk $BiFeO_3$

From the results presented here, we want to make some comments on the structural phase transitions in bulk BFO. Even though our calculations were done at the limit of low temperatures[4], a few comments can be made on the basis of the large energy differences between some of relevant phases. Our results support experiments [**?**,15,65] showing that BFO s ferroelectric $R3c$ phase transforms into an orthorhombic $Pnma$ structure at $T \sim 1100$ K, with the cubic $Pm\bar{3}m$ phase appearing at temperatures over the 1200 K. Looking at the energy differences of table 3.2, more specifically at those corresponding to the PBEsol + U calculations, we may appreciate that the $R3c$-G and $Pnma$-G minima are very close in energy and constitute strong instabilities of the prototype $Pm\bar{3}m$ structure, which lies about 900 meV/f.u. above them. This results are consistent with the observation that BFO s cubic phase can exist only at very high temperatures. Our results also rule out the possibility of the transition sequence $R3c \rightarrow I4/mcm \rightarrow Pm\bar{3}m$ obtained by Kornev et al. [56] from Monte Carlo simulations with effective Hamiltonians derived from first principles calculations. We find the $I4/mcm$ relatively higher in energy; thus, it is unlikely for this phase to occur instead of $Pnma$.

As for the pressure driven transitions, our results support the experimental observation of the $R3c$ to $Pnma$ transition with increasing hydrostatic pressure. Moreover the PBE+U predicted the phase $Pna2_1$-G to be favored under compression, nearly becoming the ground state in the pressures range in which the $R3c-G$ and $Pnma$-G phases revert their relative stability.

3.3.2 Other observations

Phenomenological theories

Now we will briefly discuss the connection of our results with phenomenological models like the Landau-Devonshire theory. It is known that such theories provides a successful description of many FE perovskites such as $BaTiO_3$. [20,22,48] Actually we may think of the Landau models as the simplest and most powerful approach that could be used to model BFO s phase

[4]For a proper description of finite temperature effects a full statistical calculations are required, as the relative stability of phases may depend on effects such as, vibrational entropy and thermal expansion, plus the fact that the transition temperatures may depend strongly on the competing instabilities (see for instance the work by Zhong and Vanderbilt [96]).

diagram and properties. However, constructing the Landau potential for BFO, and determining the temperature dependence of the parameters, is task of great complexity which as far as we know have not been accomplished yet. Our results have direct implications regarding the order of the expansion in such a Landau potential.

If we try to describe the phases of this material, including the ones obtained in this study, the Landau potential has to be written in terms of the primary order parameters: a FE order parameter associated with the three dimensional polarization vector **P**, and two AFD order parameters describing the in-phase and anti-phase O_6 octahedra rotations. We need also to include in the expression the cross terms between the three order parameters, plus an additional term describing the epitaxial strain if considered. With all this ingredients it should be possible to derive the complex energy landscape of BFO with the corresponding minima. From our findings, we can say that this Landau theory should include high-order terms in the expansion. In a seminal paper by Vanderbilt and Cohen [86], they have analyzed the order of the Landau potential needed to describe low symmetry phases in FE perovskites. They have showed that a Landau potential $\mathcal{F}(P)$ expanded up to 4th order in P can only present rhombohedral and tetragonal minima, for the inclusion of orthorhombic minima the expansion needs to be up to 6th order, and to capture the monoclinic minima up to 8th. From our results we observe the coexistence of two monoclinic different types of minima (M_A and M_C), in order to describe such behavior we need a theory of 10-th or 12-th order in the polarization. Such a level of complexity is unheard of, especially among simple ABO_3 compounds.

The role of bismuth

Let us discuss now the importance of the Bications in BFO s structural phase transitions. With the electronic configuration ($6s^2 6p^0$), Bi is known to form very anisotropic bonding which results in the presence of lone pairs at the nonbonding side. This effect is responsible for the Bi off-centering in BFO ground state $R3c$-G, and for the high polarization observed in this material. We computed the electron localization function (ELF) to analyze the characteristics of Bi s electronic structure and how it varies with the structural changes. The results are shown in Fig. 3.10, where we may appreciate the occurrence of the lone pairs for the ground state $R3c$-G and supertetragonal Cc-C structures, along with a very anisotropic bonding. So far this is what we expected considering the large Bi off centering and large polarization of these phases. However if we focus on results for the orthorhombic $Pnma$-G phase, clear differences arise, as in that case we do not observe any signature of the lone pair in the ELF..

We have thus observed how Bi exhibits an ability to form different coordination complexes with the neighboring oxygens. These chemical effects appear as the driving force for the structural richness of BFO. Thus, the relative stability between BFO s low energy phases is probably determined by subtle competitions between different Bi-O bonding mechanism.

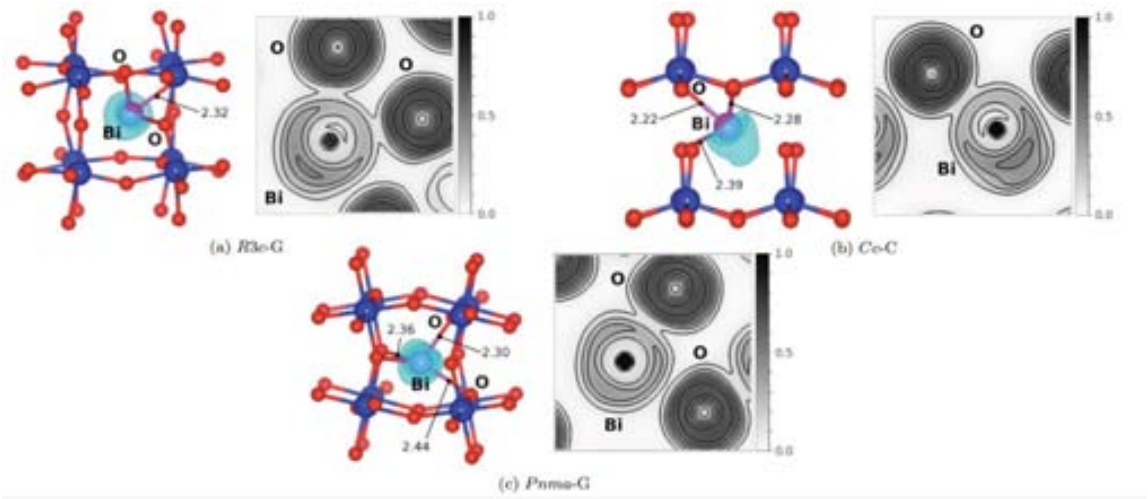

Figure 3.10: Electronic-localization-function (ELF) maps computed for the $R3c$-G, Cc-C, and $Pnma$-G phases. The figures on the left show the isosurface for an ELF value of 0.3 superimposed onto the atomic structure. (a) We can appreciate the anisotropic charge distribution for the $R3c$-G phase, it can be seen the nonbonding localization domain on the opposite side of Bi bonding to the three neighboring O atoms, which is the signature of a lone pair; (b) we found lone pair forms in the supertetragonal Cc-C phase, as might have been expected from Bis large off-centering and the anisotropic spatial distribution of its neighboring oxygens; (c) for the $Pnma$-G phase, the Bi cations have four neighboring oxygens that form a rather regular BiO_4 tetrahedron (the corresponding ELF plots show a very isotropic localization domain around Bi).

3.4 Summary

In this chapter we have presented the results of our first principles search for potentially stable phases of the multiferroic $BiFeO_3$. We performed a systematic study of most relevant distortions that are common to perovskite oxides (more specifically, ferroelectric, antiferroelectric, and anti-ferrodistortive). We obtained plenty of distinct low-energy phases of the compound and restricted our discussion to the most stable ones. We found that some of the minima presented here display complex structural distortions which lower the symmetry to M_A and M_C monoclinic space groups preserving a relatively small unit cell. This was a very peculiar finding because, as far as we know the monoclinic structures reported in perovskite oxides are usually associated to solid solutions [e.g. $PbZr_{1-x}Ti_xO_3$ (M_A type) [64] and $PbZn_{1/3}Nb_{2/3}O_3 - PbTiO_3$]; occur in thin films under epitaxial strain, or present relatively large unit cells.

From these results, a number of important implications for current research on BFO were discussed:

- First of all we have found that BFO can form plenty of stable and metastable structural phases. This is consistent with recent experimental observations that show, a wide range of possible structural transitions at low temperatures, [73] surface-specific atomic structures [60] and strain-induced new phases. [40, 94] Also, our results can be useful for the experimental works exploring the possibility of obtaining large functional effects

(piezoelectric, magnetoelectric) in BFO s films grown on strongly compressive substrates. We have shown that there are plenty of phases with large polarizations and c/a aspect ratios that can be realized in such conditions; the transitions (e.g., driven by temperature or electric fields) between such phases could give raise to useful effects.

- Our results also have implications for theoretical studies of BFO. We carried out a careful comparison of the various DFT schemes most commonly employed to study BFO and related compounds, and discussed the existing difficulties in quantifying the relative phase stability. Further, we considered the implications of our findings as regards the effective modeling of structural phase transitions in BFO. Our analysis shows that BFO is rather unusual, and requires very high-order Landau potentials to capture the diversity of structural phases that it presents. A result that is revealing the unexpected complexity of this material in comparison with the theories devised for materials such as $BaTiO_3$ or $PbZr_{1-x}Ti_xO_3$.

- Finally, we have shown quantitative evidence of the dominant role of Bi in BFO s structural instabilities. We have computed the ELF and observed how in some of the phases, the lone pair mechanism usually assumed to accompany the Bi O bonding, is absent. Instead, for the FE phases displaying strong Bi off centering, such a mechanism is present along with a large polarization. Thus, Bi s ability to form diverse and competitive in energy coordination complexes with oxygen, appears as one the reasons for the richness of structural phases presenting this material.

With this we have quantified, and analyzed in some detail the structural richness of $BiFeO_3$, the most relevant representative of the family of Bi-based transition-metal perovskite oxides. We have thus revealed a variety of unusual effects with important implications for current experimental and theoretical works on this material.

Chapter 4

$Bi_{1-x}La_xFeO_3$ Solid Solutions

As discussed before one of the proposed strategies to enhance the magnetoelectric response of bismuth ferrite ($BiFeO_3$ or BFO) is by means of a solid solution $Bi_{1-x}Re_xFeO_3$. In the present chapter we want study how this can be achieved with the $Bi_{1-x}La_xFeO_3$ (BLFO) solid solution.

Among the multiferroics, BFO is the best studied compound. [15] Bulk BFO presents magnetoelectric (ME) multiferroic order at room temperature (T_r) with magnetic and ferroelectric ordering temperatures $T_N = 643$ K and $T_C \approx 1100$ K respectively, [15] which places this material as prospective candidate for technological applications. However, one of the current challenges is to enhance the ME coupling, particularly the linear effect. The linear ME effect is accounted by the tensor α, which was introduced in see section 2.1.3.

This coupling is not allowed by symmetry in bulk BFO, due to the presence of an incommensurate cycloid-like modulation of BFO s antiferromagenic (AFM) spin structure. The existence of such spin cycloid cancels out any linear ME coupling between **P** and **M**. However, if the spin cycloid is destroyed, something that has been proposed to occur by applying an epitaxial strain or by partial chemical substitution of the cations [6, 72], the experiments and first-principles simulations suggest that BFO s linear ME coupling is still relatively weak. [89, 97]

4.1 Expected enhancement of the magnetoelectric response in $Bi_{1-x}La_xFeO_3$

With respect to the strategies to enhance BFO s linear ME response, previous theoretical works have shown that by replacing the magnetic cation with other magnetic species (which might have stronger spin-orbit interactions) the obtained results are not very promising. [89]. These calculations showed that the response to an electric field $\mathcal{E}$ in this material is dominated by the deformation of the Bi O bonds. In the cases studied (with the transition metal atoms Co, Cr, and Mn, as well as double perovskites including Fe-Cr and Mn-Ni), such response remains relatively independent of the magnetic species. Further, it was found that the magnetic response to the $\mathcal{E}$ is an indirect effect that is dominated by the Bi s structural distortions.

Our strategy here is to enhance the response via the softening of the lattice. As explained in section (2.3.3), this strategy is designed to enhance the normal response. The system is

brought close to a phase transition (preferably of second order) where the lattice deformations are stronger in the presence of an applied field. Such a structural softness would result in an enhancement of the lattice-mediated ME effect, [46] which we have shown (see section 2.1.3) to essentially follow the behavior of the dielectric response of the material. [89]. For our purpose this softening will be induced by chemical doping of BFO with $LaFeO_3$ (LFO).

The BFO solid solutions appear as the best suited candidates for such response enhancement. Recent works have shown how the ME response of the material at T_r can be increased by more than one order of magnitude in the $(BiFeO_3)_{1-x}$ $(CaTiO_3)_x$ solid solution. [53]. In this work ,the authors attribute the enhancement mechanism to the structural softness, and thus to the lattice-mediated response. Other interesting results are those by Kan et al., who have shown that an enhanced dielectric response can be achieved in $Bi_{1-x}Re_xFeO_3$ solid solutions with Re = Sm, Gd, Dy, etc. [52] Also these authors claim to have observed a seemingly universal phase diagram, with the particularity that, at intermediate compositions, the solutions exhibit an anomalous response to applied electric fields that has been associated with an $\mathcal{E}$-induced paraelectric (PE) to FE transition.

The $Bi_{1-x}La_xFeO_3$ (BLFO) solid solutions have traditionally attracted interest from experimentalists. It has been shown that the spin cycloid characterizing bulk BFO disappears upon doping with La. Besides, the doping of BFO (a FE compound) with the LFO (a PE material) is expected to result in a morphotropic phase transition, which should carry with it an enhancement of the dielectric response and the ME coupling α. Also, in the context of the previous mentioned results on $Bi_{1-x}Re_xFeO_3$ compounds, BLFO appears as the ideal model system to investigate from first-principles the physics of these compounds, as it seems to present the same sort of phase diagram and allows for simulations that do not suffer from the potential complications associated with the treatment of rare-earth elements (i.e., f electrons).

In this chapter we will present our results for the simulations of BLFO. Our results suggest that an enhancement of the functional responses occurs for compositions close to both the BFO and LFO limits. Our calculations reveal the atomistic mechanisms responsible for the improved properties. Furthermore we observe the possibility of $\mathcal{E}$-induced PE-to-FE and FE-to-FE transitions, due to the presence of several (meta)stable phases that are quasi-degenerate in energy in a wide range of intermediate compositions.

4.2 Our Computational Approach

We followed the criteria described in section (1.2.2) for the election of the functional and the calculation conditions. We thus chose the Generalized Gradient Approximation to Density Functional Theory (more precisely, the so-called PBE scheme proposed by Perdew et al. [67]), as implemented in the VASP package. [57, 58] As shown previously in chapter 3, the choice of functional has a significant effect on the relative stability of the phases here investigated, and the PBE scheme seems to be the best option to treat the rhombohedral and orthorhombic structures that are relevant for BLFO. A Hubbard-U following Dudarev s scheme [23] with $U = 4\,eV$ was used for a better treatment of irons $3d$ electrons [1].

[1] the value for the U was done carefully, according to the criteria explained in the subsection 1.2.2

We used the projector augmented wave method to compute the electronic wave functions (discussed in subsection 1.2.1), solving explicitly for the following electrons: Fe s $3p$, $3d$, and $4s$; Bi s $5d$, $6s$, and $6p$; La s $5s$, $5p$, $5d$, and $6s$; and O s $2s$ and $2p$. The wave functions were expanded in a plane wave basis set truncated at 500 eV, and a $3 \times 3 \times 3$ Γ-centered k-point grid was used for integrations within the Brillouin zone (BZ) corresponding to the 40-atom cell of Fig 4.1.

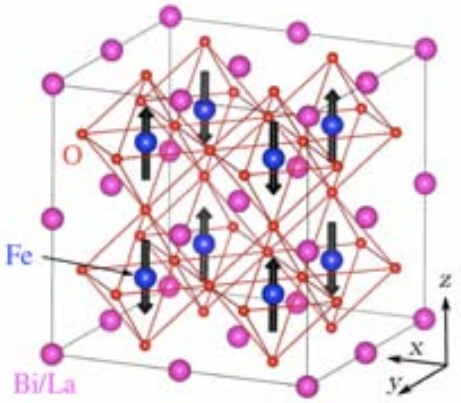

Figure 4.1: Supercell used in our simulations. The arrows on the Fe ions indicate the G-AFM spin arrangement that characterizes BLFO.

As mentioned before, we worked with the 40-atom cell depicted in Fig.4.1. This cell is compatible with the experimentally observed atomic structures of BFO (rhombohedral $R3c$ space group and 10-atom primitive cell; see Fig.4.2 and denoted R phase in the following) and LFO (orthorhombic Pnma space group and 20-atom cell; see Fig.4.3 and denoted $O1$ phase in the following). It is also compatible with the G-AFM spin arrangement that is common to both phases, see Fig.4.1.

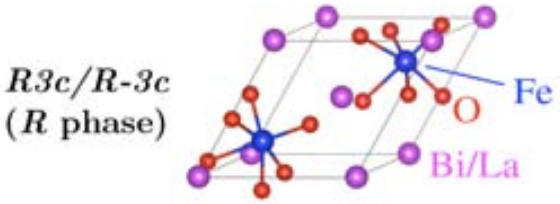

Figure 4.2: $R3c$ phase that is the ground state of pure BFO. In essence, this structure reduces to $R\bar{3}c$ when the Bi/La and Fe cations locate at the centrosymmetric positions in the middle of their first-neighboring oxygen shells.

Within this 40-atom cell, we were able study the structural distortions that are usually present in the low symmetry phases of most perovskite oxides (as mentioned in the previous chapter

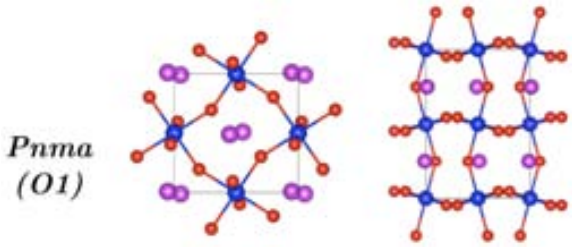

Figure 4.3: *Pnma* structure that is the ground state of pure LFO.

3). For this reason we expect our simulations to be able to capture the composition-dependent structural transitions of BLFO in a realistic way. However, recent experiments suggest that BLFOs intermediate phases, may have a more complex structures that are not compatible with our chosen cell. [85] This issue will be discussed in more detail later in this chapter, along with the connection of our results with the experiments.

We applied a systematic search for possible phases that may be relevant for this material (following the same procedure that was mentioned in the previous chapter3). For the structural search we considered the compounds at the limits for $x = 0$ (BFO) and $x = 1$ (LFO), and the $x = 1/2$ composition with a rocksalt arrangement of the Bi/La cations. For the relevant phases identified, we studied all the compositions available within the 40-atom cell (steps of La composition of $\Delta x = 1/8$).

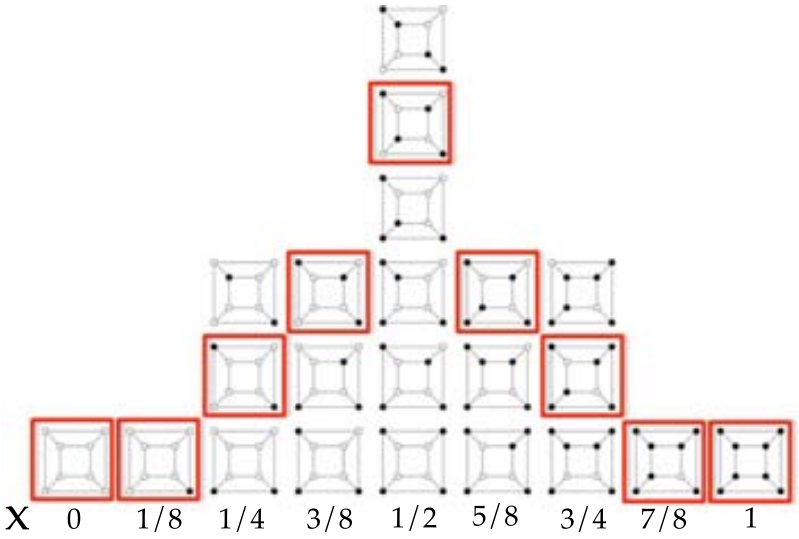

Figure 4.4: *R*3*c* related inequivalent Bi/La arrangements, we have represented only the 8 A-site present in the 40-atom pseudocubic cell where the Bi/La cations substitution takes place. This 8-sites form a cube that is showed in a stereographic representation in the figure, indicating with a black dot the dopant (La) position.

At intermediate values of x the effect of the substitutional disorder was studied by simulating explicitly all inequivalent Bi/La arrangements (see Fig. 4.4). For all the BLFO configurations investigated, the atomic structure was fully relaxed until residual forces and stresses become

smaller than 0.01 eV/Å and about 1 kB, respectively. Selected cases were further considered for the computation of their electric polarization and electromechanical response properties, following the standard methods. [91].

4.3 Phase diagram and basic properties

The BLFO solid solution has been the studied experimentally previously by many authors. [30,84,85,93] However there are many discrepancies and contradictory results about the structures involved in its phase diagram. With this we faced our first problem in the simulation of this compound. Thus, we started our study assuming no prior knowledge and performing the exhaustive search mentioned above.

We were able to identify up to three phases that we consider relevant for understanding the phase diagram of BLFO: the respective ground state phases for both pure compounds $R3c$ for BFO (Fig.4.2) and $Pnma$ for LFO (Fig.4.3), plus an structure that is ferroelectric and presents the $Pna2_1$ space group (see Fig.4.5). This third phase, which we will denote by $O2$ in the following, is very similar to LFO s orthorhombic groundstate, having the same unit cell and O_6 rotation pattern (conformed by anti-phase rotations around the $[110]_{pc}$ pseudocubic direction and in-phase rotations around $[001]_{pc}$, denoted by $a^-a^-c^+$ in Glazers notation [36]). Its main difference is the ferroelectric distortion along the $[001]_{pc}$ direction, that render a relatively high value of polarization (about $0.5\,C/m^2$ for the $O2$ structure with the BFO composition).

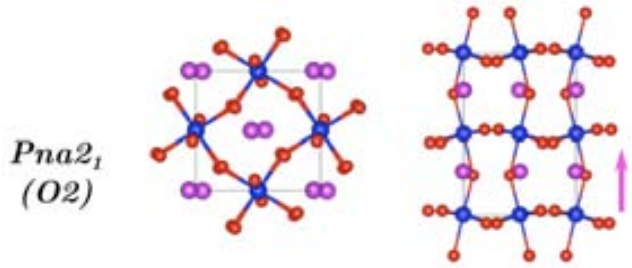

Figure 4.5: $Pna2_1$ structure; the arrow indicates the direction along which a polarization appears driven by the displacement of the Bi/La sublattice.

We may appreciate the richness and complexity of structural features that this system may have in Figure 4.6. From our relaxations for the phases studied, for each different composition, we have obtained many different configurations. Some of them with very low symmetry, and exhibiting exotic structures like those with complex tilts (a combination of in-phase and anti-phase tilts along certain direction. We observed that these complex rotations patterns involving in-phase and anti-phase tilting tend to appear in Bi/La arrangements that are relatively high in energy. As a general rule we find that the system prefers Bi/La arrangements that respect the rocksalt order.

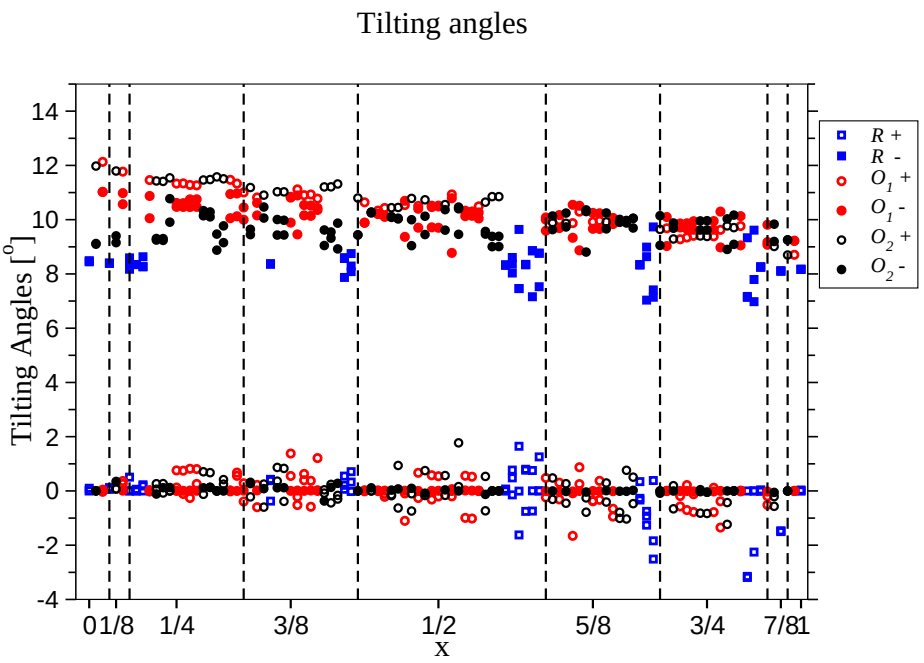

Figure 4.6: Tilting amplitudes for all phases and Bi/La arrangements (with a + we mean an in-phase tilt and the - anti-phase tilt). The composition ranges are delimited by dashed lines. The structures are ordered energetically from lower/left to higher/right energy with the lower energy structure over the line delimiting the region. The small tilts should be exactly zero in the ideal $R3c$, $Pnma$ and $Pna2_1$ structures, but become finite (thus leading to complex tilting patterns) due to the Bi/La disorder.

We will discuss the relative stability of these phases, making use of the formation energy. This is a useful concept to interpret the energy differences of phases involved in solid solutions. The formation energy is defined as the difference in energy of the actual phase and the linear interpolation between the pure phases:

$$E_{for} = E - (1-x)E_{BFO} - xE_{LFO} \tag{4.1}$$

where E is the energy of a particular BLFO structure of composition x, and E_{BFO} and E_{LFO} are the ground-state energies of the pure compounds. The results can be observed in figure 4.7, note that at a given x several points may appear for one particular phase, each of them corresponds to a different Bi/La arrangement.

As can be appreciated from figure 4.7, the R phase of bulk BFO is the most stable structure for $x \lesssim 0.3$. At $x \sim 0.3$, we observe a first order phase transition to one of the orthorhombic phases[2]. For the composition range $0.3 \lesssim x \lesssim 0.65$ our results indicate that both phases $O1$ or $O2$ are degenerated, with the energy differences between them smaller than the dispersion associated to different Bi/La orderings. For $x \gtrsim 0.65$ we find that the $O2$ phase destabilizes: from that point on, our structural relaxations starting from the $O2$ structure recover the $O1$

[2]In figures 4.7, 4.8 and 4.9, the two dashed vertical lines mark respectively, the discontinuous transformation between R and O phases (at $x \sim 0.3$) and the loss of stability of the $O2$ structure (at $x \sim 0.65$)

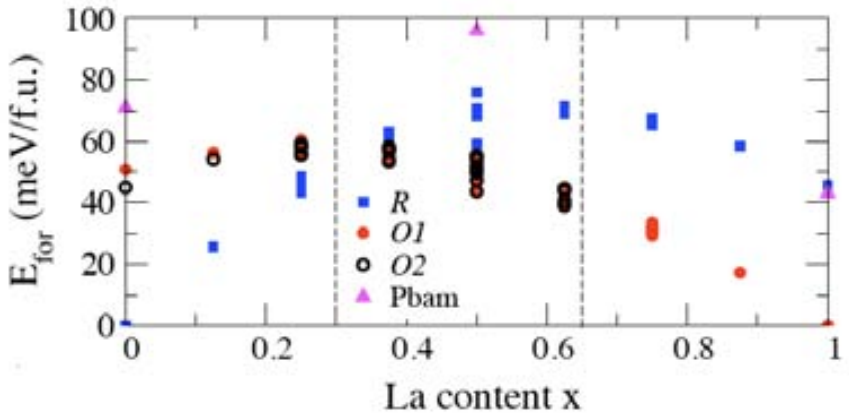

Figure 4.7: Formation energy of the three phases investigated as a function of composition (see text). For a given color and composition, each point in the figure corresponds to a different arrangement of the Bi/La atoms. The magenta triangles correspond to the $PbZrO_3$-like *Pbam* phase discussed in Subsection 4.6.

solution for all Bi/La arrangements. We could not study details of the transition from $O2$ to $O1$ with increasing La composition, as we are limited to $x = 1/8$ composition steps.

We have also plotted the volume per formula unit for all the structures studied. It can be noticed from figure 4.8, how the system undergoes a sudden volume contraction at $x \sim 0.3$ with the first order phase transition from rhombohedral to orthorhombic. As regards the intermediate region, our results have verified that both $O1$ and $O2$ are local minima of the energy for compositions $x \leq 5/8$. The implications of the simultaneous stability for these two phases and the possibilities it may open will be further discussed in detail.

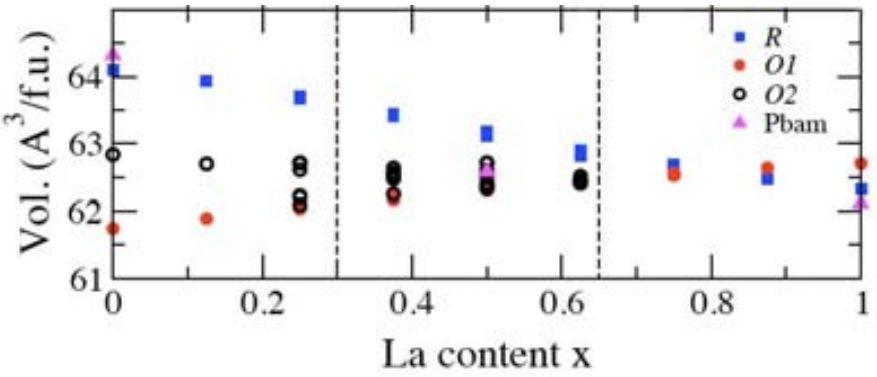

Figure 4.8: Cell volume per 5-atom formula unit, for all phases and Bi/La arrangements.

Table 4.1: Calculated lattice constant a, rhombohedral angle α, volume V_{rh} of the rhombohedral cell, and Wyckoff positions of $BiFeO_3$ and $LaFeO_3$ in the R phase

$BiFeO_3$	$R3c$ $a = b = c = 5.699$ Å			
	$\alpha = \beta = \gamma = 59.14^o$ $V_{rh} = 128.318$ Å^3			
Atom	*Wyck.*	x	y	z
Bi	2a	0.27831	0.27831	0.27831
Fe	2a	0.0000	0.0000	0.0000
O	6b	0.71522	0.16730	0.31509

$LaFeO_3$	$R\bar{3}c$ $a = b = c = 5.570$ Å			
	$\alpha = \beta = \gamma = 60.89^o$ $V_{rh} = 124.646$ Å^3			
Atom	*Wyck.*	x	y	z
La	2a	$\frac{1}{4}$	$\frac{1}{4}$	$\frac{1}{4}$
Fe	2b	0.00000	0.00000	0.00000
O	6e	0.67894	0.82106	$\frac{1}{4}$

As we have seen in the phase diagram of BLFO we obtained two FE phases. It is then important to understand the behavior of the polarization as the composition is changed. We computed the polarizationof R and $O2$ phases as a function of composition by considering the lowest-energy Bi/La arrangement for each x value. These results are presented in figure 4.9, where we can observe how the spontaneous polarization of BLFO s R phase decreases as the La content increases, disappearing at $x = 1$. At this limit (LFO) the R phase is no longer polar and the space group is $R\bar{3}c$ instead of $R3c$. For the $O2$ phase the same trend is

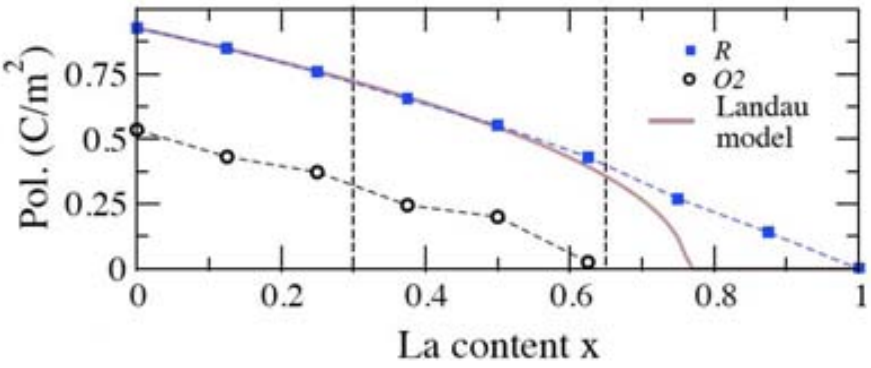

Figure 4.9: Polarization of the R and $O2$ phases as a function of composition, computed for representative Bi/La arrangements. The solid line is the result of the Landau model discussed in Section 4.5.

Table 4.2: Calculated lattice constant a, orthorhombic angle α, volume V_{orth} of the orthorhombic cell, and Wyckoff positions of $BiFeO_3$ and $LaFeO_3$ in the $O1$ phase

$BiFeO_3$	$Pnma$	$a = 5.719$ Å,	$b = 7.868$ Å,	$c = 5.488$ Å,
	$\alpha = \beta = \gamma = 90^o$		$V = 246.967$ Å^3	
Atom	$Wyck.$	x	y	z
Bi	$4c$	-0.05160	$\frac{1}{4}$	-0.00954
Fe	$4b$	0.0000	0.0000	$\frac{1}{2}$
O_1	$8d$	0.80062	-0.04722	0.19554
O_2	$4c$	0.52958	$\frac{1}{4}$	0.09677

$LaFeO_3$	$Pnma$	$a = 5.656$ Å,	$b = 7.929$ Å,	$c = 5.592$ Å,
	$\alpha = \beta = \gamma = 90^o$		$V = 250.811$ Å^3	
Atom	$Wyck.$	x	y	z
La	$4c$	-0.03825	$\frac{1}{4}$	-0.00791
Fe	$4b$	0.00000	0.00000	$\frac{1}{2}$
O_1	$8d$	0.78808	-0.04136	0.21242
O_2	$4c$	0.51867	$\frac{1}{4}$	0.07751

Table 4.3: Calculated lattice constant a, orthorhombic angle α, volume V_{orth} of the orthorhombic cell, and Wyckoff positions of $BiFeO_3$ in the $O2$ phase

$BiFeO_3$	$Pna2_1$	$a = 5.702$ Å,	$b = 5.507$ Å,	$c = 8.036$ Å,
	$\alpha = \beta = \gamma = 90^o$		$V = 252.338$ Å^3	
Atom	$Wyck.$	x	y	z
Bi	$4a$	0.4435	0.0016	0.2194
Fe	$4a$	0.5015	0.5007	0.4943
O_1	$4a$	0.2137	0.7074	0.0519
O_2	$4a$	0.1848	0.6876	0.4796
O_3	$4a$	0.5302	0.4171	0.2532

observed, with the main difference that the polarization of this phase goes to zero at the limit of stability of the phase ($x \sim 5/8$).

From a closer inspection of the relaxed structures for both cases, we found the origin of this behavior. Our results indicate that La^{3+} tends to prefer oxygen environments that are relatively isotropic and highly-coordinated, in contrasts with the large off-centering and anisotropic oxygen environment that are usual for Bi^{3+}. This strong off-centering of Bi is typically associated with the occurrence of a lone pair at the non-bonding side. For the case of Bi, its chemical preference results in the occurrence of large local electric dipoles (which add up to form the macroscopic polarization), while there is no such local dipole for the ideal La environments (i.e., those observed for LFO s $O1$ ground state as well as for its R-type PE phase of $R\bar{3}c$ symmetry).

4.4 Enhancement of the responses

Let us now focus on the response properties of the pure compounds. We will see how the response is enhanced upon substitution of a small fraction of the Bi/La cations. We identified two different mechanism behind the enhancement of the dielectric response as we dope the pure compounds BFO and LFO with La and Bi respectively. We will discuss them separately starting from the most simple to the more complex.

4.4.1 Enhanced response in Bi-doped $LaFeO_3$

We will begin our discussion with the enhancement of the response for the case of LFO and the Bi doped LFO (Bi:LFO). Our results shown that, when LFO is doped with Bi the dielectric response of the system is enhanced considerably (an enhancement of the 43% for the lattice-mediated part of the dielectric response was observed) see table (4.4). This enhancement is significant for the zz component, something that is related to the presence of a low energy (soft) polar mode with polarization along that direction. Such a soft mode is dominated by Bi s displacements, and is essentially identical to the distortion connecting the PE $O1$ structure with the FE $O2$ phase.

Table 4.4: Computed dielectric susceptibility tensors for $LaFeO_3$, $Bi_{1/8}La_{7/8}FeO_3$, and $Bi_{1/2}La_{1/2}FeO_3$ (with rocksalt ordered Bi/La cations) in the O1 phase (see text). Results given in the Cartesian (pseudo-cubic) setting defined in Fig. 4.1

	$LaFeO_3$	$Bi_{1/8}La_{7/8}FeO_3$	$Bi_{1/2}La_{1/2}FeO_3$
χ^{latt}	$\begin{bmatrix} 27 & 0 & 0 \\ 0 & 27 & 0 \\ 0 & 0 & 27 \end{bmatrix}$	$\begin{bmatrix} 35 & 0 & 0 \\ 0 & 37 & 0 \\ 0 & 0 & 39 \end{bmatrix}$	$\begin{bmatrix} 81 & -29 & -82 \\ -29 & 83 & 83 \\ -82 & 83 & 1186 \end{bmatrix}$

So far, these results are the expected ones according to our strategy. The responsible of the enhancement is the softening of the lattice, which is reflected in the presence of a Bi-dominated

soft mode. We can observe in table 4.4 for rocksalt-ordered $Bi_{1/2}La_{1/2}FeO_3$ where this soft-mode becomes barely stable, that the calculated response increases dramatically.

To make this argument more quantitative, let us recall that the lattice-mediated part of the dielectric response is given by (see Section 2.2)

$$\chi_{ij}^{latt} = \frac{1}{\Omega} \sum_s \frac{p_{si} p_{sj}}{\kappa_s} \tag{4.2}$$

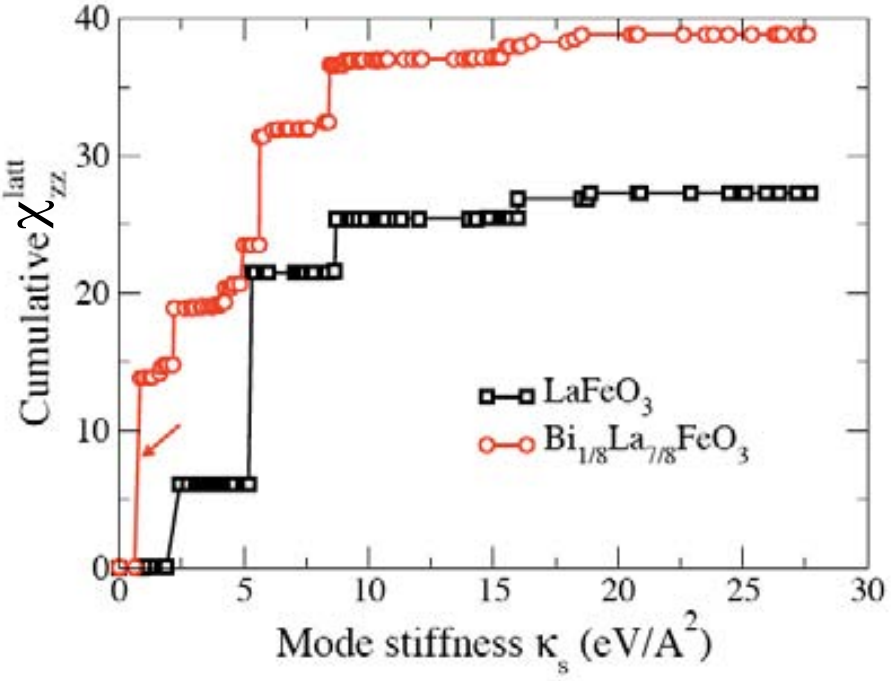

Figure 4.10: Cumulative plot of the χ_{zz}^{latt} component of the dielectric susceptibility tensor (see text) for the the O_1 phase of pure $LaFeO_3$ and $Bi_{1/8}La_{7/8}FeO_3$.

The existence of a soft mode implies the presence of an small eigenvalue κ_s, which may result in a large dielectric response. If we plot the evolution of the sum 4.2, as we add mode contributions, we obtain the cumulative plot shown in figure 4.10. Here we can see the details of the enhancement of χ_{zz}^{latt}; from the figure we confirm that, with the Bi doping, a soft mode (indicated with an arrow) appears and how this soft-mode is the responsible for essentially all the enhancement. We then confirmed by inspection of the mode eigenvector that this soft-mode is dominated by a Bi O distortion along z.

4.4.2 Enhanced response in La-doped $BiFeO_3$

The situation is different in the case of BFO and La doped BFO (La:BFO). A significant isotropic enhancement of the response can be appreciated from Table 4.5 for the χ^{latt} tensors computed for the R phases of pure BFO and $Bi_{7/8}La_{1/8}FeO_3$. The enhancement of the dielectric response in this case is not dominated by a single mode that becomes soft. Instead, we

appreciate that the number of modes that contribute to the dielectric response of La:BFO is much larger than in BFO. This can be visualized in the cumulative plot of figure 4.10.

Table 4.5: Computed dielectric susceptibility tensors for $BiFeO_3$, and $Bi_{7/8}La_{1/8}FeO_3$ in the R phase (see text). Results given in the Cartesian (pseudo-cubic) setting defined in Fig. 4.1

$$\chi^{latt} \quad \begin{matrix} BiFeO_3 \\ \begin{bmatrix} 31 & -5 & -5 \\ -5 & 31 & -5 \\ -5 & -5 & 31 \end{bmatrix} \end{matrix} \quad \begin{matrix} Bi_{7/8}La_{1/8}FeO_3 \\ \begin{bmatrix} 39 & -7 & -7 \\ -7 & 39 & -7 \\ -7 & -7 & 39 \end{bmatrix} \end{matrix}$$

If we compare the plots in figure 4.11 with those obtained for the previous case, the first difference is the profile observed. In contrast with the stepwise behavior of the Bi:LFO cumulative plot, for the La:BFO case we observe a quasi-continuous growth of the response in the range between 2 eV/Å and 10 eV/Å. Hence, we can see that instead of a single soft-mode driven enhancement, the response of La:BFO is the result of the appearance of many new polar modes, each of them giving a small contribution to the response. This implies that the presence of La in the BFO structure causes a loss of symmetry that allows that modes that were not polar in the pure BFO R phase acquire an small polarity.

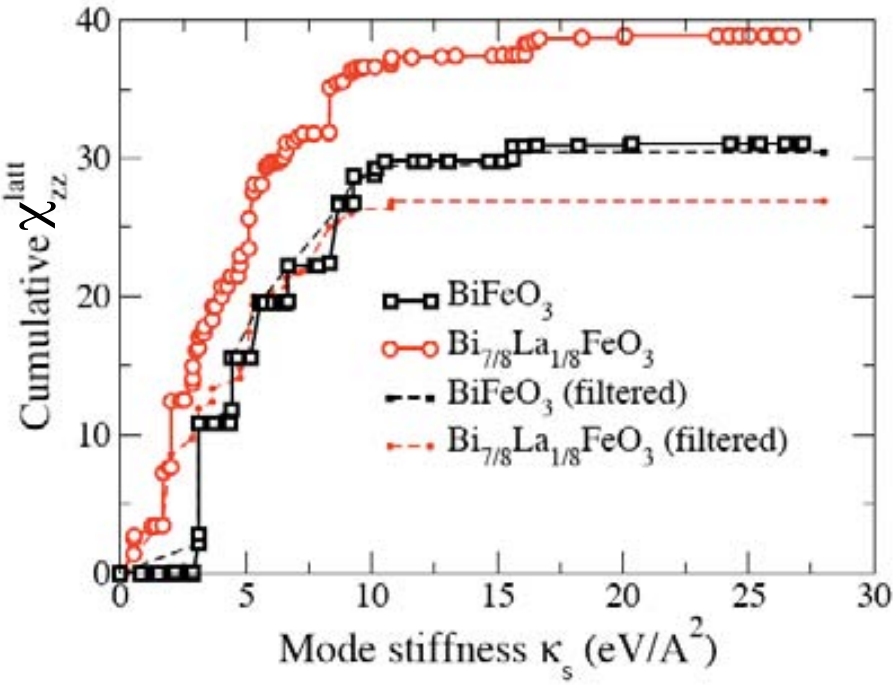

Figure 4.11: Cumulative plot of the χ^{latt}_{zz} component of the dielectric susceptibility tensor (see text) for the the R phase of pure $BiFeO_3$ and $Bi_{7/8}La_{1/8}FeO_3$.

In order to demonstrate that these small polarity modes are the responsible for the enhancement, we did a test. We filtered the small polarity modes from the sum 4.2 (we removed those

with $|p_{si}| < 2|e|$, where $|e|$ is the elemental charge) and plotted the resulting cumulative plot for both pure BFO and doped La:BFO (see Fig. 4.11). In the case of pure BFO, the filtered response is almost identical to the result including all the modes; in contrast, the filtered response of $Bi_{7/8}La_{1/8}FeO_3$ is significantly smaller than the total one, and the La-induced enhancement disappears completely.

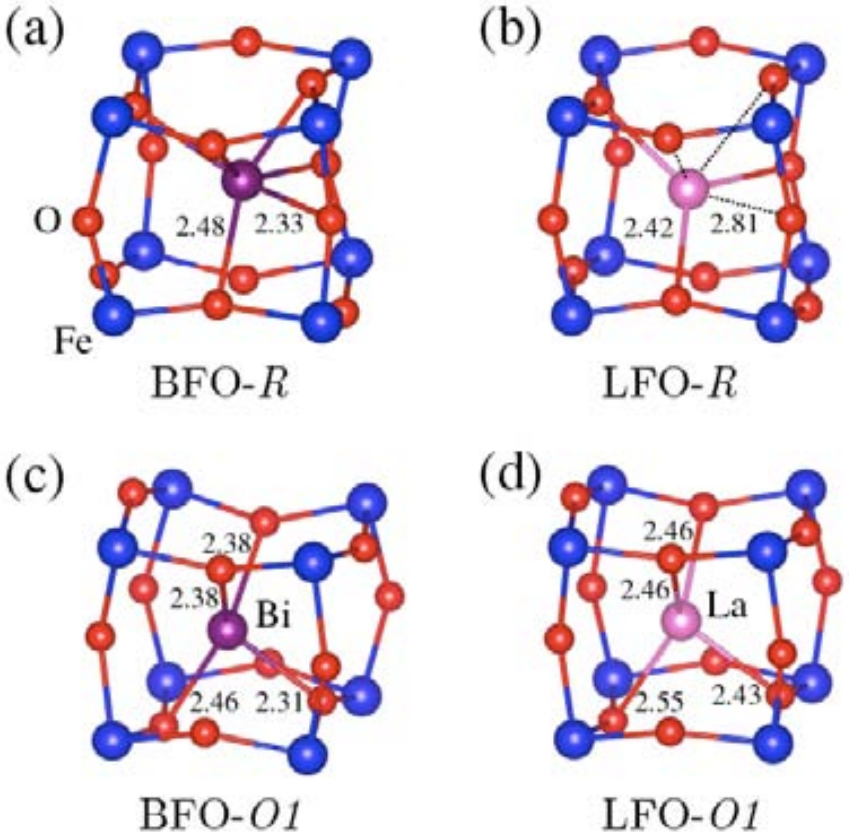

Figure 4.12: Atomic structure of the R [(a) and (b)] and O_1 [(c) and (d)] phases of BFO [(a) and (c)] and LFO [(b) and (d)], focusing on the coordination of the A-site cations Bi and La. Representative Bi O and La O bond distances ($\AA$) are indicated. In panel (b), dotted lines indicate the three La O pairs corresponding to the Bi O bonds of $2.33\AA$ shown in panel (a).

From these results it is natural to arrive to the questions: Why do we obtain so many new polar modes by doping the BFO-R phase with La? and, why did we not find a similar effect when substituting La by Bi in the LFO-$O1$ structure? The answer to this questions can be found if we look closely to the structural effects of the different doping. From the structural results discussed previously in section 4.3, we know that the R phase transforms continuously from a polar ($R3c$) to non-polar ($R\bar{3}c$) structure as we go from pure BFO to pure LFO. If we compare the structural data collected in tables 4.1 and 4.2 we may appreciate that, while for the R phase the BFO and LFO present marked differences (different space-group with the change in the symmetry mentioned before), for the $O1$ phase both compositions have a very similar structure. Thus, the La dopants induce a strong symmetry breaking in BFO-R, while the structural perturbation is relatively small when we dope LFO-$O1$ with Bi. This

occurs due to the differences in the chemical activity of Bi and La. While Bi presents an electronic configuration ($6s^2p0$) that allows for orbital rearrangements suitable to form very different bond complexes with neighboring oxygen atoms, La tends to place itself at a centro-symmetric position (this can be notice in the bond distance for La and Bi for both phases R and $O1$ in figure 4.12). When placed in the BFO-R structure, the La dopant tries to adopt its preferred configuration, which involves a large local distortion and, thus, a strong symmetry breaking; as a result, many modes that are not polar in the R phase of pure BFO acquire a small non-zero polarities. Such modes respond to the applied field, and result in a significantly enhanced response.

4.5 Phenomenological modeling of the response

So far we have discussed the enhanced dielectric response, and the atomistic origin of it. Now we would like to construct a Landau theory to model the observed effects. To our knowledge very few works have treated the composition variable explicitly in the Landau potential [41,42], even though such an extension of the theory would be of great help in predicting material properties of systems where the composition change result in phase transitions. We thus decided to build a simple Landau theory that accounts for the composition effects in BLFO.

We write the Landau potential for a single polarization component P and the composition x as

$$F(P, x, \mathcal{E}) = F^0(x) + \frac{1}{2}AP^2 + \frac{1}{4}BP^4 + \frac{1}{2}\gamma x P^2 - \mathcal{E}P \tag{4.3}$$

here, $F^0(x)$ contains all constant or P-independent terms. The composition x for a disordered solid solution, is a fully symmetric scalar variable and thus the lowest order symmetry invariant term, entering $F(P, x, \mathcal{E})$ in a form that is analogous to how temperature is treated.

As in the previous section, let us start with the simplest case. If we describe with the above model the case of Bi-doped LFO, the ground state is the PE $O1$ phase. Therefore we can assume $A > 0$ and neglect the 4th-order term B. We will also introduce a new convention, instead of using x for the composition we define $y = 1 - x$ as the compositional variable, with $y = 0$ corresponding to pure LFO. Then the y dependent dielectric susceptibility is given by

$$\chi = \frac{1}{A - \gamma y} \tag{4.4}$$

With this expression we can now fit the results for χ_{zz} given in table 4.4. Taking the values of χ_{zz} for $y = 0$ (LFO) and $y = 1/8$ ($Bi_{1/8}La_{7/8}FeO_3$), we can obtain the values of the parameters: $A = 4.178 \times 10^9\ Jm/C^2$ and $\gamma = 1.468 \times 10^9\ Jm/C^2$. If we look at the Landau potential for this case

$$F(P, y, \mathcal{E}) = F^0(y) + \frac{1}{2}AP^2 - \frac{1}{2}\gamma y P^2 - \mathcal{E}P \tag{4.5}$$

we may see that the positive value of γ implies a shallower potential well as the Bi content increases, with a lower energy cost associated to displacement along the FE instability. Hence, the application and interpretation of our Landau-like model is straightforward in this case.

Note also that the computed parameters suggest that the PE phase would become unstable for $y = A/\gamma = 2.85$ or, equivalently, $x = -1.85$; this negative (non-physical) x is compatible with the fact that the O_1 phase remains stable even in the limit of pure BFO.

For the case of La-doped BFO the analysis follows the same procedure, ut this time we have to remember that we are dealing with the properties of a FE phase. Thus, we need to consider all the terms in equation 4.3, with $A < 0$ and $B > 0$. With the equilibrium polarization given by:

$$P_{eq} = \sqrt{-\frac{A + \gamma x}{B}} \tag{4.6}$$

and the dielectric response by,

$$\chi = \frac{1}{2(A + \gamma x)} \tag{4.7}$$

Again, we fit the parameters to reproduce correctly (i) P_{eq} for $x = 0$ and $x = 1/8$ (where P is the modulus of the $[111]_{pc}$-oriented polarization of the R phase) and (ii) the response to a $[111]_{pc}$-oriented electric field at $x = 0$.[3] The values of the parameters are: $A = -1.818 \times 10^9\, Jm/C^2$, $B = 2.247 \times 10^9\, Jm^5/C^4$, and $\gamma = 2.375 \times 10^9\, Jm/C^2$. The positive value of γ now has two consequences: as the La content is increased the P_{eq} decreases and χ increases. This can be discussed in terms of the lattice dynamics: as x increases the FE instability becomes weaker and the potential well more shallow, making it less energetically costly to act on the polarization of the material, which means that the dielectric response is enhanced. These results were the ones we expected from the beginning; note that the idea of weakening the FE distortions to increase the dielectric response has been explored already in a number of works [35, 47].

However, as mentioned in the previous section, the origin of the shallowness of the FE energy minimum in La: BFO is not associated to a soft mode, but to the increased number of polar modes caused by the doping. Hence, this is an example of how a complex atomistic mechanism may be hidden by the Landau potential. For these complex materials, care must be taken when interpreting these simplified models, which nevertheless, have predicted the behavior of the P_{eq} in a wide range of compositions (see the solid line in figure. 4.9).

With respect to our proposed Landau potential, we want to comment on some features. Our fitted Landau potential, underestimates the strength of BFOs FE instability. For example, our potential gives an energy difference of about $150\, meV/f.u.$ between BFO s ground state and the $P = 0$ structure, while we know from first-principles studies that BFOs cubic PE phase lies more than $900 meV/f.u.$ above the R phase (see chapter 3). These differences are not surprising, as we fitted our potential to reproduce the equilibrium polarization and response properties of the FE phase, and not the energy difference with respect to the cubic structure. Another observation is that our fitted potential reproduces very well the evlution of the polarization of the R phase in a wide composition range (see Fig. 4.9). This is remarkable taking into account that the potential parameters were fitted to reproduce results obtained in

[3] We checked that alternative fitting strategies, for example demanding that the response is reproduced exactly for $x = 0$ and $x = 1/8$ and it give very similar results.

the limit of pure BFO. Hence, this seems to be a new example of how Landau potentials are often accurate well outside its expected range of applicability. This fact has been pointed out by other authors, as regards the modelization of temperature-dependent properties, [26] and our work suggests that the same is true in the case of a varying composition.

4.5.1 Electric field driven phase transitions

As we already mentioned our results show that at the intermediate compositions of BLFO the system can be in any of the orthorhombic phases $O1$ or $O2$ as they are nearly degenerated. This simultaneous stability of two very similar phases was unexpected, and thus we did a some calculations to confirm it and characterize it better. As we may appreciate in figure 4.13, we computed the interpolation path between the PE $O1$ phase and two $O2$ structures with the polarization pointing in opposite directions. As we may see from figure 4.13, depending on the ordering and the composition, the relative stability of phases $O1$ and $O2$ can be switched.

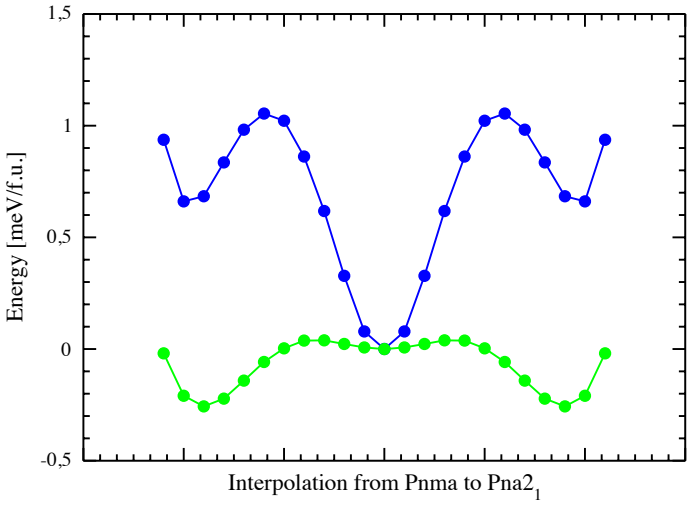

Figure 4.13: Energy variation along the path interpolated between the $O1$ and $O2$ phases for different compositions ($x = 2/8$ green, and $x = 3/8$ blue) and Bi/La arrangement. The distortion is given in arbitrary units as for each case the amplitudes are very different.

We want to discuss the possibilities that this multi-stability may open. We will chose a representative case for our discussions, which is the $x = 3/8$ and a quasi-rocksalt Bi/La arrangement [see Fig. 4.14(a)], where the PE phase is more stable than the FE phase. We can fit the energy vs polarization data of Fig. 4.14(a) to a sixth-order Landau-like potential of the form

$$F(P_z, \mathcal{E}_z) = F^0 + \frac{1}{2}AP_z^2 + \frac{1}{4}BP_z^4 + \frac{1}{6}CP_z^6 - \mathcal{E}_z P_z \tag{4.8}$$

Setting $F_0 = 0$, we obtain $A = 7.105 \times 10^8$ Jm/C^2, $B = -4.111 \times 10^10$ Jm^5/C^4, and $C = 4.760 \times 10^11$Jm^9/C^6, all expressed in SI units. (To compute these coefficients, we assumed

that the volume per elementary perovskite cell is approximately constant and equal to 62.2 Å^3 throughout the interpolation path.)

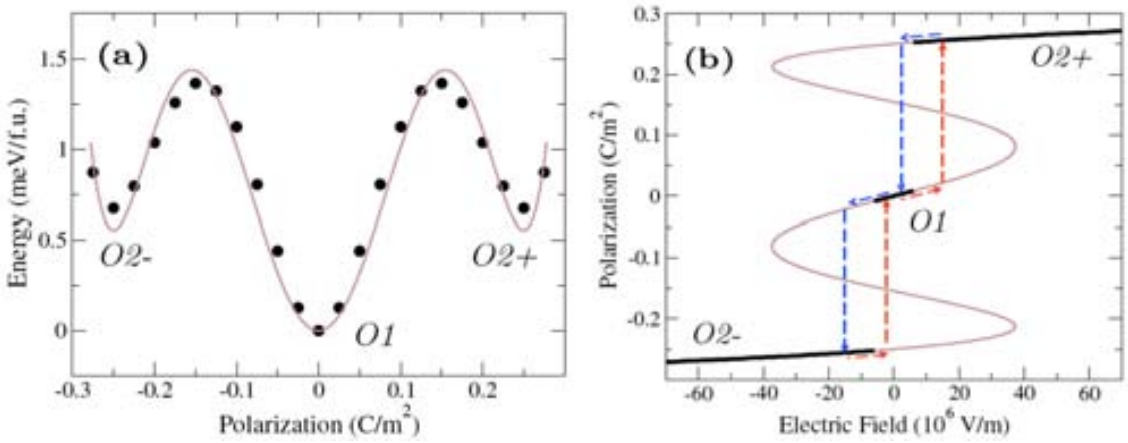

Figure 4.14: Panel (a): Energy variation along the path interpolating between the $O1$ and $O2$ phases obtained for a particular composition ($x = 3/8$) and Bi/La arrangement. We quantify the distortion in units of polarization assuming that a linear relationship between its amplitude and P_z. The points correspond to energies obtained from first-principles, and the line is a fit to a 6-th order Landau-like potential (see text). Panel (b): Polarization as a function of electric field, as obtained from the fitted Landau-like potential. Thicker lines mark the lowest-energy state. Dashed arrows sketch the transitions between the PE and FE phases that would occur in a hysteresis cycle.

From equation 4.8 we can compute the relation between P_z and $\mathcal{E}_z$ and obtaine the ideal polarization-switching cycle of figure 4.14(b). (We call it ideal because we are assuming a mono-domain switching, that occurs homogeneously throughout the whole material). The stability regions of polarization states for the phases $O1$ and $O2$ were determined and are indicated by thicker lines in Fig. 4.14. Note that if the system is at $O2-$ and the electric field is adiabatically switched to zero, the system probably will keep its structure in a metastable state until it transforms to the PE $O1$. This evolution through the possible metastable states, and the proposed hysteresis cycle, is sketched by the dashed lines.[4]

These results are very reminiscent of the experimental observations by Kan et al. in $Bi_{1-x}R_xFeO_3$ compounds (see figure 5 of Ref. [52]), and the field-driven PE-to-FE transition hypothesized in that work. The authors propose that such field induced transitions are a universal feature of the $Bi_{1-x}R_xFeO_3$. Our calculations suggest, in addition to the PE-$O1$ to FE-R transition proposed by Kan et al., the phases involved in such transitions for the BLFO might be the PE $O1$ and FE $O2$ structures. Also, our results suggest that such an $O1$ to $O2$ transformation might be possible in a rather wide composition range ($0.3 \lesssim x \lesssim 0.65$) in which both phases are quasi-degenerated.

[4]The quantitative values in such a hysteresis loop are not to be taken very seriously, as (i) the Landau-limit for polarization switching is clearly a crude approximation to reality and (ii) the parameters of the Landau potential in equation (4.8) may vary significantly depending on the specific composition and Bi/La arrangement considered.

4.6 Connection with experiment

BLFO had attracted the attention from the experimental community for a long time. However, the data collected about the structural transitions and the phases involved at intermediate compositions is often contradictory. Intermediate phases of orthorhombic, monoclinic, and triclinic symmetries, [30,85,93] and even incommensurate structures [75], have been reported. Interestingly, our results suggest that some of the phases proposed in the literature do not occur in BLFO. Examples of that are the phases compatible with our choice of simulation cell and which we did not found any local minima for such structures (the $C222$ and $C222_1$ variants reported by Zalesskii et al., [93] or the $Imma$ symmetry reported by Troyanchuk et al. [84]).

We would like to made an special mention to the recent work by Troyanchuk et al. [85]. These authors did a careful study, paying great attention to the sample preparation process for BLFO, and found a different intermediate phase at $x \sim 0.18$. This phase with a $Pbam$ space group (similar to that of the PE ground state of perovskite $PbZrO_3$) presents a 40 atom orthorhombic unit cell that is incompatible with the cell used in our simulations ($PbZrO_3$ cell is usually described as a $\sqrt{2}a \times 2\sqrt{2}a \times 2a$ repetition of the elemental perovskite unit, while our simulation cell is a $2a \times 2a \times 2a$ repetition). We wanted to check how this newly reported phase entered the picture obtained by our simulation of the BLFO phase diagram. Thus, we did first principles calculations to determine the formation energy of this $PbZrO_3$-like phase, using the crystallographic data provided in Ref. [85] as starting point of our structural relaxations. We considered three different compositions, the pure BFO and LFO limits and the $Bi_{1/2}La_{1/2}FeO_3$ with a rocksalt arrangement of the Bi and La atoms. The results are shown in Figs. 4.7 and 4.8 as magenta triangles. We find that the phase proposed by Troyanchuk et al. is metastable at all the compositions considered here[5], having a higher formation energy than the $O1$ structure for the selected compositions. Therefore our results suggest that this phase is not likely to appear in BLFOs phase diagram.

Therefore, from our calculations we do not have evidence to support any of the many structures that have been reported experimentally for BLFO s phase diagram, except for the stable phases of the pure compounds ($R3c$ for BFO and $Pnma$ for LFO). However, we acknowledge the fact that our simulations do not include thermal effects and are restricted to the investigation of local energy minima. For real materials, many factors that are beyond the scope of our calculations may contribute to the stabilization of structural phases that are not minimum of the energy. Nevertheless, we want to remark that, in the case of pure BFO, all the structures appearing in its phase diagram, seem to be local energy minima, (as discussed in Chapter 3). Hence, it is somewhat surprising that we were not able to validate with our simulations any of the intermediate phases reported experimentally for BLFO.

Our results suggest a possible explanation for the diversity of structural phases found in this compound. The positive formation energies shown in figure 4.7 indicate that there is an energy cost associated with the stabilization of the BLFO solid solution; in other words, at all compositions the most thermodynamically stable configuration would involve a phase separation in BFO-R and LFO-$O1$. The predicted instability of BLFOs solid-solved phase clearly indicates,

[5]We have not checked the structural stability of the $Pbam$ phase, and in principle, it might be a saddle point of the energy. Hence, their metastability is not confirmed.

that it may be a hard task to prepare samples in which the Bi and La atoms are well disordered. In fact, in many of the crystallographic works it was necessary to assume some sort of phase coexistence to model the structural data at intermediate compositions. Troyanchuk et al. [85] have described how the sample-preparation procedure can critically affect the results. All these facts suggest that most of the BLFO phases reported in the literature do probably occur in samples prepared in some specific conditions; yet, it is not so clear whether they may be stable phases of an ideal solid solution with Bi/La disorder. Let us also note that the difficulties to identify BLFO s most stable phase pertain to compositions in the $0.1 \lesssim x \lesssim 0.5$ range. Again, this seems consistent with our calculations, as that is the region in which (i) we find the crossover from the R phase to the orthorhombic structures $O1$ and $O2$, and (ii) according to our results BLFO can adopt different orthorhombic conformations that are essentially degenerate in energy.

4.7 Summary

We used first-principles methods to study the $Bi_{1-x}La_xFeO_3$ (BLFO) solid solution formed by the multiferroic $BiFeO_3$ (BFO) and the paraelectric antiferromagnet $LaFeO_3$ (LFO). Investigating BLFO s phase transitions as a function of the La content x, we find that at $x \sim 0.3$ BLFO transforms discontinuously from BFOs rhombohedral ferroelectric phase into an orthorhombic structure. The nature of such an orthorhombic phase could not be fully determined from the simulations, as we obtained two different states namely, ferroelectric $Pna2_1$ and paraelectric $Pnma$ that are essentially as stable in the $0.3 \lesssim x \lesssim 0.65$ composition range. We also found that the paraelectric $Pnma$ phase prevails for $x \gtrsim 0.65$. The phase coexistence at intermediate x values suggests some appealing possibilities; for example, our results indicate that an electric field might be used to induce paraelectric-to-ferroelectric phase transformations in this compound. We have also discussed the connection between our results and published crystallographic studies of BLFO solid solutions. Our simulations do not support any of the many different phases that have been experimentally proposed to occur at intermediate compositions. We have suggested some explanations for the experimental difficulties that hamper BLFO s structural characterization.

Additionally, we have shown that the chemical substitution of Bi/La atoms in the pure compounds leads to significantly improved response properties. (Our calculations were restricted to the dielectric susceptibility, and we argue that the obtained enhancement should be observed in the magnetoelectric response as well.) We have analyzed in detail the diverse origins of the increased responses,

- In the case of Bi-doped LFO, the enhancement is associated with an incipient ferroelectric instability involving Bi O distortions.
- In contrast, in La-doped BFO the improvement relies on the strong structural relaxation and local symmetry breaking caused by the La atoms, which result in the appearance of many new polar modes that react to an applied electric field.

We have shown that both effects can be captured by a phenomenological theory in which the composition x is explicitly treated in a Landau-like potential.

In conclusion, our first-principles results for the BLFO multiferroic solid solution, suggest that these compounds present many appealing features, ranging from improved response properties to the possibility of inducing structural phase transitions by application of electric fields. Further, we find that several BLFO phases are quasi-degenerate in energy in a wide composition range; thus, our calculations suggest that BLFO undergoes a very unusual morphotropic transformation that deserves a detailed experimental investigation. Finally, some of our results are strongly reminiscent of phenomena that has been experimentally found in similar solid solutions, as for example the $Bi_{1-x}R_xFeO_3$ compounds where R is a rare-earth lanthanide. Such similarities suggest that, BLFO may be a convenient model system, representative of this larger family of materials.

Chapter 5

Spin transitions in $BiFeO_3$ under pressure

The complexity of $BiFeO_3$ is not only structural as already mentioned. This compound may exhibit a wide variety of interesting phenomena, like for instance the manifold transition observed by Gavriliuk et al. [31 34] under hydrostatic pressure. These authors found that, at room temperature and in the 40-50 GPa range BFO undergoes a transition that involves a structural change, loss of magnetic order, and the metallization (see figure 5.1). These authors proposed a number of possible causes behind these transformations,

- An insulator-to-metal transition at which the $3d$ electrons of the Fe^{3+} ions are delocalized and form a conduction band. Then, the associated magnetic transition would be from an antiferromagnetic to a paramagnetic metallic state.
- A transition of the iron ions from a high-spin to a low-spin state. The iron ions in $BiFeO_3$ are in the high-spin state with $S = 5/2$ at normal pressure. The low-spin state of Fe^{3+} ions involves a non-zero magnetic moment as well $S = 1/2$, but the Neel point T_N with this configuration can be expected to be much lower than that of materials with Fe^{3+} ions in the high-spin state. In this case, the observed transition would be from a high-spin antiferromagnetic to the low-spin paramagnetic state. Further, it is assumed that the gap would close in the LS configuration.

The experimentalists at that point were not sure about the nature of the mechanism behind the transitions. When the experimental work came out, we wanted to understand the basics of the correlation between the structural, electronic, and magnetic properties of $BiFeO_3$ and clarify which scenario was the responsible for the simultaneous change of properties at the transition.This was in fact the first time our group worked on BFO.

5.1 Our approach

Model system considered

The goal of this project was to simulate the behavior of BFO under hydrostatic pressure, and capture the effect of very high pressures in the electronic structure. For that purpose, we employed a 10-atom simulation cell corresponding to the $R3c$ phase of BFO s ground

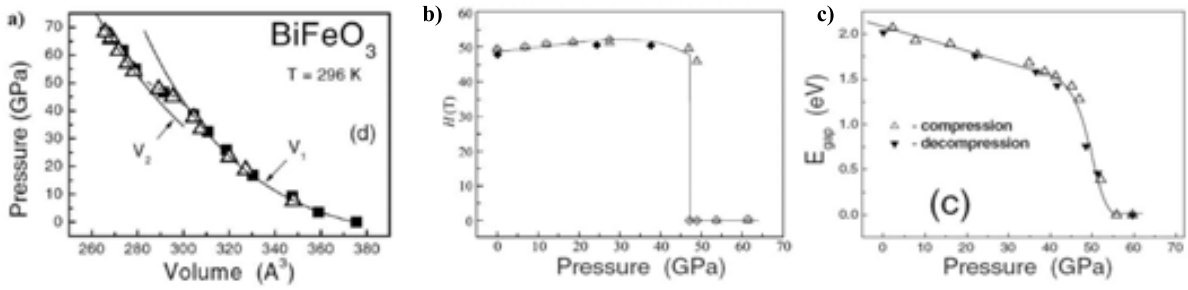

Figure 5.1: Figures taken from (citaaa 8,9); in a) the p-V curves are plotted, as can be seen there is a discontinous change in the curve corresponding to a structural transition; b) the magnetic hyperfine field drops to 0 at the transition, this effect occurs due to the transition of the $BiFeO_3$ crystal to a nonmagnetic state, thus, demonstrating the collapse of the localized magnetic moment of Fe; c) we may appreciate the closure of the electronic gap at the transition region, indicator of an insulator to metal transition.

state (see figure 5.2). Within this unit cell, we were able to study the ferromagnetic and G-antiferromagnetic orders, and also describe the different spin configurations (i.e. high/low spin and the possible mixture of both configurations) of Fe^{3+} $3d$ electrons.

In view of recent experimental evidences, we actually expect the HS-LS transition to take place whithin the *Pnma* phase which becomes stable at 11 GPa [38] (see sketch of the phase diagram in Fig. 3.1). However, the spin crossover transition can be expected to involve very local changes in the FeO_6 groups, which we expect to be very similar in the $R3c$ and *Pnma* structures. Thus, our simplified study of the pressure effects on the 10 atom cell, should account for the main effects. Our good agreement with the experimental observations indicates that this is actually the case.

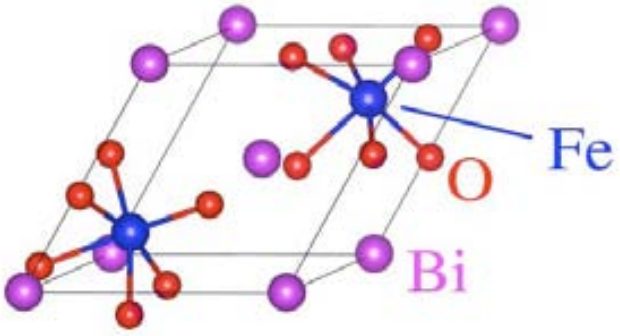

Figure 5.2: Representation of the 10 atom simulation cell used in our calculations with the $R3c$ symmetry corresponding to the BFO ground state

The effects studied here occur in a regime of very high pressures. We considered the interactions with the aid of the local-density approximation to DFT. We included the so-called $LDA + U$ correction of Dudarev et al. [**?**] for a better treatment of Fe s $3d$ electrons, as

implemented in the Vienna ab-initio simulation package (VASP). Our choice of LDA was conditioned by two facts: (1)-the GGA s available at the time were known to overestimate the ferroelectric distortions in perovskite oxides with lone pairs (e.g., $PbTiO_3$); (2)-the frequent use of LDA in most prior theoretical works on BFO. Thus, we used a rather simple approach to describe the physics of the system, which resulted to be enough to capture the qualitative description of the phenomena that we were interested in.

For this work, we compared the energies of different electronic phases, (insulating vs. metallic). in which the Fe^{3+} ions display different spin states. Describing this scenarios accurately constitutes a challenge for any ab-initio approach; particularly, the choice of U to enter the LDA+U scheme should be carried with caution. For this reason, we repeated all our calculations for the values 3 and 4 eV of the U parameter, and thus confirm that our qualitative conclusions are reliable. Unless otherwise indicated, the reported results are for $U = 3$ eV.

Computational details

The details of this calculations are essentially as those discussed in chapter 1, except for the following differences. We used a Γ-centered $7 \times 7 \times 7$ k-point grid for integrations in the Brillouin zone corresponding to the unit cell in Fig. 5.2, which is higher than the one chosen in chapter 1; this choice is justified by the fact that we want to study also metallic solutions, and a denser sampling of the Brillouin zone is needed. Also, the electronic wave functions were described with a plane-waves basis truncated at 400 eV. These calculation conditions were checked to render converged results for the quantities of interest, following a similar scheme as the one discussed in chapter 1.

Therefore, we ran a set of structural relaxations for a variety of atomic, electronic, and magnetic configurations. This allowed us to identify a large number of possible phases and determine their relative stability and properties. The structural relaxations were started from configurations in which we has broken the symmetry in order to allow the system be able to find the lowest energy phase. With the appropriate choice of the starting spin state in the calculations, we were able to obtain different electronic configurations e.g., high-spin (HS) and low-spin (LS) states of the Fe^{3+} cations, plus a phase with no local magnetic moments and metallic character that we will refer to as no-spin state (NS). For this purpose, we started the calculations from a spin polarized state, specifying the initial local magnetic moment on each atom (for Fe^{3+}, we used 5 unpaired electrons in the HS configuration and 1 unpaired electron for the LS). We neglected the incommensurate spin cycloid in BFO, for the inclusion of this feature would requires a considerably bigger simulation cell that we can not afford. Consequently we only considered collinear spin configurations.

5.2 Results for the structural and spin transitions

In order to extract the equation of state of the system, we performed structural relaxations at fixed volumes within the range of volumes of interest. As result we obtained the equation of state for the most relevant phases; i.e., the three phases that we found to be stable at some pressure range are:

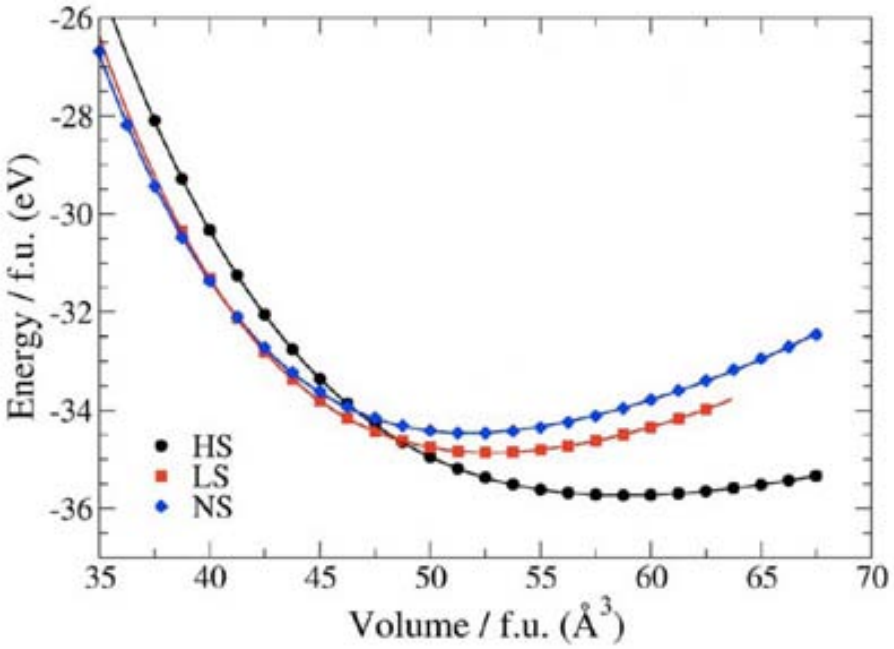

Figure 5.3: Computed equations of state for the most relevant phases obtained in this study.

- the $R3c$ phase of the ground state, with G-antiferromagnetism and the Fe^{3+} $3d$ electrons in a high-spin configuration, (HS) phase;
- a phase with $R\bar{3}c$ symmetry and a low-spin configuration of the Fe^{3+} $3d$ electrons, (LS) phase;
- and a third phase of $R3c$ symmetry with a null magnetic moment and a metallic behavior, (NS) phase.

which can be seen in figure 5.3.

We fitted our results to obtain the equation of state $E(V)$, from which we have derived the pressure dependence on volume $p(V) = -\partial E/\partial V$; by inverting this relationship we also get $V(p)$. A better description of the phases stability can be obtained if, instead of plotting the equation of state, we draw the enthalpy of the system:

$$H(p) = E(V(p)) + pV(p) \tag{5.1}$$

We computed the enthalpy H for all the points obtained from our calculations, and drew the enthalpy differences for the relevant phases with respect to the HS phase. The result can be seen in figure 5.4 (a), where we can appreciate that for up to 36 GPa the most stable phase found was the HS phase, over 36 GPa we observed the LS phase which remained stable up to 72 GPa where our calculations point to the NS phase.

We have plotted the dependence on pressure of the key properties of the material in figure 5.4. Here we can observe clearly the simultaneous changes associated with the first order transition between the HS and LS phases, namely, the drop in volume (panel b), and the change in the

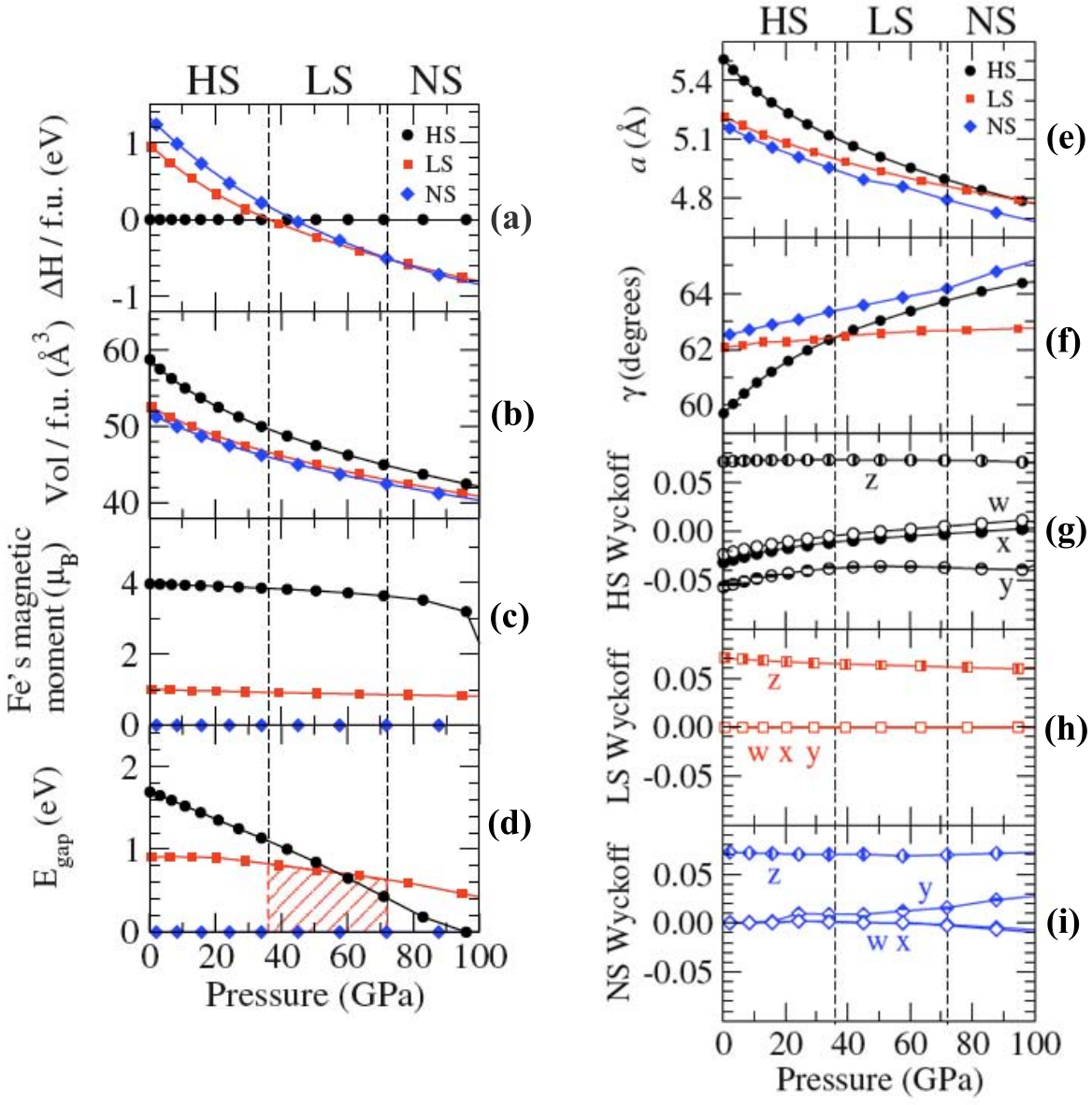

Figure 5.4: Variation of the fundamental properties of the system with respect to pressure. We show for for the relevant phases (HS, LS, and NS): panel a) the variation of the enthalpy ; panel b) Volume vs pressure curves; panel c) Change of local magnetic moments with pressure; panel d) Electronic gap of the material; and in panels from e) to i)we have plotted the dependence on pressure of the structural parameters defining the phases of interest. Dashed lines indicate the transition pressures.

Fe magnetic moments (panel c). It is interesting to note how the magnetic moments are nearly pressures independent within both the HS and LS phases.

We can express the obtained phases as the ideal cubic perovskite structure plus the amplitude of primary distortions (see table 5.1). The structural induced changes may be observed from figure 5.4, where we present the amplitude of the primary distortions defining the structural phases (see table 5.1). These primary distortions can be classified according to their symmetry as:

- polar displacements associated with irreducible representation Γ_4^- (symmetry labels correspond to the BZ of the five-atom cubic cell).
- antiferrodistortive (AFD) patterns corresponding to anti-phase (R_4^+) rotations of the O_6 octahedra around the [111] direction of the cubic structure.

For all the phases, we found oxygen octahedra rotations quantified by the R_4^+-type parameter z, defined in table 5.1. Our calculations show that such rotations remain relatively unchanged under compression. However, as regards the FE distortions described by the Γ_4^--type parameters w, x, and y, they are always present for the HS phase, but are completely absent in the LS phase. At very high pressures, in the NS phase, distortions breaking the inversion symmetry appear and increase with further compression.

Table 5.1: Structural parametrization for a unified description of all the phases here discussed. Listed are the occupied Wyckoff orbits according to the rhombohedral setting of the $R3c$ space group. The locations of the representative atoms are given as the sum of a reference position plus Γ-type (corresponding to zone center distortions) or FE distortion and R-type (corresponding to zone boundary distortions) or antiferrodistortive distortions. The representative Bi is chosen to be at the origin.Whenever both Γ- and R-type distortions occur, we get the $R3c$ space group; when only Γ-type (R-type) distortions exist, we obtain $R3m$ ($R\bar{3}c$) ; and when both Γ- and R-type displacements are null, we recover the ideal $Pm\bar{3}m$ perovskite structure. In all cases, the 10-atom unit cell is fully specified by a single lattice parameter $a = b = c$ and the rhombohedral angle $\alpha = \beta = \gamma$.

			Distortions	
Atom	Wyck.	Reference pos.	FE dist. (Γ_4^-)-type	AFD dist. (R)-type
Bi	$2a$	$(0,0,0)$	$+(0,0,0)$	
Fe	$2a$	$(1/4,1/4,1/4)$	$+(w,w,w)$	
O	$6b$	$(1/2,0,1/2)$	$+(x,y,x)$	$+(z,0,-z)$

The observed FE distortion has its origin in Bi s stereochemical activity. Basically, what we observed in the HS phase is that the Bi atoms move along the [111] direction to approach the three O atoms forming a face of the neighboring oxygen octahedron. In the LS phase, there

is a change in Bi coordination: we find BiO_3 planar groups in which the three oxygen atoms binding with the Bi atom belong to three different O_6 octahedra. In the NS phase, these planar groups are also present, but coexist with an small distortion that breaks the center of inversion (see figure 5.5).

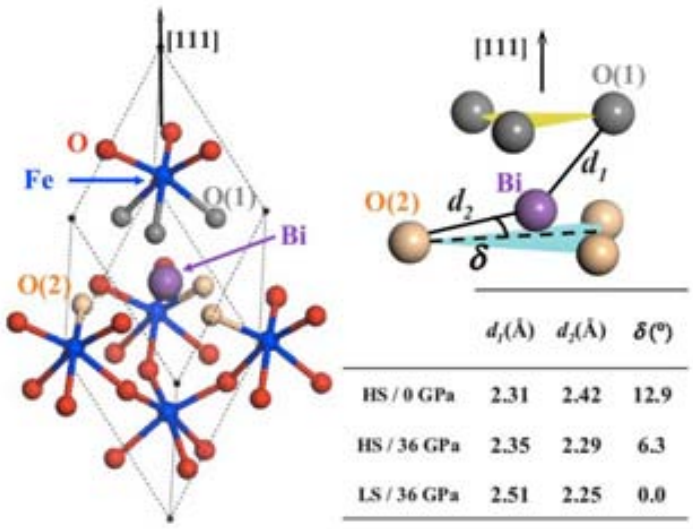

	d_1(Å)	d_2(Å)	δ(°)
HS / 0 GPa	2.31	2.42	12.9
HS / 36 GPa	2.35	2.29	6.3
LS / 36 GPa	2.51	2.25	0.0

Figure 5.5: Structural details of Bi activity, we may appreciate the changes in Bi coordination as the distance between Bi and the neighboring oxygens change with pressure.

As discussed in previous chapter Bi s coordination is the main factor controlling the occurrence of the FE distortion in BFO. The same is true in the system under compression.

So far we have seen that our calculations show that, as BFO is pressurized, two main changes are induced: the change in Bi coordination (with the subsequent loss of FE distortion) and the change in the Fe^{3+} electron s configuration (from high to low spin). It is important to note that, even if not competing in energy, we obtained many metastable phases exhibiting different combinations of the above mentioned features. For instance, besides the observed phase with a LS configuration, we found solutions with intermediate spin (two electrons paired and three unpaired electrons, in each Fe atom) and a mixed spin phase (one iron in the HS and the other one in the LS configuration in the 10-atom cell). Such mixed spin phase was found to be stable in a very narrow range of pressure (35 to 37 GPa). This result, which we find interesting and exotic, will be kept outside the discussion, as the stability range is too small to be relevant.

The computed HS-LS transition pressure is about 36 GPa, in a reasonable agreement with the experimentally observed one at 40-50 GPa. The predicted presence of many competing metastable phases, being consistent with the diffuse transition reported by the experiments. Further, our results for $p(V)$ in figure 5.6 are in good qualitative agreement with the experi-

mental data.

We have computed the bulk modulus (B_0) of the HS and LS phases, and find them to be markedly different. The computed bulk modulus is very sensitive to pressure, increasing strongly with compression. For the HS phase we obtained $B_0 = 130 - 300$ GPa within its stability range (from 0 to 36 GPa), and $B_0 = 400 - 500$ GPa for the LS phase (for pressures between 36 and 72 GPa). The HS phase is significantly softer than the LS near the transition point, as observed experimentally *Gavriliuk et al.* [34] give a single value for the bulk modulus of their low-pressure phase (corresponding to the HS phase) of 76 GPa, and for the high-pressure phase (corresponding to the LS phase) they report 290 GPa, which makes a comparison difficult. Moreover, from the data in their work we deduce $B_0 = 180$ GPa for the low-pressure (HS) phase, a value much greater than the one of 76 GPa given by the authors themselves.

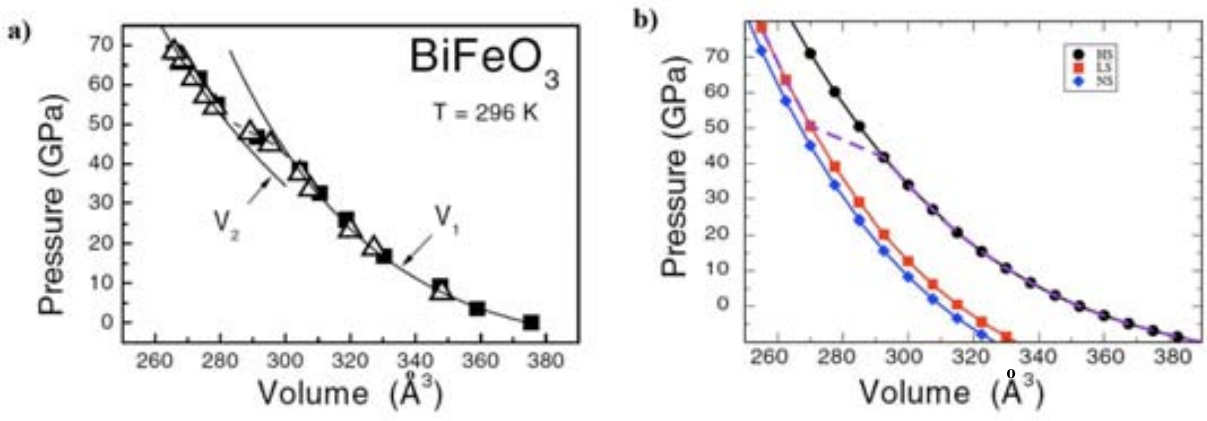

Figure 5.6: In this figure we can compare the results obtained by the experiment and those obtained by us for the Volume vs. Pressure curves. In the panel a) the results reported by Gavriliuk et al.; panel b) show our results, where we ca appreciate a close agreement with the experiment (dash-lines sign the stable phase).

Finally, the pressure dependence of the enthalpy difference between the LS and HS phases was experimentally determined to be 12 meV/GPa at the transition region, and we obtained about 15 meV/GPa. All this evidence supports the obtained LS phase, is a good representation of the one involved in the experiments done by *Gavriliuk et al.*

5.3 Metallization at the HS-LS transition

The computed HS phase, has a G-AFM spin order and is insulating, as expected in accordance with the phase corresponding to BFO groundstate. The energy differences between G-AFM and FM orders for the HS configuration rises with pressure, from 0.27 eV/f.u. at 0 GPa to about 0.65 eV/f.u. at 36 GPa. These observations are compatible with the experimentally reported high ordering temperature $T_{Neel} = 643$ K at 0 GPa, and its increase with pressure. We may appreciate from figure 5.4 d) that the HS phase exhibits a relatively large energy

gap, which decreases under pressure. Experimentally, the gap was observed to decrease from 2.0 eV to 1.5 eV in the range from 0 to 40 GPa, with a variation of $\sim$ 12.5 meV/GPa; [34] our predicted gap changes from 1.7 to 1.2 eV between 0 and 36 GPa, with a variation of 13.9 meV/GPa; thus, our results are in a reasonable agreement with the experiments.

However, if we look at the LS phase, our results reveal a more complex scenario. For the LS phase, throughout its stability range, the G-AFM and FM orders are quasi degenerate with a difference in energy of less than 0.03 eV/f.u. Moreover, their relative stability is switched when the pressure is increased. Thus, for the LS phase, the magnetic ordering temperature will be at least an order of magnitude smaller than that of the HS phase. These results suggest that if we heat the LS phase up to room temperature, it will appear in a disordered paramagnetic state.

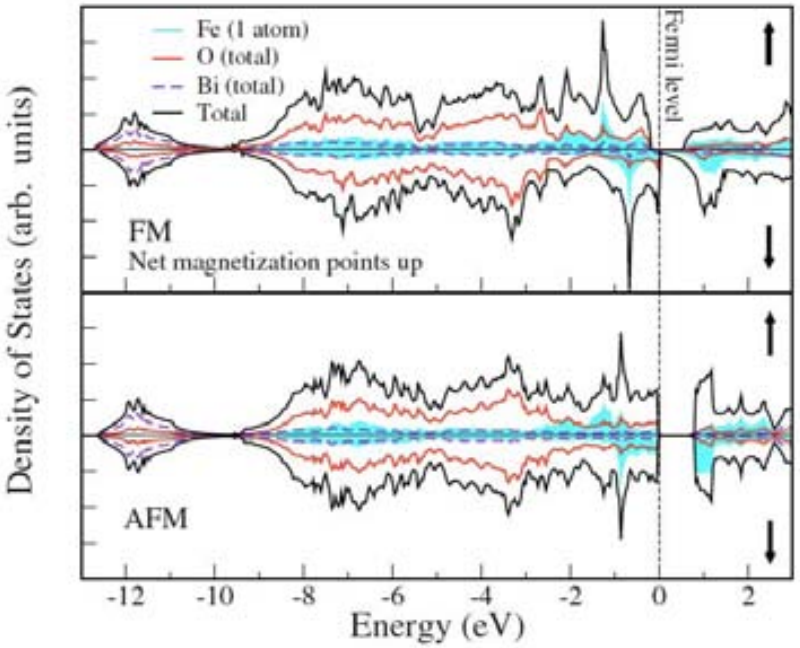

Figure 5.7: Density of states of the LS phase for the FM and G-AFM configurations of the LS phase of BFO at 50 GPa. We observe a half metallic solution for FM configuration.

We also found that, for the LS phase, the electronic structure depends strongly on the spin arrangement (see Fig. 5.7). While the G-AFM order presents a gap of around 0.8 eV, for the FM order the system is half-metallic. Thus, at room temperature a metallic behavior is expected, as the thermal averaged equilibrium state should present a significant electronic density of states at the Fermi level.

Therefore, the BFO s pressure driven HS to LS phase transition is accompanied by the simultaneous changes in structure, spin configuration, magnetic order, and insulator to metal transformations.

5.4 Implications of our results

Our simulations are essentially in agreement with the mechanism proposed by Gavriliuk et al. [34] to explain the observed pressure driven transitions. However, it is important to remark that, while our calculations were done for the system at 0 K, the experiments were performed at T_{room}.

Computing the temperature vs. pressure ($T-p$) phase diagram ab-initio is beyond the scope of our work. We can nevertheless estimate the temperature stability range of the phases by calculating the enthalpy differences with respect to the cubic phase. Such a quantity should be roughly proportional to the temperature at which the transition to the cubic phase occurs. For 0 GPa, we obtained a difference of 0.88 eV/f.u. between the $R3c$ HS phase and the lowest energy cubic phase, which displays HS configuration. This quantity is relatively large, as expected for a transition that occurs at very high temperatures ($\sim$ 1000 K). The difference in enthalpies decreases moderately when the pressure is increased. For instance, at 50 GPa the difference between the LS phase and the lowest energy cubic phase (which presents LS configuration at these pressures), is about 0.60 eV/f.u., a value that would correspond approximately to a transition temperature in the 700-800 K range. This results supports our LS phase as the one observed experimentally by *Gavriliuk et al.* at room temperature.

We want to comment on the possible implications of our study for the $T-p$ phase diagram of BFO. Catalan et al. [15] have obtained, for the high temperature regime, a cubic phase with metallic character. The same authors have proposed this cubic phase as the equilibrium state corresponding to the high pressure and low temperatures for this material. Our calculations, even if restricted to the simple 10-atom simulation cell, included as a possibility the ideal cubic perovskite. However, for pressures in a range up to 100 GPa, we were not able to find this phase as the most stable one. For all the range of pressure explored in this study, we always observed some distortions lowering the symmetry, like the O_6 octahedra tilting, and the ferroelectric distortion associated to Bi s coordination. This is consistent with the observations by *Gavriliuk et al.* [34] and *Haumont et al.* [40] who reported a non-cubic structure at high pressures and room temperature. Also in a very recent paper by *Guennou et al.* have reported a careful study of BFO under hydrostatic pressure and have shown that indeed the high pressure phase is not cubic. [38]

Let us make a final comment on our computational approach and the quantitative results obtained. As already mentioned, our simulations have employed the LDA+U functional. The choice of the U, and the way to deal with the d-electrons under very high pressures, is not an obvious one. For that reason, we repeated all our calculations with two values for the U describing the Fe^3 $3d$ electrons, $U = 3$ and 4 eV. Our qualitative results were identical, the only difference been at the quantitative level where we observed a positive shift of the transition pressures as we increased the value of U. For instance, the computed pressure for the HS-LS transition for $U = 3$ eV was of 36 GPa, while for $U = 4$ eV, occurs at 42 GPa. Our results for the LS-NS transition are less obvious: the transition pressure in this case depends strongly on the choice of U (it is shifted by almost a factor 2, obtaining 130 GPa for $U = 4$ eV). thus, it is clear that we do not have a quantitative predictive theory at very high pressures.Yet, given the drastic simplifications made in this work as regards the simulated system (i.e. we restricted to a 10-atom unit cell), we thought it was not reasonable to insist further in the

quantitative accuracy of the LDA+U scheme employed.

5.5 Summary

In this work we have identified the main structural, electronic, and magnetic effects that occur in $BiFeO_3$ under compression and how they are connected. More precisely, we found that under hydrostatic pressure the system:

- suffers a change in the coordination of the Bi atoms, which tend to form BiO_3 planar groups
- undergoes a HS-LS crossover transition for Fe^{3+} at pressures around 40 GPa
- the magnetic interactions are relatively weak in the LS phase, which should result in a relatively low magnetic ordering temperature
- the electronic structure of the LS phase strongly depends on the magnetic order, which suggests that, at room-temperature the paramagnetic LS phase will be metallic.

These are drastic transformations, which involve relatively large energy scales. Thus, these predictions seem reliable, in spite of the approximations made for our theoretical study. Our predictions for the HS-LS transition are thus consistent with the manifold transformation observed experimentally by Gavriliuk et al., [34] and provides an explanation for it.

Let us conclude by saying that our investigations were by no means exhaustive and many issues remain open. For example, our results strongly suggest that BFO will not present a cubic phase $Pm\bar{3}m$ at high pressures; however, we cannot deduce from our calculations the space group of the high-pressure phases. There are many possibilities involving unit cells larger than the 10-atom one used in our simulations, which were considered in this work. Similarly, the possibility of complex magnetic orders occurring at high pressures has not been explored. Finally, for more accurate quantitative calculations of the transition pressures, and the properties of the high-pressure phases, it would be required the use of sophisticated first-principles techniques that can improve over our LDA+U results.

Chapter 6

Towards a systematic treatment of complex structural phases in perovskite oxides

As already mentioned, perovskites are materials with singular properties. The ideal perovskite structure is quite symmetric, it can be explained as a lattice of corner sharing oxygen octahedra with interpenetrating simple cubic lattices of cations (see Fig. 1.1). However, perovskites present a rich phase diagram with phases exhibiting different physical properties. Understanding these structural phase transitions and under which conditions they may occur, is then crucial for the development of new materials with enhanced properties.

Ideally, we want to have a phenomenological model able to explain and predict the structural phases of a material as complex as $BiFeO_3$ (BFO). Such a theory could be used to predict the stability of phases under different conditions and thus, obtain relevant information about the properties of the material. However as explained before, BFO has a very complicated energy map with plenty of minima. The first step into developing such theory would be to identify the primary distortions that need to be considered explicitly in it.

Recalling the distinction done among the different distortions that are common to perovskites, two major group were identified,

- the ferroelectric (FE) polar distortions, associated with the freezing of a soft mode at Brillouin zone center (Γ modes), and described in terms of the polarization $\mathbf{P}$.
- the antiferrodistortive (AFD) distortions, composed by in-phase and/or anti-phase tiltings of the oxygen octahedra, corresponding to the condensation of a soft mode at Brillouin zone boundary (type M and R modes, respectively). These will be described by two order parameters, defined as $\mathbf{M} = (m_x, m_y, m_z)$ for the in-phase rotations, and $\mathbf{R} = (r_x, r_y, r_z)$ for the anti-phase rotations, around the principal perovskite axes x, y, and z.

The occurrence of different combination of such distortions results in the most commonly observed structures among the oxide perovskites, see table 6.1.

The energetics of the FE distortions was studied in the seminal paper by *King-Smith and Vanderbilt* [54], where they discussed the total energy surface as function of $\mathbf{P}$, correctly

FE	AFD	$FE + AFD$
$\mathbf{P}[x,y,z]$	$a^{\circlearrowleft}b^{\circlearrowleft}c^{\circlearrowleft}$	$\mathbf{P}[x,y,z] + a^{\circlearrowleft}b^{\circlearrowleft}c^{\circlearrowleft}$
$R3m$ $_{\mathbf{P}[111]}$	$R\bar{3}c$ $^{a^-a^-a^-}$	$R3c$ $^{a^-a^-a^-}_{\mathbf{P}[111]}$
	$Pnma$ $^{a^-a^-c^+}$	$Pna2_1$ $^{a^-a^-c^+}_{\mathbf{P}[001]}$
$P4mm$ $_{\mathbf{P}[001]}$	$I4/mcm$ $^{a^0a^0c^-}$	

Table 6.1: Most common symmetries of perovskites in nature, and their respective type of distortion from the ideal cubic. Again we have employed the Glazer notation, with $a^{\circlearrowleft}b^{\circlearrowleft}c^{\circlearrowleft}$, letters refer to tilts around axes [100], [010], [001] respectively; $\circlearrowleft$ superscript refer to whether the tilting is in-phase(+) or anti-phase(-) along certain axis, or absent(0); $\circlearrowleft = +, -, 0$ and $a^+a^+b^-$ means two equal in-phase tilts along [100] and [010] and a different anti-phase tilt along [001]

predicting the groundstate symmetries for classic FE compounds ($BaTiO_3$,$KNbO_3$, $PbTiO_3$ among others). Later, they extended their study to include the AFD and the FE distortions in tetragonal $SrTiO_3$. [76] However, their theory was not intended to consider more complex scenarios than that of the energetics of the tetragonal AFD distortions. In order to describe more complex structures, it is needed to include all the possible tilts which in principle occur individually (as in the tetragonal $a^+b^0b^0$ phase) or combined (as in an orthorhombic $a^-a^-c^+$ phase). Thus, a theory that includes the AFD order parameters $[E(\mathbf{P}, \mathbf{M}, \mathbf{R})]$ is still missing, and might be of great use to predict and explain the role played by such distortions in the stabilization of structural phases in many perovskite oxides.

6.1 Modeling the energetics of oxygen-octahedra rotations

We want to describe the energetics of perovskites in terms of the primary order parameters. As a first step, we will derive the energy in terms only of the **M** and **R** type of distortions (i.e. rotations of the oxygen octahedra). We chose to construct a 4-th order expansion of the energy around the cubic phase, and analyze if it is enough to correctly describe a relatively simple system. The energy of the system for certain amplitude of the distortions **M** and **R** is obtained from,

$$E(\mathbf{M}, \mathbf{R}) = \min_{\mathbf{u}|\mathbf{M},\mathbf{R}} E^{DFT}(\mathbf{u}) \tag{6.1}$$

where the generalized vector **u** describes an arbitrary atomic structure, and the minimization is over **u** compatible with specific values of **M** and **R**. The energy expansion will be written as a linear combination of sets of invariant polynomials in the components of the order parameters:

$$E(\mathbf{M}, \mathbf{R}) = E_{cubic} + E(\mathbf{M}) + E(\mathbf{R}) + E_{int}(\mathbf{M}, \mathbf{R}). \tag{6.2}$$

4^{th} Order Theory

In analogy with the approach adopted by Vanderbilt and King-Smith [54]. we want to have a general model to describe similarly the phase transitions involving the O_6 octahedra rotations. Thus, we have expanded the energy up to 4-th order in $\mathbf{M} = (m_x, m_y, m_z)$ and $\mathbf{R} = (r_x, r_y, r_z)$,

$$\begin{aligned} E(\mathbf{M},\mathbf{R}) =& E_0 + \kappa^+ m^2 + \kappa^- r^2 + \alpha^+ m^4 + \alpha^- r^4 + \gamma^+(m_x^4 + m_y^4 + m_z^4) \\ &+ \gamma^-(r_x^4 + r_y^4 + r_z^4) + \alpha^{\pm} m^2 r^2 + \vartheta(m_x^2 r_x^2 + m_y^2 r_y^2 + m_z^2 r_z^2) \end{aligned} \tag{6.3}$$

where:

$$m^2 = (m_x^2 + m_y^2 + m_z^2) \qquad ; \qquad r^2 = (r_x^2 + r_y^2 + r_z^2)$$

and

$$m^4 = (m^2)^2 = (m_x^4 + m_y^4 + m_z^4 + 2m_x^2 m_y^2 + 2m_x^2 m_z^2 + 2m_y^2 m_z^2)$$
$$r^4 = (r^2)^2 = (r_x^4 + r_y^4 + r_z^4 + 2r_x^2 r_y^2 + 2r_x^2 r_z^2 + 2r_y^2 r_z^2)$$

Note that κ^+, κ^-, α^+ and α^- are the coefficients describing the isotropic part of the energy (i.e., the part that remains invariant under rotations of $\mathbf{M}$ and $\mathbf{R}$) while γ^+, γ^- and ϑ account for the anisotropy. The superscripts in the coefficients account for the (+) in-phase and (-) the anti-phase rotations parameters. The coefficients κ^+ and κ^- are related to the eigenvalues of the force-constant matrix of the cubic reference structure; when $\kappa^{+\,or\,-} < 0$ the corresponding distortion is a instability of the cubic phase. The coefficients $\alpha^{\pm}$ and ϑ account for the coupling between the in-phase and the anti-phase rotations, with ϑ quantifying the energy cost of complex tilts (i.e., those involving a combination of in-phase and anti-phase rotations around one axis) in the system.

Analytic solution for high-symmetry tilt phases

Let us derive the analytic expressions for the possible energy minima along the high symmetry directions. For the time being, we will focus on the anti-phase tiltings, as the derivation for the in-phase tilting is analogous. The energy expression for the anti-phase tilting $\mathbf{R}$ is:

$$E(\mathbf{R}) = E_0 + \kappa^- r^2 + \alpha^- r^4 + \gamma^-(r_x^4 + r_y^4 + r_z^4) \tag{6.4}$$

Considering the presence of tilting along the high symmetry directions, we obtained:

For the tetragonal case with $\mathbf{R} \,||\, [100]$ (i.e. $a^- b^0 b^0$ tilting) the energy can be written as,

$$E(r_x) = E_0 + \kappa^- r_x^2 + \alpha^- r_x^4 + \gamma^- r_x^4 \tag{6.5}$$

For the existence of a extrema it must satisfy:

$$\frac{dE(r_x)}{dr_x} = 2\kappa^- r_x + 4\alpha^- r_x^3 + 4\gamma^- r_x^3 = 0 \tag{6.6}$$

From this equation we may extract the amplitude of the tilting and the energy of the minima to be:

$$a^-b^0b^0: \qquad r_x^2 = -\frac{\kappa^-}{2(\alpha^- + \gamma^-)} \qquad E = E_0 - \frac{(\kappa^-)^2}{4\alpha^- + 4\gamma^-}$$

Proceeding in the same manner for the other directions we obtain that:
for $\mathbf{R}\,||$ in the [110] direction, taking $r_y = r_x$, the expressions are:

$$a^-a^-c^0: \qquad r_x^2 = -\frac{\kappa^-}{2(2\alpha^- + \gamma^-)} \qquad E = E_0 - \frac{(\kappa^-)^2}{4\alpha^- + 2\gamma^-}$$

for $\mathbf{R}\,||$ in the [111] direction, taking $r_z = r_y = r_x$ the expressions are:

$$a^-a^-a^-: \qquad r_x^2 = -\frac{\kappa^-}{2(3\alpha^- + \gamma^-)} \qquad E = E_0 - \frac{(\kappa^-)^2}{4\alpha^- + \frac{4}{3}\gamma^-}$$

We also computed the Hessian for each of the phases discussed, and obtained that within our model, assuming the $\mathbf{R}$ a instability of the cubic phase (i.e., $\kappa^- < 0$ and $\alpha^- > 0$, with $|\alpha^-| > |\gamma^-|$), there can be only one type of minimum of the energy. More precisely, if $\gamma^- < 0$, we have a tetragonal ($a^-b^0b^0$) minimum; while the rhombohedral phase is stabilized for $\gamma^- > 0$. The orthorhombic phase on the other hand, is always a saddle point of the energy.
the only possible minimum is the rhombohedral $a^-a^-a^-$ phase, (see table 6.2).

According to this results, the relative energy between the different axes of the octahedra rotations will depend on the sign of γ^-. From these results, we may see that for a system with the tilting patterns composed only by anti-phase rotations, if the lower energy is that one along the [111] direction, then the coefficient γ^- must be positive.

$$\overbrace{-\frac{(\kappa^-)^2}{4\alpha^- + 4\gamma^-}}^{[100]} \quad > \quad \overbrace{-\frac{(\kappa^-)^2}{4\alpha^- + 2\gamma^-}}^{[110]} \quad > \quad \overbrace{-\frac{(\kappa^-)^2}{4\alpha^- + \frac{4}{3}\gamma^-}}^{[111]} \tag{6.7}$$

We may also see that the condition $\gamma > -3\alpha$ must be satisfied, otherwise the energy has unphysical divergence to $-\infty$, and the order of the expansion would need to be increased.

The same result is obtained if only in-phase tilting are considered. However, the situation is different when considering a composed tilting pattern of in-phase and anti-phase rotations. We also computed the energy minima condition for the most relevant case, (i.e., that corresponding

Table 6.2: Eigenvalues and eigenvectors obtained for the 4-th order theory. Results for the high symmetry phases here considered are shown.

	Eigenvalues (eigenvectors)		
$a^-b^0b^0$	$-4\kappa^-$	$\frac{2\kappa^-\gamma^-}{\alpha^-+\gamma^-}$	$\frac{2\kappa^-\gamma^-}{\alpha^-+\gamma^-}$
	(1, 0, 0)	(0, 1, 0)	(0, 0, 1)
$a^-a^-c^0$	$-4\kappa^-$	$-\frac{4\kappa^-\gamma^-}{2\alpha^-+\gamma^-}$	$\frac{2\kappa^-\gamma^-}{2\alpha^-+\gamma^-}$
	(1, 1, 0)	(−1, 1, 0)	(0, 0, 1)
$a^-a^-a^-$	$-4\kappa^-$	$-\frac{4\kappa^-\gamma^-}{3\alpha^-+\gamma^-}$	$-\frac{4\kappa^-\gamma^-}{3\alpha^-+\gamma^-}$
	(1, 1, 1)	(−1, 0, 1)	(−1, 1, 0)

to the orthorhombic $a^-a^-c^+$ phase) taking $r_x = r_y = r$, $m_z = m$, and $r_z = m_x = m_y = 0$, we have:

$$E(r,m) = E_0 + \kappa^+ m^2 + \kappa^- 2r^2 + \alpha^+ m^4 + \alpha^- 4r^4 + \alpha^{\pm} 2m^2 r^2 + \gamma^+ m^4 + \gamma^- 2r^4 \tag{6.8}$$

$$= E_0 + \kappa^+ m^2 + \kappa^- 2r^2 + \alpha^+ m^4 + \alpha^- 4r^4 + \alpha^{\pm} 2m^2 r^2$$

where we have used $\alpha^- = (2\alpha^- + \gamma^-)$ and $\alpha^+ = (\alpha^+ + \gamma^+)$ for an easier interpretation. From the conditions of extremal:

$$\frac{\partial E(r,m)}{\partial r}\Big|_m = 0 \qquad \text{and} \qquad \frac{\partial E(r,m)}{\partial m}\Big|_r = 0 \tag{6.9}$$

We find the equilibrium values for r and m are given by:

$$r^2 = \frac{-\kappa^-}{2\alpha^- - \frac{(\alpha^{\pm})^2}{\tilde{\alpha^+}}} + \frac{\kappa^+\alpha^{\pm}}{4\alpha^+\alpha^- - 2(\alpha^{\pm})^2} \qquad \text{and} \quad m^2 = \frac{-\kappa^+}{2\alpha^+ - \frac{(\alpha^{\pm})^2}{\tilde{\alpha^-}}} + \frac{\kappa^-\alpha^{\pm}}{2\alpha^+\alpha^- - (\alpha^{\pm})^2}$$

and the energy:

$$E^{a^-a^-c^+} = E_0 - \frac{(\kappa^-)^2}{2\alpha^- - \frac{(\alpha^{\pm})^2}{\tilde{\alpha^+}}} - \frac{(\kappa^+)^2}{2(2\alpha^+ - \frac{(\alpha^{\pm})^2}{\tilde{\alpha^-}})} + \frac{\kappa^-\kappa^+\alpha^{\pm}}{2\alpha^+\alpha^- - (\alpha^{\pm})^2}$$

These results now include the coefficient $\alpha^{\pm}$ for the coupling between the in-phase and anti-phase tilting.

We have thus introduced the simplest theory that may allow us to capture the energetics of the O_6- octahedra tilting in perovskites. Now, let us try to apply it to a simple material .

6.2 Case study: $LaAlO_3$

We first wanted to try our model for describing the energetics of the tilting patterns in a simple system. For that purpose we chose $LaAlO_3$, a paraelectric system that only exhibits O_6 octahedra rotations in its ground state. $LaAlO_3$ has a rhombohedral symmetry in its ground state, with the space group $R\bar{3}c$ ($a^-a^-a^-$). This material is insulating and does not exhibit magnetism, and thus its treatment should be relatively simple.

Calculation details

The calculations conditions were obtained from a convergence test following the scheme presented in section (1.2.2). As the system is not magnetic, it does not present strongly localized electrons in the valence and thus, we do not need to use U-corrected functionals. For the simulations we used the generalized gradient approximation (GGA) to density functional theory: more precisely, the PBE and PBEsol schemes as implemented in the VASP package. We have employed the PAW method to represent the ionic cores, solving for the following electrons: Al s $3s$, and $3p$; La s $5s$, $5p$, $5d$, and $6s$; and O s $2s$ and $2p$. Wave functions were represented in a plane-wave basis truncated at 600 eV, and a $3 \times 3 \times 3$, Γ-centered k-point grid was used for integrations within the Brillouin zone (BZ) corresponding to the 40-atoms cell (analogous to the one shown in Fig. 1.1).

6.2.1 Results for the exploration of high-symmetry phases

We started by studying the high-symmetry structures discussed in section 6.1, i.e., the anti-phase tilt patterns denoted by $a^-b^0b^0$, $a^-a^-c^0$ and $a^-a^-a^-$ in Glazer s notation. To do this, we run structural relaxations that are constrained to maintain the targeted symmetry. The results are shown in table 6.3. We ran the relaxations with and without considering the strain response to the O_6-rotations, in order to quantify the importance of the cell deformations.

As we can see the choice of the GGA functional plays an important role in the relative stabilities of the phases investigated. This was unexpected, as we thought that for a rather simple compound as $LaAlO_3$ the qualitative results would not be very sensitive to the functional. We also considered the orthorhombic $a^-a^-c^+$ tilting pattern, but the relaxations started from this configurations always ended in the $a^-a^-c^0$ phase.

Some important conclusions can be extracted from the results in table 6.3 already.

Table 6.3: Energies for the different configurations in $LaAlO_3$, at fixed cell and after full relaxations. These results were obtained for PBE and PBEsol functionals are presented. The energies are reported as relative energies with respect to the cubic phase. Note that the $\theta_x = ArcSin(r_x)$

$\Delta E = E - E_{cub}$ in [meV/f.u.]
(Rotation angles, θ_x, θ_y, θ_z) in [^{o}]

$LaAlO_3$	PBEsol		PBE	
	Fully relaxed	Fixed Cell	Fully relaxed	Fixed Cell
$a^-b^0b^0$	−11.91	−10.72	−17.91	−16.09
	(5.8, 0.0, 0.0)	(5.8, 0.0, 0.0)	(6.4, 0.0, 0.0)	(5.7, 0.0, 0.0)
$a^-a^-c^0$	**−12.30**	−10.52	−19.08	−14.73
	(**4.2**, **4.2**, **0.0**)	(4.2, 4.2, 0.0)	(4.7, 4.7, 0.0)	(4.4, 4.4, 0.0)
$a^-a^-a^-$	−12.26	**−11, 01**	**−19.16**	**−17.33**
	(3.4, 3.4, 3.4)	(**3.4**, **3.4**, **3.4**)	(**3.9**, **3.9**, **3.9**)	(**3.6**, **3.6**, **3.6**)
$a^0a^0a^0$	0, 00	0.00	0.00	0.00
	(0.0, 0.0, 0.0)	(0.0, 0.0, 0.0)	(0.0, 0.0, 0.0)	(0.0, 0.0, 0.0)

Functional dependence of the results

The experimental ground state was only obtained correctly with the PBE functional. To our surprise, the results obtained with PBEsol are not in agreement with the experimental observations for $LaAlO_3$, and the $a^-a^-c^0$ tilting pattern is predicted as the ground state of the material. However, as can be appreciated from the table 6.3, the differences in energy are very small, i.e., of the order of hundredth of meV per formula unit between the $a^-a^-c^0$ orthorhombic and $a^-a^-a^-$ rhombohedral phases. These small energy differences, and the wrong description given by PBEsol, may be an indicator of the need to include zero-point corrections in the calculations of the relative stability of these phases.

Effect of strain and compatibility with our 4-th order theory

The only result compatible with a 4-th order theory is the PBE result with cell relaxations. The fully-relaxed PBEsol results predict an orthorhombic ground state, which as discussed above, cannot be captured by our 4-th order theory. From table 6.3, we can also observe that for fixed cell calculation the energy relation obtained is: $E_{[111]} < E_{[100]} < E_{[110]}$, while the result of the 4-th order theory would be: $E_{[111]} < E_{[110]} < E_{[100]}$ (see relations 6.7). Two conclusions can be drawn from these numbers: (1) the strain has an important role in the relative phase stability; (2) even in the simpler case of a frozen strain relaxation, our 4-th order theory is not able to capture the first principle results.

Obtained coefficients for the 4-th order theory

While we have seen its validity is questionable, let us focus on the PBE fully relaxed results and see how well our 4-th order theory can describe them. From the results obtained for the high symmetry directions, we may fit the parameters regarding the anti-phase tilting (i.e., κ^-, α^-, and γ^-, see table 6.4).

Table 6.4: Different sets of parameters obtained for the 4-th order theory: Fit 1,was obtained enforcing the conditions for the tilting amplitudes for the minima; Fit 2, correspond to the conditions for the energies for the minima; Fit 3, is the fit to energies and tilting amplitudes of the minima

	Theory coefficients			$\Delta E = E - E_{cub}$ in [meV/f.u.] (Rotation angles, θ_x, θ_y, θ_z) in [^{o}]			
	κ^- [eV/Å^2]	α^- [eV/Å^4]	γ^- [eV/Å^4]		[100]	[110]	[111]
Fit 1	-23	747	247	Fit 1	-16.7	-19.1	-20.0
					$(6.1, 0, 0)$	$(4.7, 4.7, 0)$	$(3.9, 3.9, 3.9)$
Fit 2	-29	1351	172	Fit 2	-17.9	-18.9	-19.3
					$(5.6, 0, 0)$	$(4.1, 4.1, 0)$	$(3.4, 3.4, 3.4)$
Fit 3	-28	1242	126	Fit 3	-18.6	-19.5	-19.8
					$(5.8, 0, 0)$	$(4.2, 4.2, 0)$	$(3.5, 3.5, 3.5)$

From table 6.4, we may appreciate the energy hierarchy among the phases is well reproduced; however, the differences in energy between the orthorhombic and the rhombohedral phases are overestimated with any of the parameters obtained from the different fits. For example, fitting only to the structure, we found good agreement with the amplitude for the minima, but the energy difference between the tetragonal and rhombohedral phases are overestimated by a factor of ~ 3. The predicted curves are shown in Fig. 6.2 along with the calculated points for the different phases.

Checking for the presence of higher order terms in the energy landscape

So far, the energy hierarchy obtained with the PBE fully relaxed calculations are compatible with the 4-th order theory, but still there are some inconsistencies between the model and the calculated points. From our previous discussion in section 6.1, we know that we can only describe a single type of minimum (either rhombohedral or tetragonal) within our model. An important test with this respect is to check wether the computed phases are local minima or saddle points in the energy landscape. A simple way to determine this is to compute the interpolation path between the different phases and see how the energy changes.

From Fig. 6.2 we can appreciate that our calculations found the $a^-b^0b^0$, and $a^-a^-c^0$ phases are also local minima of the energy. This is apparent from the energy barriers that separate the different minima along the interpolation paths.

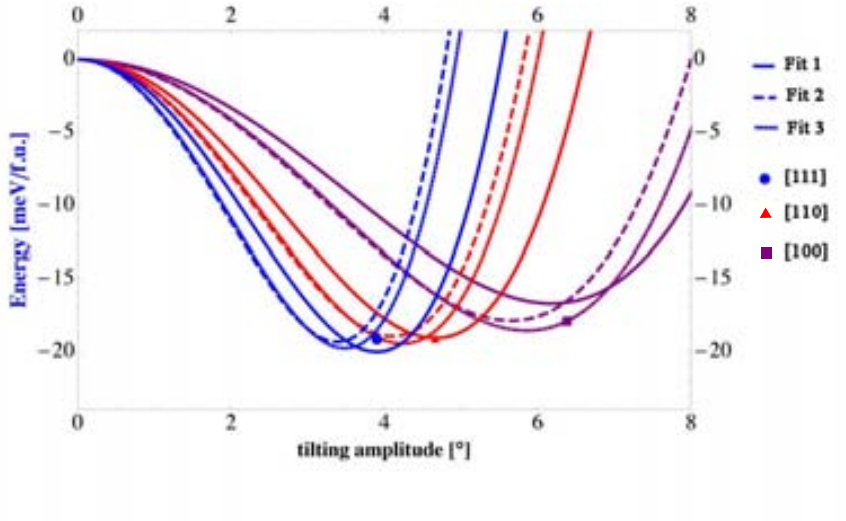

Figure 6.1: Energy dependence with respect to tilting angle for the different sets of parameters obtained, Fit 1 is represented in solid lines, Fit 2 in dashed and Fit 3 with dotted lines; the colors stand for: blue [111], red [110] and purple [100].

Hence in order to capture the energetics of $LaAlO_3$, even if computed at the PBE level we clearly need to increase the order of the theory.

6.3 Conclusions and next steps

Here we have shown the first step in constructing a general theory to capture the energetics of the most common distortions present in perovskites. We tried to capture the relative stability of different high symmetry phases in $LaAlO_3$ with an energy expansion up to 4-th order in the **M** and **R** AFD distortions. The analytic solutions of the model were compared with the DFT results for the minima along the high-symmetry directions [100], [110], and [111].

The relative stability of the phases was found to be only captured by the PBE functional. However, the energy differences obtained from our GGA calculations are very small within PBE, and wrong for PBEsol. An issue that would require a further investigation, as one would expected to have an adequate description of a system that is rather simple (not magnetic, insulating and paraelectric).

From our PBE calculations we have fitted the 4-th order theory. The obtained coefficients shown in table 6.4, where we can see that for $LaAlO_3$, the anti-phase tilting are a instability of the cubic phase (with $\kappa^- < 0$). Note that in our calculations we do not considered any case composed by complex tilts, thus we were not able to fit ϑ as it accounts for the occurrence of such complex distortions. We computed the energies along the interpolation path between the high-symmetry phases, and found that in the case of $LaAlO_3$ the 4-th order theory is not sufficient to describe the existence of the orthorhombic minimum ($a^-a^-b^0$) and thus, we would need to go for higher order theories.

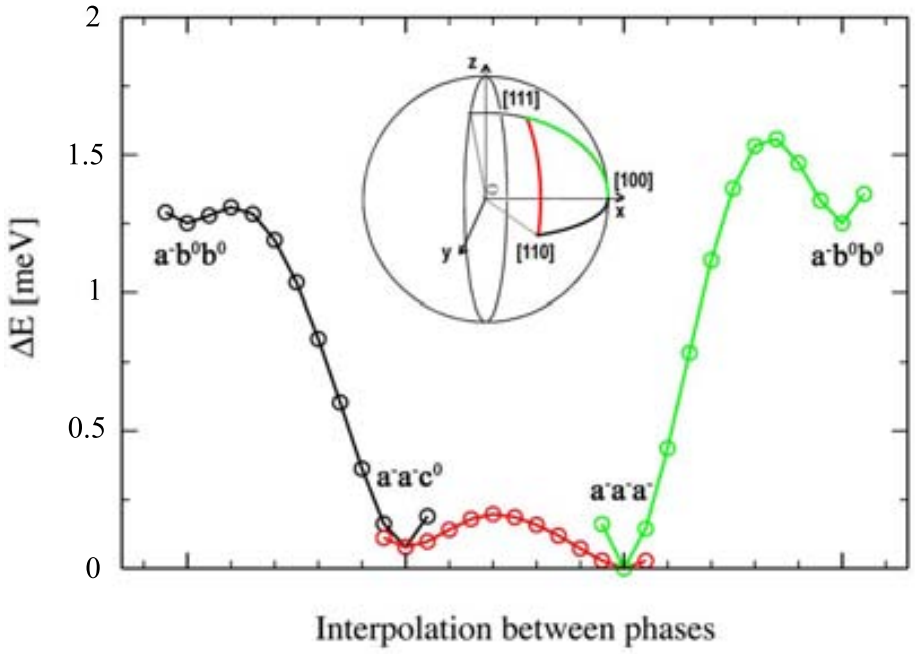

Figure 6.2: Computed energies along the interpolated paths linking the minima for the phases $a^-b^0b^0$, $a^-a^-b^0$ and $a^-a^-a^-$.

Thus, $LaAlO_3$ resulted to be a more complex material with respect to the structural phases it exhibit than expected. Therefore the next steps will be,

- With respect to the theoretical model, to extend the theory to higher order to describe the minima $LaAlO_3$ present.
- Regarding the DFT calculations, the question is whether the PBE functional is giving correctly the magnitude of the energy differences? It would be useful to have results for the relative energies of the phases discussed including zero-point corrections in the calculations.

The results presented in this last chapter are part of an ongoing project, that should finish with a general model to describe the interplay between the most common structural distortions in perovskite oxides, and the strain.

Conclusions

In the present work we have studied the properties of one of the most relevant magnetoelectric multiferroic materials, $BiFeO_3$. We have discussed the structural richness of this compound and the possible reason behind. The implications of our findings and the relation with recent experimental results were discussed in chapter 3. In this chapter we have presented the results of our first principles search for potentially stable phases of the multiferroic $BiFeO_3$. We performed a systematic study of most relevant distortions that are common to perovskite oxides (more specifically, ferroelectric, antiferroelectric, and anti-ferrodistortive). We obtained plenty of distinct low-energy phases of the compound and restricted our discussion to the most stable ones. We found that some of the minima presented here display complex structural distortions which lower the symmetry to M_A and M_C monoclinic space groups preserving a relatively small unit cell. This was a very peculiar finding because, as far as we know the monoclinic structures reported in perovskite oxides are usually associated to solid solutions [e.g. $PbZr_{1-x}Ti_xO_3$ (M_A type) [64] and $PbZn_{1/3}Nb_{2/3}O_3 - PbTiO_3$]; occur in thin films under epitaxial strain, or present relatively large unit cells.

From these results, a number of important implications for current research on BFO were discussed:

- First of all, we have found that BFO can form plenty of stable and metastable structural phases. This is consistent with recent experimental observations that show, a wide range of possible structural transitions at low temperatures, [73] surface-specific atomic structures [60] and strain-induced new phases. [40, 94] Also, our results can be useful for the experimental works exploring the possibility of obtaining large functional effects (piezoelectric, magnetoelectric) in BFO s films grown on strongly compressive substrates. We have shown that there are plenty of phases with large polarizations and c/a aspect ratios that can be realized in such conditions; the transitions (e.g., driven by temperature or electric fields) between such phases could give raise to useful effects.

- Our results also have implications for theoretical studies of BFO. We carried out a careful comparison of the various DFT schemes most commonly employed to study BFO and related compounds, and discussed the existing difficulties in quantifying the relative phase stability. Further, we considered the implications of our findings as regards the effective modeling of structural phase transitions in BFO. Our analysis shows that BFO is rather unusual, and requires very high-order Landau potentials to capture the diversity of structural phases that it presents. A result that is revealing the unexpected complexity of this material in comparison with the theories devised for materials such as $BaTiO_3$ or $PbZr_{1-x}Ti_xO_3$.

- Furthermore, we have shown quantitative evidence of the dominant role of Bi in BFO s structural instabilities. We have computed the ELF and observed how in some of the phases, the lone pair mechanism usually assumed to accompany the Bi O bonding, is absent. Instead, for the FE phases displaying strong Bi off centering, such a mechanism is present along with a large polarization. Thus, Bi s ability to form diverse and competitive in energy coordination complexes with oxygen, appears as one the reasons for the richness of structural phases presenting this material.

With this we have quantified, and analyzed in some detail the structural richness of $BiFeO_3$, the most relevant representative of the family of Bi-based transition-metal perovskite oxides. We have thus revealed a variety of unusual effects with important implications for current experimental and theoretical works on this material.

In chapter 4 we have used first-principles methods to study the $Bi_{1-x}La_xFeO_3$ (BLFO) solid solution formed by the multiferroic $BiFeO_3$ (BFO) and the paraelectric antiferromagnet $LaFeO_3$ (LFO). Investigating BLFO s phase transitions as a function of the La content x, we find that at $x \sim 0.3$ BLFO transforms discontinuously from BFOs rhombohedral ferroelectric phase into an orthorhombic structure. The nature of such an orthorhombic phase could not be fully determined from the simulations, as we obtained two different states namely, ferroelectric $Pna2_1$ and paraelectric $Pnma$ that are essentially as stable in the $0.3 \lesssim x \lesssim 0.65$ composition range. We also found that the paraelectric $Pnma$ phase prevails for $x \gtrsim 0.65$. The phase coexistence at intermediate x values suggests some appealing possibilities; for example, our results indicate that an electric field might be used to induce paraelectric-to-ferroelectric phase transformations in this compound. We have also discussed the connection between our results and published crystallographic studies of BLFO solid solutions. Our simulations do not support any of the many different phases that have been experimentally proposed to occur at intermediate compositions. We have suggested some explanations for the experimental difficulties that hamper BLFO s structural characterization.

Additionally, we have shown that the chemical substitution of Bi/La atoms in the pure compounds leads to significantly improved response properties. (Our calculations were restricted to the dielectric susceptibility, and we argue that the obtained enhancement should be observed in the magnetoelectric response as well.) We have analyzed in detail the diverse origins of the increased responses,

- In the case of Bi-doped LFO, the enhancement is associated with an incipient ferroelectric instability involving Bi O distortions.

- In contrast, in La-doped BFO the improvement relies on the strong structural relaxation and local symmetry breaking caused by the La atoms, which result in the appearance of many new polar modes that react to an applied electric field.

We have shown that both effects can be captured by a phenomenological theory in which the composition x is explicitly treated in a Landau-like potential.

In conclusion, our first-principles results for the BLFO multiferroic solid solution, suggest that these compounds present many appealing features, ranging from improved response properties to the possibility of inducing structural phase transitions by application of electric fields.

Further, we find that several BLFO phases are quasi-degenerate in energy in a wide composition range; thus, our calculations suggest that BLFO undergoes a very unusual morphotropic transformation that deserves a detailed experimental investigation. Finally, some of our results are strongly reminiscent of phenomena that has been experimentally found in similar solid solutions, as for example the $Bi_{1-x}R_xFeO_3$ compounds where R is a rare-earth lanthanide. Such similarities suggest that, BLFO may be a convenient model system, representative of this larger family of materials.

The high pressure effects on the spin configurations in the $3d$ orbitals of Fe^{3+} for $BiFeO_3$, were discussed in chapter 5. Our results support and explain the spin-crossover that is responsible for the change in the magnetic and conduction properties of $BiFeO_3$ at high pressures. More precisely, we found that under hydrostatic pressure the system:

- suffers a change in the coordination of the Bi atoms, which tend to form BiO_3 planar groups
- undergoes a HS-LS crossover transition for Fe^{3+} at pressures around 40 GPa
- the magnetic interactions are relatively weak in the LS phase, which should result in a relatively low magnetic ordering temperature
- the electronic structure of the LS phase strongly depends on the magnetic order, which suggests that, at room-temperature the paramagnetic LS phase will be metallic.

These are drastic transformations, which involve relatively large energy scales. Thus, these predictions seem reliable, in spite of the approximations made for our theoretical study. Our predictions for the HS-LS transition are thus consistent with the manifold transformation observed experimentally by Gavriliuk et al., [34] and provides an explanation for it.

Let us conclude by saying that our investigations were by no means exhaustive and many issues remain open. For example, our results strongly suggest that BFO will not present a cubic phase $Pm\bar{3}m$ at high pressures; however, we cannot deduce from our calculations the space group of the high-pressure phases. There are many possibilities involving unit cells larger than the 10-atom one used in our simulations, which were considered in this work. Similarly, the possibility of complex magnetic orders occurring at high pressures has not been explored. Finally, for more accurate quantitative calculations of the transition pressures, and the properties of the high-pressure phases, it would be required the use of sophisticated first-principles techniques that can improve over our LDA+U results.

In chapter 6 we have presented a preliminary study on the energy maps for rotations of the oxygen octahedra in perovskite oxides. Here we have shown the first step in constructing a general theory to capture the energetics of the most common distortions present in perovskites. We tried to capture the relative stability of different high symmetry phases in $LaAlO_3$ with an energy expansion up to 4-th order in the **M** and **R** AFD distortions. The analytic solutions of the model were compared with the DFT results for the minima along the high-symmetry directions [100], [110], and [111].

The relative stability of the phases was found to be only captured by the PBE functional. However, the energy differences obtained from our GGA calculations are very small within

PBE, and wrong for PBEsol. An issue that would require a further investigation, as one would expected to have an adequate description of a system that is rather simple (not magnetic, insulating and paraelectric).

From our PBE calculations we have fitted the 4-th order theory. The obtained coefficients shown in table 6.4, where we can see that for $LaAlO_3$, the anti-phase tilting are a instability of the cubic phase (with $\kappa^- < 0$). Note that in our calculations we do not considered any case composed by complex tilts, thus we were not able to fit ϑ as it accounts for the occurrence of such complex distortions. We computed the energies along the interpolation path between the high-symmetry phases, and found that in the case of $LaAlO_3$ the 4-th order theory is not sufficient to describe the existence of the orthorhombic minimum ($a^-a^-b^0$) and thus, we would need to go for higher order theories.

Thus, $LaAlO_3$ resulted to be a more complex material with respect to the structural phases it exhibit than expected. Therefore the next steps will be,

- With respect to the theoretical model, to extend the theory to higher order to describe the minima $LaAlO_3$ present.
- Regarding the DFT calculations, the question is whether the PBE functional is giving correctly the magnitude of the energy differences? It would be useful to have results for the relative energies of the phases discussed including zero-point corrections in the calculations.

The results presented in this last chapter are part of an ongoing project, that should finish with a general model to describe the interplay between the most common structural distortions in perovskite oxides, and the strain.

Bibliography

[1] Vladimir I. Anisimov, Jan Zaanen, and Ole K. Andersen. Band theory and mott insulators: Hubbard U instead of stoner I. *Phys. Rev. B*, 44:943 954, Jul 1991.

[2] G.B. Arfken and H.J. Weber. *Mathematical methods for physicists*. Elsevier, 2005.

[3] Donna C. Arnold, Kevin S. Knight, Gustau Catalan, Simon A. T. Redfern, James F. Scott, Philip Lightfoot, and Finlay D. Morrison. The ?-to-? transition in bifeo3: A powder neutron diffraction study. *Advanced Functional Materials*, 20(13):2116 2123, 2010.

[4] Pio Baettig, Claude Ederer, and Nicola A. Spaldin. First principles study of the multiferroics $BiFeo_3$, bi_2FeCro_6, and $BiCro_3$: Structure, polarization, and magnetic ordering temperature. *Phys. Rev. B*, 72:214105, Dec 2005.

[5] A. Baldereschi. Mean-value point in the brillouin zone. *Phys. Rev. B*, 7:5212 5215, Jun 1973.

[6] H. Bea, M. Bibes, S. Petit, J. Kreisel, and A. Barthelemy. Structural distortion and magnetism of bifeo3 epitaxial thin films: A raman spectroscopy and neutron diffraction study. *Philosophical Magazine Letters*, 87(3-4):165 174, 2007.

[7] H. Béa, B. Dupé, S. Fusil, R. Mattana, E. Jacquet, B. Warot-Fonrose, F. Wilhelm, A. Rogalev, S. Petit, V. Cros, A. Anane, F. Petroff, K. Bouzehouane, G. Geneste, B. Dkhil, S. Lisenkov, I. Ponomareva, L. Bellaiche, M. Bibes, and A. Barthélémy. Evidence for room-temperature multiferroicity in a compound with a giant axial ratio. *Phys. Rev. Lett.*, 102:217603, May 2009.

[8] E.F. Bertaut and M. Mercier. Structure magnetique de mnyo3. *Physics Letters*, 5(1):27 29, 1963.

[9] Satadeep Bhattacharjee, Eric Bousquet, and Philippe Ghosez. Engineering multiferroism in $camno_3$. *Phys. Rev. Lett.*, 102:117602, Mar 2009.

[10] D. I. Bilc, R. Orlando, R. Shaltaf, G.-M. Rignanese, Jorge Íniguez, and Ph. Ghosez. Hybrid exchange-correlation functional for accurate prediction of the electronic and structural properties of ferroelectric oxides. *Phys. Rev. B*, 77:165107, Apr 2008.

[11] P. E. Blochl. Projector augmented-wave method. *Phys. Rev. B*, 50:17953 17979, Dec 1994.

[12] M. Born and Oppenheimer. Zur quantentheorie der molekeln. *Annalen der Physik*, 389:457484, 1927.

[13] W. F. Brown, R. M. Hornreich, and S. Shtrikman. Upper bound on the magnetoelectric susceptibility. *Phys. Rev.*, 168:574 577, Apr 1968.

[14] Branton J. Campbell, Harold T. Stokes, David E. Tanner, and Dorian M. Hatch. *ISODISPLACE*: a web-based tool for exploring structural distortions. *Journal of Applied Crystallography*, 39(4):607 614, Aug 2006.

[15] Gustau Catalan and James F. Scott. Physics and applications of bismuth ferrite. *Advanced Materials*, 21(24):2463 2485, 2009.

[16] D. J. Chadi and Marvin L. Cohen. Special points in the brillouin zone. *Phys. Rev. B*, 8:5747 5753, Dec 1973.

[17] Peuzin J C Buisson G Coeure P, Guinet F and Bertaut E F. *Proc. International Meeting on Ferroelectricity (Prague, 1966)*, 1966.

[18] C. J. M. Daumont, S. Farokhipoor, A. Ferri, J. C. Wojdel, Jorge Íniguez, B. J. Kooi, and B. Noheda. Tuning the atomic and domain structure of epitaxial films of multiferroic $bifeo_3$. *Phys. Rev. B*, 81:144115, Apr 2010.

[19] M. De La Pierre, R. Orlando, L. Maschio, K. Doll, P. Ugliengo, and R. Dovesi. Performance of six functionals (lda, pbe, pbesol, b3lyp, pbe0, and wc1lyp) in the simulation of vibrational and dielectric properties of crystalline compounds. the case of forsterite mg2sio4. *Journal of Computational Chemistry*, 32(9):1775 1784, 2011.

[20] A.F. Devonshire. Theory of ferroelectrics. *Advances in Physics*, 3(10):85 130, 1954.

[21] Oswaldo Diéguez and Jorge Íniguez. First-principles investigation of morphotropic transitions and phase-change functional responses in $bifeo_3$-$bicoo_3$ multiferroic solid solutions. *Phys. Rev. Lett.*, 107:057601, Jul 2011.

[22] Oswaldo Diéguez, Silvia Tinte, A. Antons, Claudia Bungaro, J. B. Neaton, Karin M. Rabe, and David Vanderbilt. *Ab initio* study of the phase diagram of epitaxial $batio_3$. *Phys. Rev. B*, 69:212101, Jun 2004.

[23] S. L. Dudarev, G. A. Botton, S. Y. Savrasov, C. J. Humphreys, and A. P. Sutton. Electron-energy-loss spectra and the structural stability of nickel oxide: an lsda+u study. *Phys. Rev. B*, 57:1505 1509, Jan 1998.

[24] W. Eerenstein, N. D. Mathur, and J. F. Scott. Multiferroic and magnetoelectric materials. *Nature*, 442(7104):759 765, 08 2006.

[25] M. Eibschutz and H.J. Guggenheim. Antiferromagnetic-piezoelectric crystals: Bame4 (m = mn, fe, co and ni). *Solid State Communications*, 6(10):737 739, 1968.

[26] B. Wruck E.K.H. Salje and H. Thomas. *Z. Phys. B*, 82:399, 1991.

[27] Enrico Fermi. Un metodo statistico per la determinazione di alcune priopriet dell atomo. *Rend. Accad. Naz. Lincei*, 6:602607, 1927.

[28] Manfred Fiebig. Revival of the magnetoelectric effect. *Journal of Physics D: Applied Physics*, 38(8):R123, 2005.

[29] Alessio Filippetti and Nicola A. Hill. Coexistence of magnetism and ferroelectricity in perovskites. *Phys. Rev. B*, 65:195120, May 2002.

[30] Z.V. Gabbasova, M.D. Kuz min, A.K. Zvezdin, I.S. Dubenko, V.A. Murashov, D.N. Rakov, and I.B. Krynetsky. Bi1xrxfeo3 (r=rare earth): a family of novel magnetoelectrics. *Physics Letters A*, 158(9):491 498, 1991.

[31] A. Gavriliuk, I. Lyubutin, and V. Struzhkin. Electronic transition and the metallization effect in the bifeo$_3$ crystal at high pressures. *JETP Letters*, 86:532 536, 2007. 10.1134/S0021364007200088.

[32] A. Gavriliuk, V. Struzhkin, I. Lyubutin, M. Hu, and H. Mao. Phase transition with suppression of magnetism in bifeo$_3$ at high pressure. *JETP Letters*, 82:224 227, 2005. 10.1134/1.2121819.

[33] A. Gavriliuk, V. Struzhkin, I. Lyubutin, and I. Troyan. Equation of state and structural transition at high hydrostatic pressures in the bifeo$_3$ crystal. *JETP Letters*, 86:197 201, 2007. 10.1134/S0021364007150106.

[34] Alexander G. Gavriliuk, Viktor V. Struzhkin, Igor S. Lyubutin, Sergey G. Ovchinnikov, Michael Y. Hu, and Paul Chow. Another mechanism for the insulator-metal transition observed in mott insulators. *Phys. Rev. B*, 77:155112, Apr 2008.

[35] A. M. George, Jorge Iniguez, and L. Bellaiche. Anomalous properties in ferroelectrics induced by atomic ordering. *Nature*, 413(6851):54 57, 09 2001.

[36] A. M. Glazer. The classification of tilted octahedra in perovskites. *Acta Crystallographica Section B*, 28(11):3384 3392, Nov 1972.

[37] J.B. Goodenough. Theory of the role of covalence in the perovskite-type manganites [la,m(ii)]mno3. *Physical Review*, 100(2):564 573, 1955. cited By (since 1996) 1535.

[38] Mael Guennou, Pierre Bouvier, Grace S. Chen, Brahim Dkhil, Raphael Haumont, Gaston Garbarino, and Jens Kreisel. Multiple high-pressure phase transitions in bifeo$_3$. *Phys. Rev. B*, 84:174107, Nov 2011.

[39] Alison J. Hatt, Nicola A. Spaldin, and Claude Ederer. Strain-induced isosymmetric phase transition in bifeo$_3$. *Phys. Rev. B*, 81:054109, Feb 2010.

[40] R. Haumont, P. Bouvier, A. Pashkin, K. Rabia, S. Frank, B. Dkhil, W. A. Crichton, C. A. Kuntscher, and J. Kreisel. Effect of high pressure on multiferroic bifeo$_3$. *Phys. Rev. B*, 79:184110, May 2009.

[41] M. J. Haun, E. Furman, S. J. Jang, and L. E. Cross. Thermodynamic theory of the lead zirconate-titanate solid solution system, part i: Phenomenology. *Ferroelectrics*, 99(1):13 25, 1989.

[42] M. J. Haun, E. Furman, H. A. McKinstry, and L. E. Cross. Thermodynamic theory of the lead zirconate-titanate solid solution system, part ii: Tricritical behavior. *Ferroelectrics*, 99(1):27 44, 1989.

[43] Nicola A. Hill. Why are there so few magnetic ferroelectrics? *The Journal of Physical Chemistry B*, 104(29):6694 6709, 2000.

[44] P. Hohenberg and W. Kohn. Inhomogeneous electron gas. *Phys. Rev.*, 136:B864 B871, Nov 1964.

[45] C. J. Howard and H. T. Stokes. Group-Theoretical Analysis of Octahedral Tilting in Perovskites. *Acta Crystallographica Section B*, 54(6):782 789, Dec 1998.

[46] Jorge Íniguez. First-principles approach to lattice-mediated magnetoelectric effects. *Phys. Rev. Lett.*, 101:117201, Sep 2008.

[47] Jorge Íniguez and L. Bellaiche. Ab initio design of perovskite alloys with predetermined properties: The case of $Pb(sc_{0.5}nb_{0.5})O_3$. *Phys. Rev. Lett.*, 87:095503, Aug 2001.

[48] Jorge Íniguez, S. Ivantchev, J. M. Perez-Mato, and Alberto García. Devonshire-landau free energy of $batio_3$ from first principles. *Phys. Rev. B*, 63:144103, Mar 2001.

[49] Naoshi Ikeda, Hiroyuki Ohsumi, Kenji Ohwada, Kenji Ishii, Toshiya Inami, Kazuhisa Kakurai, Youichi Murakami, Kenji Yoshii, Shigeo Mori, Yoichi Horibe, and Hijiri Kito. Ferroelectricity from iron valence ordering in the charge-frustrated system lufe2o4. *Nature*, 436(7054):1136 1138, 08 2005.

[50] R. O. Jones and O. Gunnarsson. The density functional formalism, its applications and prospects. *Rev. Mod. Phys.*, 61:689 746, Jul 1989.

[51] Junjiro and Kanamori. Superexchange interaction and symmetry properties of electron orbitals. *Journal of Physics and Chemistry of Solids*, 10(2-3):87 98, 1959.

[52] Daisuke Kan, Lucia Plov, Varatharajan Anbusathaiah, Ching Jung Cheng, Shigehiro Fujino, Valanoor Nagarajan, Karin M. Rabe, and Ichiro Takeuchi. Universal behavior and electric-field-induced structural transition in rare-earth-substituted bifeo3. *Advanced Functional Materials*, 20(7):1108 1115, 2010.

[53] D.V. Karpinsky, I.O. Troyanchuk, J.V. Vidal, N.A. Sobolev, and A.L. Kholkin. Enhanced ferroelectric, magnetic and magnetoelectric properties of bi1xcaxfe1xtixo3 solid solutions. *Solid State Communications*, 151(7):536 540, 2011.

[54] R. D. King-Smith and David Vanderbilt. First-principles investigation of ferroelectricity in perovskite compounds. *Phys. Rev. B*, 49:5828 5844, Mar 1994.

[55] W. Kohn and L. J. Sham. Self-consistent equations including exchange and correlation effects. *Phys. Rev.*, 140:A1133 A1138, Nov 1965.

[56] Igor A. Kornev, S. Lisenkov, R. Haumont, B. Dkhil, and L. Bellaiche. Finite-temperature properties of multiferroic $bifeo_3$. *Phys. Rev. Lett.*, 99:227602, Nov 2007.

[57] G. Kresse and J. Furthmuller. Efficient iterative schemes for *ab initio* total-energy calculations using a plane-wave basis set. *Phys. Rev. B*, 54:11169 11186, Oct 1996.

[58] G. Kresse and D. Joubert. From ultrasoft pseudopotentials to the projector augmented-wave method. *Phys. Rev. B*, 59:1758 1775, Jan 1999.

[59] Mel Levy, John P. Perdew, and Viraht Sahni. Exact differential equation for the density and ionization energy of a many-particle system. *Phys. Rev. A*, 30:2745 2748, Nov 1984.

[60] Xavi Martí, Pilar Ferrer, Julia Herrero-Albillos, Jackeline Narvaez, Vaclav Holy, Nick Barrett, Marin Alexe, and Gustau Catalan. Skin layer of bifeo$_3$ single crystals. *Phys. Rev. Lett.*, 106:236101, Jun 2011.

[61] Hendrik J. Monkhorst and James D. Pack. Special points for brillouin-zone integrations. *Phys. Rev. B*, 13:5188 5192, Jun 1976.

[62] Maxim Mostovoy, Andrea Scaramucci, Nicola A. Spaldin, and Kris T. Delaney. Temperature-dependent magnetoelectric effect from first principles. *Phys. Rev. Lett.*, 105:087202, Aug 2010.

[63] J. B. Neaton, C. Ederer, U. V. Waghmare, N. A. Spaldin, and K. M. Rabe. First-principles study of spontaneous polarization in multiferroic BiFeo$_3$. *Phys. Rev. B*, 71:014113, Jan 2005.

[64] B. Noheda, D. E. Cox, G. Shirane, J. A. Gonzalo, L. E. Cross, and S-E. Park. A monoclinic ferroelectric phase in the pb(zr[sub 1 - x]ti[sub x])o[sub 3] solid solution. *Applied Physics Letters*, 74(14):2059 2061, 1999.

[65] R. Palai, R. S. Katiyar, H. Schmid, P. Tissot, S. J. Clark, J. Robertson, S. A. T. Redfern, G. Catalan, and J. F. Scott. β phase and γ-β metal-insulator transition in multiferroic BiFeo$_3$. *Phys. Rev. B*, 77:014110, Jan 2008.

[66] J. P. Perdew and Alex Zunger. Self-interaction correction to density-functional approximations for many-electron systems. *Phys. Rev. B*, 23:5048 5079, May 1981.

[67] John P. Perdew, Kieron Burke, and Matthias Ernzerhof. Generalized gradient approximation made simple. *Phys. Rev. Lett.*, 77:3865 3868, Oct 1996.

[68] John P. Perdew, Kieron Burke, and Matthias Ernzerhof. Generalized gradient approximation made simple [phys. rev. lett. 77, 3865 (1996)]. *Phys. Rev. Lett.*, 78:1396 1396, Feb 1997.

[69] John P. Perdew, Adrienn Ruzsinszky, Gábor I. Csonka, Oleg A. Vydrov, Gustavo E. Scuseria, Lucian A. Constantin, Xiaolan Zhou, and Kieron Burke. Restoring the density-gradient expansion for exchange in solids and surfaces. *Phys. Rev. Lett.*, 100:136406, Apr 2008.

[70] John P. Perdew and Yue Wang. Accurate and simple analytic representation of the electron-gas correlation energy. *Phys. Rev. B*, 45:13244 13249, Jun 1992.

[71] S. Prosandeev, Igor A. Kornev, and L. Bellaiche. Magnetoelectricity in bifeo$_3$ films: First-principles-based computations and phenomenology. *Phys. Rev. B*, 83:020102, Jan 2011.

[72] William Ratcliff, Daisuke Kan, Wangchun Chen, Shannon Watson, Songxue Chi, Ross Erwin, Garry J. McIntyre, Sylvia C. Capelli, and Ichiro Takeuchi. Neutron diffraction investigations of magnetism in bifeo3 epitaxial films. *Advanced Functional Materials*, 21(9):1567 1574, 2011.

[73] S A T Redfern, Can Wang, J W Hong, G Catalan, and J F Scott. Elastic and electrical anomalies at low-temperature phase transitions in bifeo$_3$. *Journal of Physics: Condensed Matter*, 20(45):452205, 2008.

[74] James M. Rondinelli, Massimiliano Stengel, and Nicola A. Spaldin. Carrier-mediated magnetoelectricity in complex oxide heterostructures. *Nat Nano*, 3(1):46 50, 01 2008.

[75] Dmitriy A. Rusakov, Artem M. Abakumov, Kazunari Yamaura, Alexei A. Belik, Gustaaf Van Tendeloo, and Eiji Takayama-Muromachi. Structural evolution of the bifeo3?lafeo3 system. *Chemistry of Materials*, 23(2):285 292, 2011.

[76] Na Sai and David Vanderbilt. First-principles study of ferroelectric and antiferrodistortive instabilities in tetragonal srtio$_3$. *Phys. Rev. B*, 62:13942 13950, Dec 2000.

[77] H. Schmid. On a magnetoelectric classification of materials. *Int. J. Magn*, 4:337 361, 1973.

[78] Hans Schmid. Introduction to the proceedings of the 2nd international conference on magnetoelectric interaction phenomena in crystals, meipic-2. *Ferroelectrics*, 161(1):1 28, 1994.

[79] Hans Schmid. Multi-ferroic magnetoelectrics. *Ferroelectrics*, 162(1):317 338, 1994.

[80] J. F. Scott. Spectroscopy of incommensurate ferroelectrics. *Ferroelectrics*, 24(1):127 134, 1980.

[81] J. Seidel, L. W. Martin, Q. He, Q. Zhan, Y. H. Chu, A. Rother, M. E. Hawkridge, P. Maksymovych, P. Yu, M. Gajek, N. Balke, S. V. Kalinin, S. Gemming, F. Wang, G. Catalan, J. F. Scott, N. A. Spaldin, J. Orenstein, and R. Ramesh. Conduction at domain walls in oxide multiferroics. *Nat Mater*, 8(3):229 234, 03 2009.

[82] Hisashi Sugie, Nobuyuki Iwata, and Kay Kohn. Magnetic ordering of rare earth ions and magnetic-electric interaction
of hexagonal rmno$_3$ (r=ho, er, yb or lu). *Journal of the Physical Society of Japan*, 71(6):1558 1564, 2002.

[83] L. H. Thomas. The calculation of atomic fields. *Mathematical Proceedings of the Cambridge Philosophical Society*, 23(05):542 548, 1927.

[84] I. O. Troyanchuk, M. V. Bushinsky, D. V. Karpinsky, O. S. Mantytskaya, V. V. Fedotova, and O. I. Prochnenko. Structural transformations and magnetic properties of bi1xlnx feo3 (ln = la, nd, eu) multiferroics. *physica status solidi (b)*, 246(8):1901 1907, 2009.

[85] I. O. Troyanchuk, D. V. Karpinsky, M. V. Bushinsky, V. A. Khomchenko, G. N. Kakazei, J. P. Araujo, M. Tovar, V. Sikolenko, V. Efimov, and A. L. Kholkin. Isothermal structural transitions, magnetization and large piezoelectric response in bi$_{1-x}$la$_x$feo$_3$ perovskites. *Phys. Rev. B*, 83:054109, Feb 2011.

[86] David Vanderbilt and Morrel H. Cohen. Monoclinic and triclinic phases in higher-order devonshire theory. *Phys. Rev. B*, 63:094108, Jan 2001.

[87] Y. N. Venevtsev, V. V. Gagulin, and I. D. Zhitomirsky. Material science aspects of seignette-magnetism problem. *Ferroelectrics*, 73(1):221 248, 1987.

[88] J. Wang, J. B. Neaton, H. Zheng, V. Nagarajan, S. B. Ogale, B. Liu, D. Viehland, V. Vaithyanathan, D. G. Schlom, U. V. Waghmare, N. A. Spaldin, K. M. Rabe, M. Wuttig, and R. Ramesh. Epitaxial bifeo3 multiferroic thin film heterostructures. *Science*, 299(5613):1719 1722, 2003.

[89] Jacek C. Wojdel and Jorge Íniguez. Magnetoelectric response of multiferroic bifeo$_3$ and related materials from first-principles calculations. *Phys. Rev. Lett.*, 103:267205, Dec 2009.

[90] Jacek C. Wojdel and Jorge Íniguez. *Ab Initio* indications for giant magnetoelectric effects driven by structural softness. *Phys. Rev. Lett.*, 105:037208, Jul 2010.

[91] Xifan Wu, David Vanderbilt, and D. R. Hamann. Systematic treatment of displacements, strains, and electric fields in density-functional perturbation theory. *Phys. Rev. B*, 72:035105, Jul 2005.

[92] Zhigang Wu and R. E. Cohen. More accurate generalized gradient approximation for solids. *Phys. Rev. B*, 73:235116, Jun 2006.

[93] A. Zalesskii, A. Frolov, T. Khimich, and A. Bush. Composition-induced transition of spin-modulated structure into a uniform antiferromagnetic state in a bi1-xlaxfeo3 system studied using fe nmr. *Physics of the Solid State*, 45:141 145, 2003. 10.1134/1.1537425.

[94] R. J. Zeches, M. D. Rossell, J. X. Zhang, A. J. Hatt, Q. He, C.-H. Yang, A. Kumar, C. H. Wang, A. Melville, C. Adamo, G. Sheng, Y.-H. Chu, J. F. Ihlefeld, R. Erni, C. Ederer, V. Gopalan, L. Q. Chen, D. G. Schlom, N. A. Spaldin, L. W. Martin, and R. Ramesh. A strain-driven morphotropic phase boundary in bifeo3. *Science*, 326(5955):977 980, 2009.

[95] W. Zhong, R. D. King-Smith, and David Vanderbilt. Giant lo-to splittings in perovskite ferroelectrics. *Phys. Rev. Lett.*, 72:3618 3621, May 1994.

[96] W. Zhong and David Vanderbilt. Competing structural instabilities in cubic perovskites. *Phys. Rev. Lett.*, 74:2587 2590, Mar 1995.

[97] A.K. Zvezdin, A.M. Kadomtseva, S.S. Krotov, A.P. Pyatakov, Yu.F. Popov, and G.P. Vorobev. Magnetoelectric interaction and magnetic field control of electric polarization in multiferroics. *Journal of Magnetism and Magnetic Materials*, 300(1):224 228, 2006. ce:title The third Moscow International Symposium on Magnetism 2005 /ce:title xocs:full-name The third Moscow International Symposium on Magnetism 2005 /xocs:full-name .